ADA081542

AFML-TR-79-4151

RESPONSE OF INFRARED-TRANSPARENT MATERIALS TO RAINDROP IMPACTS

William F. Adler, John C. Botke, and Timothy W. James

Effects Technology, Inc.
5383 Hollister Ave.
Santa Barbara, Ca. 93111

October 1979

TECHNICAL REPORT AFML-TR-79-4151

Final Report for Period August 1978 — August 1979

DTIC
SELECTED
MAR 10 1980

A

AIR FORCE MATERIALS LABORATORY
AIR FORCE WRIGHT AERONAUTICAL LABORATORIES
AIR FORCE SYSTEMS COMMAND
WRIGHT-PATTERSON AIR FORCE BASE, OHIO 45433

DDC FILE COPY

80 3 6 014

NOTICE

When Government drawings, specifications, or other data are used for any purpose other than in connection with a definitely related Government procurement operation, the United States Government thereby incurs no responsibility nor any obligation whatsoever; and the fact that the Government may have formulated, furnished, or in any way supplied the said drawings, specifications, or other data, is not to be regarded by implication or otherwise as in any manner licensing the holder or any other person or corporation, or conveying any rights or permission to manufacture, use, or sell any patented invention that may in any way be related thereto.

This report has been reviewed by the Information Office (OI) and is releasable to the National Technical Information Service (NTIS). At NTIS, it will be available to the general public, including foreign nations.

This technical report has been reviewed and is approved for publication.
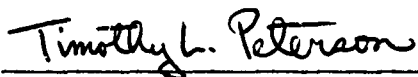
TIMOTHY L. PETERSON, Project Engineer

Coatings & Thermal Protection
    Materials Branch
Nonmetallic Materials Division

WILLIAM C. KESSLER, Acting Chief

Coatings & Thermal Protection
    Materials Branch
Nonmetallic Materials Division

FOR THE COMMANDER

J. M. KELBLE, Chief

Nonmetallic Materials Division

"If your address has changed, if you wish to be removed from our mailing list, or if the addressee is no longer employed by your organization, please notify AFML/MBE, W-P AFB, OH 45433 to help us maintain a current mailing list."

Copies of this report should not be returned unless return is required by security considerations, contractual obligations, or notice on a specific document.

14 ETI-CR 79-60

REPORT DOCUMENTATION PAGE		READ INSTRUCTIONS BEFORE COMPLETING FORM
1. REPORT NUMBER AFML-TR-79-4151	2. GOVT ACCESSION NO.	3. RECIPIENT'S CATALOG NUMBER
4. TITLE (and Subtitle) RESPONSE OF INFRARED-TRANSPARENT MATERIALS TO RAINDROP IMPACTS		5. TYPE OF REPORT & PERIOD COVERED Final Report August 1978 — August 1979
		6. PERFORMING ORG. REPORT NUMBER CR79-60
7. AUTHOR(s) William F. Adler John C. Botke Timothy W. James		8. CONTRACT OR GRANT NUMBER(s) F33615-78-C-5143
9. PERFORMING ORGANIZATION NAME AND ADDRESS Effects Technology, Inc. 5383 Hollister Avenue Santa Barbara, CA 93111		10. PROGRAM ELEMENT PROJECT, TASK AREA & WORK UNIT NUMBERS Project 2423, Task 242302 Work Unit 24230206
11. CONTROLLING OFFICE NAME AND ADDRESS Air Force Materials Laboratory Air Force Wright Aeronautical Laboratories Wright-Patterson AFB, Ohio		12. REPORT DATE October 1979
		13. NUMBER OF PAGES 165
14. MONITORING AGENCY NAME & ADDRESS(if different from Controlling Office) Air Force Materials Lab (AFML/MBE) Air Force Wright Aeronautical Laboratories Air Force Systems Command Wright-Patterson AFB, Ohio 45433		15. SECURITY CLASS (of this report) UNCLASSIFIED
		15a. DECLASSIFICATION DOWNGRADING SCHEDULE

16. DISTRIBUTION STATEMENT (of this Report)

APPROVED FOR PUBLIC RELEASE; DISTRIBUTION UNLIMITED.

17. DISTRIBUTION STATEMENT (of the abstract entered in Block 20, if different from Report)

18. SUPPLEMENTARY NOTES

19. KEY WORDS (Continue on reverse side if necessary and identify by block number)

Chemical vapor deposition	Stress waves	Fracture toughness
Zinc sulfide	Fracture	Hardness
Infrared transmitting material	Impact	Grain size
Water drop impingement	Shock waves	
Rain erosion		

20. ABSTRACT (Continue on reverse side if necessary and identify by block number)

This investigation concentrates on the damage produced in chemically vapor deposited (CVD) zinc sulfide (ZnS) by water drop impacts on the order of 1 mm in diameter impinging over a velocity range from 222 to 684 ms^{-1} (730 to 2240 fps). A combined experimental and analytical approach was pursued to determine the relationships between water drop impact damage and the material properties of CVD ZnS in order to evaluate and guide efforts to develop erosion resistant window materials for use at 8-12 μm wavelengths.

DD FORM 1473 1 JAN 73   EDITION OF 1 NOV 55 IS OBSOLETE

Microscopic observations of the damage produced in three formulations of CVD ZnS representing variations in grain size, grain shape, and inclusion content indicated the fracture trajectories and penetration depths were essentially insensitive to the range of microstructural features which were investigated. The quality of the surface finish was found to be the dominant contribution to the fracture response of CVD ZnS. Further modification of the bulk material properties does not appear warranted: the present production material is satisfactory. Considerably greater latitude for increased resistance to rain erosion can be gained from improved polishing procedures and subsequent maintenance of the initial surface finish.

Since the fracture response of CVD ZnS is controlled by surface polishing flaws, a continuum mechanics analysis was introduced to estimate the potential for fracture due to the transient stresses generated by the water drop collision. Various approximations are considered for illustration purposes. The limitations of previous analyses are described and the need for an analysis which is applicable within 10 μm from the surface of the target is demonstrated. These conditions motivated a mathematical analysis of the transient stress states due to an arbitrarily spatially and temporally varying localized pressure on the target's surface formulated in terms of Green's function and a Green's theorem relation derived from the divergence theorem. The Green's function analysis is then utilized to develop an analysis for surface flaw, stress wave interactions.

Hydraulic penetration of the water in a drop impacting over a pre-existing surface defect is also modeled mathematically, since this has been identified as an important factor in the internal fracture growth observed in CVD ZnS due to multiple water drop collisions. In addition, the effect of the internal fractures on transmission through the window is analyzed. The significance of the crack separation distance and crack orientation on the transmittance is evaluated.

FOREWORD

iii

TABLE OF CONTENTS

LIST OF ILLUSTRATIONS

LIST OF ILLUSTRATIONS (concluded)

LIST OF TABLES

SECTION I

INTRODUCTION

This investigation concentrates on the damage produced in chemically vapor deposited (CVD) zinc sulfide (ZnS) by water drop impacts on the order of 1 mm in diameter impinging over a velocity range from 222 to 684 ms^{-1} (730 to 2240 fps). A combined experimental and analytical study was pursued to determine the relationships between water drop impact damage and the material properties of CVD zinc sulfide in order to evaluate and guide efforts to develop erosion resistant window materials for use at 8-12 μm wavelengths. The general problem can be divided into three major categories and each of these categories involves a number of experimental and analytical tasks. The suggested categorization outlined below is essentially our overview of the general problem and places some perspective on the relative balance between experiment and analysis.

1. Fracture Initiation

Identification of the material properties associated with fracture initiation due to a single water drop impact (fracture threshold).

Identification of the material properties associated with fracture initiation due to multiple water drop impacts below the single water drop fracture threshold.

Identification of the material properties controlling fracture initiation and growth at water drop impact velocities well above the single water drop fracture threshold.

Evaluation of the change in the fracture response due to modification of a controlling material property.

Development of a model for fracture initiation.

2. Crack Growth

Identification of the material properties controlling crack growth.

Evaluation of the change in crack growth and crack morphology due to modification of a controlling material property.

1

Evaluation of the relation between crack growth and morphology and infrared transmittance.

Development of a model for crack growth.

3.   Erosion Pit Nucleation and Growth

Identification of the erosion mechanisms responsible for mass removal (erosion pit nucleation).

Identification of the material properties controlling the erosion process (erosion pit growth).

Evaluation of the change in erosion rate and erosion pit morphology due to modification of a controlling material property.

Evaluation of the relation between erosion pit growth and morphology and infrared transmittance.

Development of a model for the general erosion process.

Development of a model for the prediction of the degradation of infrared transmittance.

Not all of the above tasks are relevant for the specified impact conditions nor have all that are relevant been addressed in this study. For example, the first two tasks on fracture initiation are not directly applicable, since the fracture threshold for zinc sulfide is already exceeded at the minimum velocity of interest (222 ms^{-1}). Erosion pit growth was not investigated extensively, since the objective of the program can be satisfied without pursuing this complex subject. Analytical and experimental investigations of the events leading to material removel (the incubation period for erosion pit nucleation) are sufficient for providing the desired material guidance for the development of more erosion resistant windows. The primary emphasis of the program was on crack growth and to a lesser extent on the events leading to erosion pit nucleation. The relevant velocity range for this investigation determined from an initial overview of water drop impact damage as a function of impact velocity reported in Section III.2 is from 342 to 512 ms^{-1} (1120 to 1680 fps).

2

Water drop impact experiments were carried out on CVD zinc sulfide specimens in the ETI Liquid Drop Impact Facility and are described in Section III.1. This facility provides controlled and well characterized impact conditions. The water drops fall from the tip of a hypodermic needle and have diameters in the range from 1.5 to 2 mm. Although many of the qualitative aspects of the rain erosion response of brittle materials are known, the water drop impact experiments on CVD zinc sulfide are useful for they provide specimens for detailed materials characterization in order to identify the dominant surface features and microstructural properties which influence fracture initiation and growth.

Mathematical analyses of water drop impacts on an elastic target with and without a surface crack have been formulated. The general analysis is based on Green's theorem formulated for the convolution of the displacement vector and the stress tensor. It was initially thought that the extension suggested by Hackworth and Kocher (1978) of the TURBAN computer program could be used to generalize Blowers' analytic solution for the stresses in an elastic half-space due to a water drop collision (Blowers, 1969). It was found upon closer examination that this extension is quite restrictive and in fact in the form suggested is not valid for the pressure distribution used by Blowers. A simple generalization of this work is easily found, however, which is valid for Blowers' pressure distribution but the resulting distribution is still so restrictive that this extension of Blowers' work cannot be usefully incorporated into the present program as originally proposed. This led to an independent effort to provide an analytic generalization of Blowers' work in conjunction with consideration of crack growth in a transient stress field.

An analytic formulation of the crack growth problem in materials subject to water drop impact is developed which does not involve explicit numerical integration of the equations of motion. The latter approach, while straightforward, has a number of disadvantages not the least of which is the large expense for the required computer time. Other disadvantages include the lack of transparency of the solution with regard to parametric variation and, at a more fundamental level, the problem of disentangling

3

subtle physical effects from numerical artifacts of the finite grid size used. In explicit numerical studies, parametric studies are done by generating several solutions for a range of values of the parameters, a procedure which is usually impractical for more than one or two parameters because of the great expense involved, for example, in finite difference schemes. Nevertheless, it is often the case that explicit numerical schemes are the only alternative (particularly in the case of nonlinear problems for which analytic techniques are generally lacking) and, irrespective of the expense, they do have the distinct advantage that solutions can always be found provided the singularities of the solution are understood.

For linear or quasilinear problems the possibility exists, at least in principal, for obtaining analytic solutions to the problems in question. Analytic is used in the sense that it includes the use of numerical methods for evaluating integrals and summing series, but excludes the use of large grids of values of the independent and dependent variables. It is the use of the latter which accounts for the large cost of the explicit numerical schemes. The two approaches are complimentary in many respects. Parametric dependence is made explicit by analytic solutions and approximations made to achieve a solution are usually better understood so that the accuracy of the solutions obtained can be better assessed. For interesting problems, on the other hand, analytic solutions are almost always more difficult to obtain. If found, however, they provide more information at less expense than do the explicit numerical methods. For this latter reason, it is always advantageous to expend some effort on any problem to determine if at least an approximate analytic solution can be found before undertaking the development of an explicit numerical solution. Even if the analytical approach does not yield a solution, one usually benefits from the effort by achieving a better understanding of the problem, in particular the singularities, which helps to understand the numerical results generated by the explicit schemes.

SECTION II

MATERIALS

All of the formulations of chemically vapor deposited (CVD) zinc sulfide (ZnS) investigated were produced by the Research Division of Raytheon Corporation. A baseline material was supplied by AFML which was fabricated as a FLIR window. The piece of material received was designated Plate A, Run No. MT-207, Section B-2, and was 62x104x17 mm thick. Subsequently Section G-2 was also received from Run No. MT-207. This material was selected as the baseline material since it has been characterized by the University of Dayton Research Institute (Graves, et al., 1977; Wimmer and Graves, 1977, 1978; Wimmer, 1979). This sample will be referred to as material A in this report. According to Wimmer and Graves (1977) it was deposited at 640°C for 250 hours.

Additional formulations of zinc sulfide have been received from the Research Division of Raytheon Corporation for the purpose of investigating the influence of different microstructures on water drop impact damage. Two of the additional formulations deposited at 690 and 728°C (Material B and C, respectively) were investigated. No physical or mechanical property data have been received for these materials.

1. INITIAL CHARACTERIZATION

Materials A and B are amber in color, while Material C has a milky yellow appearance. Visual inspection of these materials reveals bands of color change and differing inclusion concentrations parallel to the deposition plane.

Table 1 is a summary of the characterization data generated by Wimmer and Graves (1977) and Wimmer (1979) for material A. Microhardness measurements were made on the polished surfaces of the specimens used in the water drop impact tests. The results are presented in Table 2.

TABLE 1. Properties of CVD ZnS, MT-207,
Plate A* (Material A).

Lattice Parameter	5.409 $\overset{\circ}{\text{A}}$
Density	4090 kg/m^3
Grain Size	8-10 µm in growth plane; up to 60 µm (columnar) in growth direction
4-Point Bend Strength	100.8 MPa (14.6 ksi)
K_{IC}**	0.67 MN/m$^{3/2}$ (609 psi $\sqrt{\text{in}}$)
Weibull Parameters (surface flaw model)	σ_o = 29.0 x 10^6 (dimensions in meters, stress in pascals)
	σ_o = 14.3 x 10^3 (dimensions in inches, stress in psi)
	m = 6.07
Knoop Hardness (100 g load)	239 kg/mm^2 (growth plane)
Young's Modulus	74.1 GPa (10.7 x 10^6 psi)
Poisson's Ratio	0.30 (in plane of plate)
	0.35 (in growth direction)
Calculated Dilatational Wave Velocity	4,960 ms^{-1}
Calculated Distortional Wave Velocity	2,600 ms^{-1}
Thermal Expansion	6.33 x 10^{-6}/°K (-67°C to 25°C)
	7.42 x 10^{-6}/°K (25°C to 200°C)
Thermal Diffusivity	0.09 cm^2/sec (25°C)
Thermal Conductivity	0.146 w/cm/°K (25°C)
Specific Heat	0.40 j/g/°K

*Taken from Wimmer (1979).
**Crack propagation parallel to columnar grains.

TABLE 2. Knoop Microhardness Measurements (100 g Load)

MATERIAL	KNOOP HARDNESS	STANDARD DEVIATION
A	238 kg/mm^2	5 kg/mm^2
B	244 kg/mm^2	8 kg/mm^2
C	194 kg/mm^2	8 kg/mm^2

TABLE 3. Characteristic Grain Dimensions
for CVD ZnS Formulations Investigated.

	AVERAGE LINEAR INTERCEPT (μm)		
	MATERIAL A	MATERIAL B	MATERIAL C
Growth plane	3-4	3-5	5-10
Cross section perpendicular to growth plane in the direction perpendicular to growth plane	5-30	5-30	10-100
Aspect ratio range	1.25-10	1-10	1-20

General grain structure and growth patterns were investigated by chemically etching polished surfaces. The etchant was equal parts concentrated HCl and H_2O at 45°C. Etching time was 1 minute. Surfaces both parallel and perpendicular to the growth plane were etched. Representative grain structure micrographs are shown in Figure 1 for Material A. Materials B and C exhibited the same qualitative features shown in Figure 1.

Due to the highly anisotropic nature and local variations of the grain size and structure, an average grain size dimension is somewhat meaningless. Average intercept distances were measured both in the growth plane and perpendicular to it for quantitative comparison of the grain sizes in these materials. The grains appear equiaxed in the growth plane but columnar in the perpendicular plane as can be seen in Figure 1. The intercept distances are given in Table 3. No difference in grain structure was noted between Section B-2 and G-2 for the baseline material.

In addition to having columnar grain morphologies, the three ZnS formulations exhibited local grain structures which will be referred to as haystacks which describes their general appearance. Examples of the haystack grain growth patterns are shown in Figure 2. A haystack consists of a nucleation site and localized distortion of the characteristic columnar grain growth pattern. At the nucleation site, the major axes of the grains radiate out into the half space above the growth plane. As more grains are formed, their major axes tend to approach the growth direction leaving the haystack structure. Partially developed haystack structures appear to have been noticed by Graves, et al. (1977), in thin zinc sulfide layers deposited on zinc selenide substrates. They were referred to as rosettes by these investigators. The haystack structures nucleate at clinker and rod inclusions. These inclusions, which have a maximum size on the order of 100 µm, tend to exist in growth bands parallel to the growth plane. The inclusions are of a larger average size (c. 80 µm) in material C and approximately ten times more numerous than in material A or B (average size c. 50 µm).
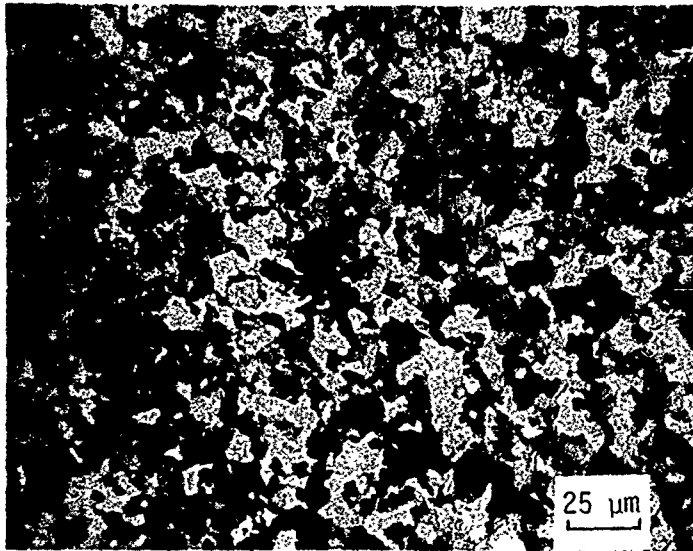
a. Growth Plane

Growth
Direction
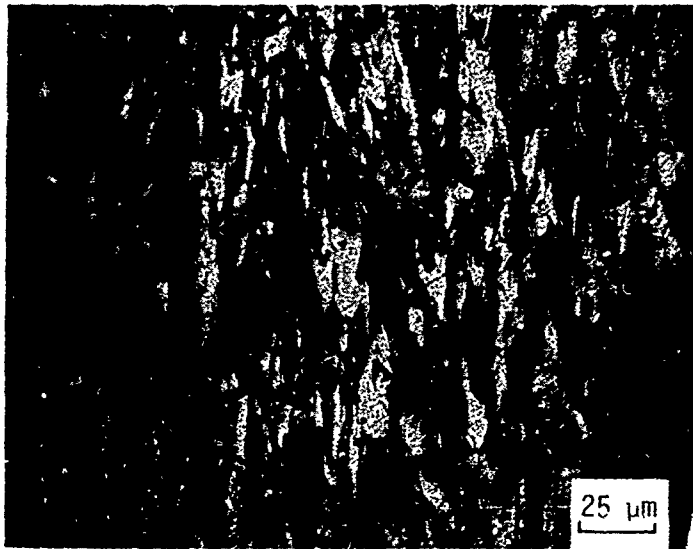
b. Section Perpendicular to Growth Plane

Figure 1. Appearance of Columnar Grains in Material A (Baseline).

a. Haystack Structure in Material C.
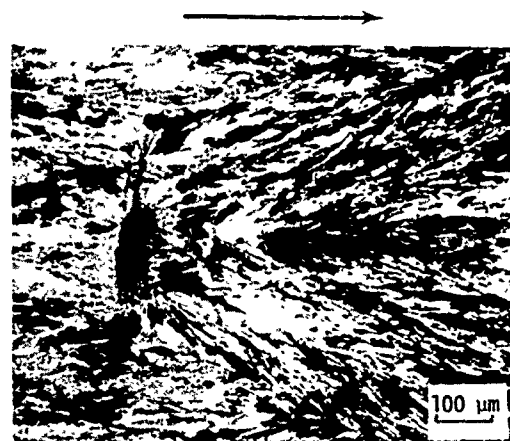
b. Nucleation site of a Haystack Structure at a Clinker Inclusion.
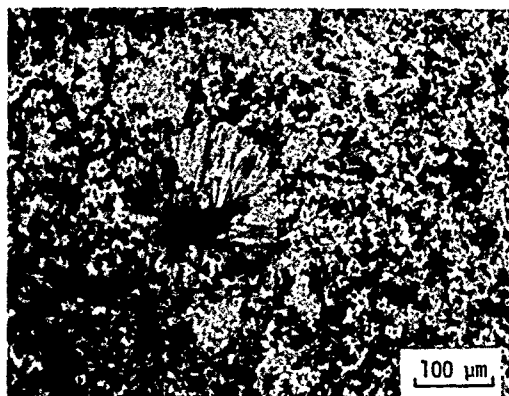
c. Growth Plane Section at the Nucleation Site of a Haystack Structure in Material A.
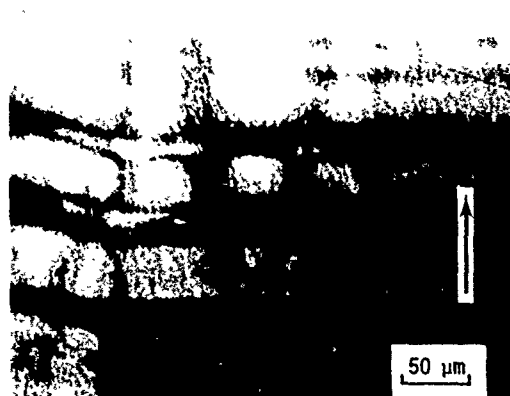
d. Transmitted Polarized Light View of Material A Showing the Haystack Structure and Deposition Bands of Differing Grain Texture.

Figure 2. Examples of Microstructural Features in CVD ZnS. (Arrows indicate growth direction.)

In addition to bands of inclusions all materials exhibited bands of altered grain structure. These bands can be seen in Figure 2d photographed in transmitted polarized illumination.

2. SAMPLE PREPARATION PROCEDURES

Specimens for water drop impact were fabricated in the form of right circular cylinders 17 mm diameter by 12 mm thick. The specimens of material C were only 4 mm thick due to limited plate thickness.

The circular impact faces were oriented parallel to the growth plane, and then mechanically polished to optical quality by A.M.F. Optics, Inc., Woburn, MA. Additional specimens with their impact faces oriented perpendicular to the growth plane were prepared at ETI.

In the initial phases of the program all of the impact specimens were polished at ETI. These surfaces were found to contain excessive polishing induced flaws which interacted strongly with the impact loading. The quality of the surface finish achieved at ETI with further polishing experience has approached the level supplied by A.M.F. Optics, Inc.

3. POST-TEST EXAMINATION PROCEDURES

After impacting a water drop in the ETI Liquid Drop Impact Facility, the specimen is carefully removed from the sabot (the experimental procedure is described in Section III.1). Recovery debris are removed with methanol alcohol in a low energy ultrasonic cleaner followed by a methanol and then ether rinse. The major fractures and outflow damage are photographed in both reflected and transmitted illumination for future reference. The specimen is typically etched (50% HCl @45°C) to reveal the fine surface fractures present. The enhanced fracture pattern is then photographed. The subsurface morphologies of the fractures are revealed by sectioning the specimen on a plane that is perpendicular to the impact plane and passes through the center of the impact. The sectioning is accomplished by first encapsulating the impact face with Buehler mounting epoxy. The sectioning

process involves rough material removal by wet sanding with progressively finer grits of SiC paper, terminating with 5 μm Al_2O_3 in water on nylon. This is followed by removal of approximately 100 μm of material with 0.3 μm Al_2O_3 in water on nylon and finally polishing the desired section with .05 μm Al_2O_3 on silk wet with 50% HCl. This sectioning method exposes the internal fractures essentially undisturbed for optical microscope examinations using various illuminations.

The finer details of the fracture/grain structure interactions on the impacted face of the specimen are observed from etched surfaces using scanning electron microscopy. Surface replication procedures were used to examine the details of the damage within surface grains using transmission electron microscopy.

SECTION III

WATER DROP IMPACTS

This program concentrates on understanding water drop impact damage in CVD zinc sulfide. The surface loading conditions associated with a water drop collision are still somewhat ill-defined, although advances are being made in analyzing water drop collisions at high subsonic to low super-sonic impact velocities (Adler, 1979a). Since the water drop impact conditions are not well defined quantitatively, the nature of the loading condition as well as the response of the target becomes an integral part of the general problem. The ETI Liquid Drop Impact Facility currently provides ideal (spherical) water drop impacts at velocities from 222 to 684 ms^{-1} (730 to 2240 fps) along with well-documented data on individual drops just prior to collision with the target.

The operation of the ETI Liquid Drop Impact Facility is described in Section III.1. The system components and instrumentation used in the facility were for the most part drawn from what was readily available. Quite accept-able results are presently obtained in this facility as shown in Section III.2. The potential exists, however, for enhanced and extended capability through additional modifications and component upgrading. These modifications are being made as justified. The mechanics of water drop collisions required for better understanding of the internal fracture observations reported in Section III.2 is described in Section III.3.

1. DESCRIPTION OF LIQUID DROP IMPACT FACILITY AND PROCEDURES

A schematic of the ETI Liquid Drop Impact Facility is shown in Figure 3. The specimen is mounted at the front end of a sabot which is propelled down the range by a small charge of gunpowder. Water drops are formed at the tip of a hypodermic needle mounted above the test section and fall in the path of the moving specimen. A slotted rail system is used to guide the sabot through the test section and into the recovery tube. As a single drop falls from the tip of the hypodermic needle it interrupts dual fiber optics links above the test chamber thereby initiating the firing sequence. The system is calibrated so the sabot reaches the drop when it has fallen to a point within the limits of the exposed surface of
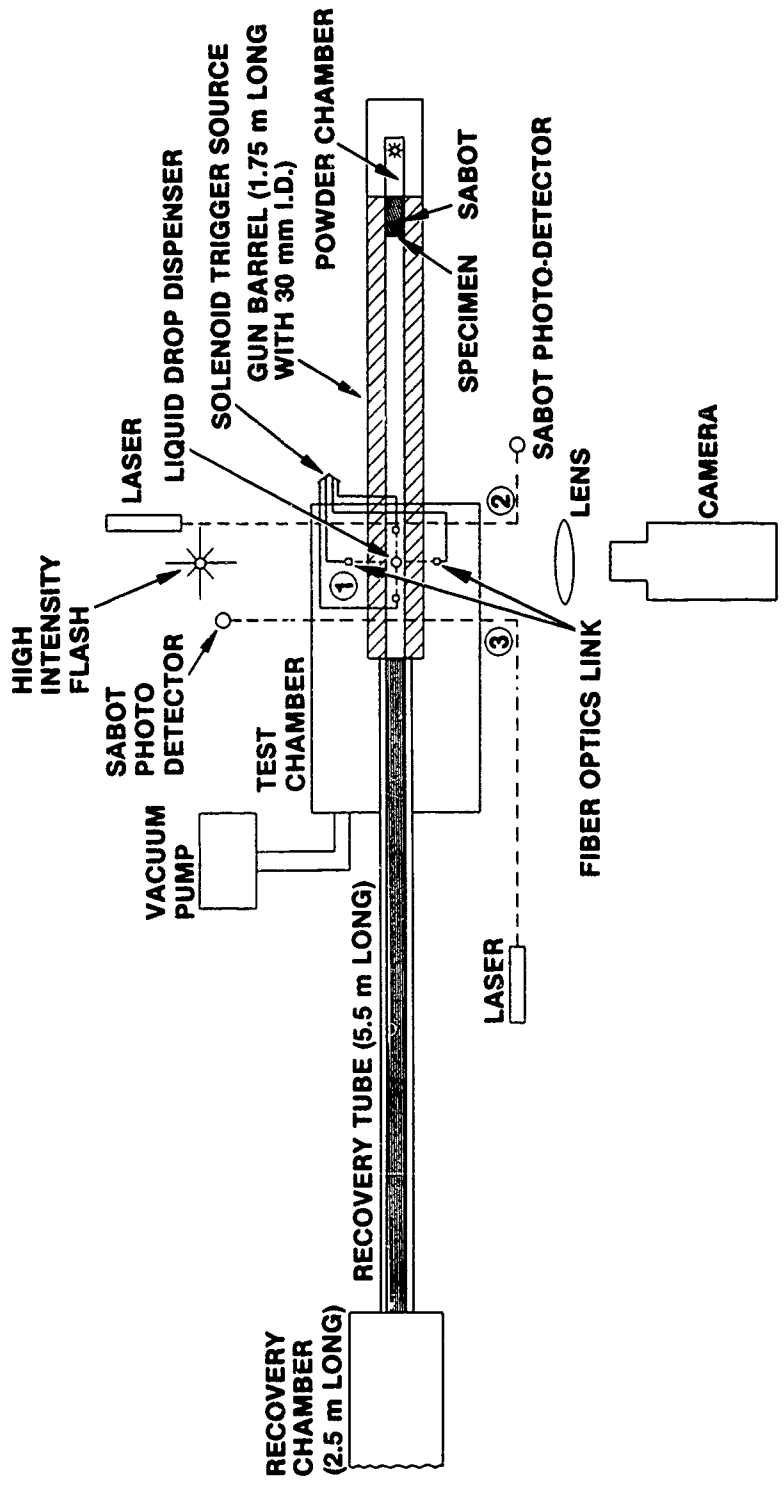
Figure 3. Liquid Drop Impact Facility.

14

the specimen. After impacting the water drop the sabot enters the recovery tube where a graded distribution of material controls the deceleration of the sabot and protects the face of the specimen from extraneous damage.

The barrel of the powder gun has an inside diameter of 30 mm and is capable of accelerating the sabot to a maximum speed of 1370 ms^{-1} (c. 4500 fps). Circular specimens up to 22 mm (0.875 in.) in diameter can be accommodated with the existing sabot configuration. Non-circular specimens with lateral dimensions less than 22 mm and a wide range of thicknesses can also be used. The zinc sulfide specimens used in this program are 17 mm in diameter and range from 6 to 10 mm thick. These dimensions are adequate to avoid edge effects and to eliminate any stress wave interactions with the water drop impact damage due to stress wave reflections from the back face of the specimen. Specimens of zinc sulfide can be recovered after water drop collisions over the velocity range of interest, 222 to 684 ms^{-1} (730 to 2240 fps corresponding to an aircraft traveling at 500 mph through mach 2), without cracking the specimens or producing additional damage which obscures that due to the drop impact. As shown in Figure 3 the total length of the recovery system is only 8 m (26 ft.). The extent of the water drop impact damage on zinc sulfide over this velocity range is described in Section III.2. Multiple water drop impact damage can be obtained by sequential firings of the same specimen down the range. Only a few interacting drop impacts are required at 342 ms^{-1} (1120 fps) to significantly degrade the infrared transmittance of zinc sulfide. The ETI facility (described more fully by Adler and James, 1979) is ideally suited for documenting each drop impact in conjunction with its effect on the general degradation process.

The tests were conducted in a helium atmosphere at an ambient pressure of 300 μm Hg in order to minimize distortion of the drop caused by the bow shock prior to impact with the specimen's surface. This effect is distinct from that of blow-by which results from the expansion of the gases associated with the gunpowder burn. Escape of these gases generated by the detonation of the gunpowder has been eliminated by means of a self-sealing sabot configuration. A considerable developmental effort has been completed to maintain

the integrity of the water drop and to minimize its aerodynamic distortion prior to impact. While shock wave and boundary layer effects are an integral part of the erosion problem for supersonic aircraft, the drop geometry prior to impact in actual flight environments is an aerodynamic problem. The intent here is to understand the material's response to water drop collisions which requires a reproducible and relatively simple drop geometry.

In order to operate at pressures well below the vapor pressure of water, a solution of 80 volume percent of distilled water and 20 volume percent ethylene glycol ($C_2H_6O_2$) is used. From a pragmatic viewpoint this solution behaves essentially the same as pure water during the collision process.

The water-glycol solution is deaerated. The temperature of the solution is typically slightly below room temperature: approximately 15°C. Chilling the solution has the advantage of lowering the vapor pressure, but this advantage has to be balanced against an increase in viscosity. The deaerated water-glycol solution is placed in a reservoir above the test chamber where it is drawn into a vertically mounted syringe. Manually applied pressure to the syringe initiates drop formation at the tip of the hypodermic needle. If the drops are forming satisfactorily at the test pressure when viewed through an optical microscope with a magnification of about seven times, a single drop is photographed as it falls between the guide rails at the elevation of the specimen. The integrity and general appearance of the drop is checked from this photograph. If it passes this visual inspection, the pressure in the system is checked to confirm that it matches the desired test pressure, the pre-set firing sequence is unlocked, and detonation of the gunpowder takes place as a subsequent drop interrupts the dual fiber optics links passing above the test chamber corresponding to station ① in Figure 3. When the sabot is 25 mm from the impact point, it passes through a laser beam at station ② which sends a pulse to a delay generator which subsequently triggers a flash unit to photograph the drop prior to impact. The delay circuit

allows the drop to be photographed as close to the impact site as the jitter in the system will permit. In all cases this photograph will record the water drop when the specimen is less than 25 mm away. Stated differently, the sabot will be a maximum of 113 μs away from impacting the water drop when traveling at 222 ms^{-1} and 36 μs away for a 700 ms^{-1} impact condition. The velocity of the sabot is measured by the length of time required for the sabot to pass through the laser at station ② in Figure 3. Knowing the length of the sabot and this time, the velocity can be calculated. A second determination of the impact velocity is made by measuring the time required for the sabot to pass through laser beams ② and ③ in Figure 3. The distance between these stations divided by the recorded time increment yields a second value for the impact velocity.

During the initial phases of this investigation the water drops were tending toward ellipsoidal shapes prior to colliding with the specimen due to the interaction with the gas remaining in the gun barrel. The pumping capability was subsequently improved. At a system pressure of 100 to 200 μm Hg in a helium atmosphere, the drop distortions appear to be negligible prior to impacting the specimen. A series of tests were carried out for confirmed spherical water drop impacts as shown in Figure 4. The significance of ellipsoidal drop collisions compared with spherical drop impacts will be considered along with the nature of the loading conditions for spherical water drop collisions on ZnS.

2. OVERVIEW OF WATER DROP IMPACT DAMAGE

Water drop impacts have been obtained on the three ZnS materials described in Section II.1, and additional impacts were obtained on specimens from an unidentified ZnS FLIR window over the velocity range from 222 to 684 ms^{-1}. The complete range of test conditions and the general features of the resulting impact fractures will be described.
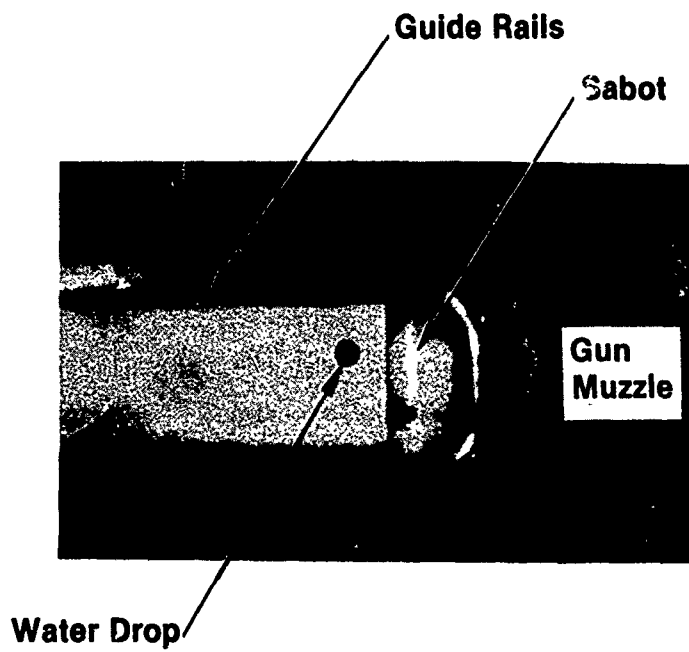
Figure 4. Typical Appearance of Water Drop Prior to Impact for Impact Velocities from 200 to 700 ms^{-1} at a Pressure of 0.1 torr or less.

a.   Test Conditions

Tables 4 and 5 list the impact conditions for each test carried out within this program.

The impacts obtained from the initial sequence (Table 4) were for surfaces prepared at ETI. At the time the initial test sequence was under-taken the drops were deforming to ellipsoidal shapes prior to impact, how-ever the water drop impacts listed in Table 5 are for confirmed spherical drop collisions. An ellipsoidal drop will be considered equivalent to a spherical drop when they have the same mass. Let b_1, b_2 be the semi-major and semi-minor axes of the ellipsoid, then the equivalent spherical drop radius r_o is determined from the relation

$$r_o = \sqrt[3]{b_1^2 b_2} \qquad (3.1)$$

The equivalent drop diameter is calculated using the dimensions measured from the photographs of the drop prior to impact as shown in Figure 4. The ratio of the major to minor axis of the elliptical cross section is listed in Table 4 to provide a measure of the distortion which occurred. The influence ellipsoidal drop impacts have on the magnitude of the ob-served damage will be examined in Section III(a). The missing entries under the heading b_1/b_2 are for shots in which the drop was already obscured by the sabot when the photograph of the drop prior to impact was taken; for these cases which arise due to the inherent jitter in the system the diameter of the pretest drop is used for the equivalent spherical drop diameter.

Improvements in the ETI Liquid Drop Impact Facility were made during the early stages of this program which eliminated drop distortions prior to impact: spherical drop impacts are now obtained at all impact velocities. A second series of water drop impact tests were carried out for this condi-tion for optically polished surfaces as listed in Table 5. The nature of the impact damage during the initial sequence did not show any change in its general form over the velocity range from 237 to 640 ms^{-1}, so the second test series concentrated on two impact velocities: 342 and 512 ms^{-1} corresponding to mach 1 and mach 1.5.

19

TABLE 4. Summary of Water Drop Impacts on Zinc Sulfide (Initial Sequence).

SHOT NO.	MATERIAL	IMPACT VELOCITY ms^{-1} (fps)	EQUIVALENT DROP DIAMETER mm	b_1/b_2	REMARKS
803	FLIR	512 (1680)	1.82	1.32	Specimens from unidentified
805	FLIR	259 (850)	1.60	1.54	FLIR window material
813 *	A(B-2)	368 (1205)	1.56	1.67	
815 *	A(B-2)	237 (776)	1.60	1.54	
819 *	A(B-2)	518 (1700)	1.78	1.24	
836 *	A(B-2)	640 (2100)	1.96	1.18	
838 *	A(B-2)	372 (1220)	1.91	--	Impact face along deposition direction
839	A(B-2)	350 (1150)	1.97	1.50	
845	C	332 (1090)	1.79	--	
847 *	C	350 (1150)	1.85	--	Chemically etched surface
851	A(B-2)	506 (1662)	2.16	c. 1.00	
852	A(B-2)	363 (1190)	2.14	1.12	Chemically etched surface
853	A(B-2)	332 (1088)	2.19	1.22	Chemically etched surface
854	A(B-2)	262 (860)	2.28	—	Chemically etched surface, impact face along deposition direction

*Specimens sectioned for microscopic observation.

20

TABLE 5. Summary of Spherical Water Drop Impacts on Zinc Sulfide.

SHOT NO.	MATERIAL	IMPACT VELOCITY ms^{-1} (fps)	DROP DIAMETER mm	REMARKS
971 *	A(B-2)	515 (1690)	1.62	Estimated velocity
978 *	C	512 (1680)	1.68	
985 *	A(B-2)	510 (1673)	---	
1011	C	345 (1132)	1.60	Overexposed photograph of drop
1012	A(G-2)	336 (1104)	1.62	
1016 *	A(B-2)	331 (1087)	1.70	
1017 *	C	338 (1110)	1.56	
1036 *	B	299 (981)	1.70	
1038 *	B	517 (1695)	1.72	
1040	FLIR	401 (1314)	2.02	
1041	FLIR	497 (1629)	2.10	
1042	FLIR	594 (1950)	2.10	
1048	FLIR	516 (1692)	2.10	
1049	A(G-2)	518 (1699)	2.10	First impact in multiple sequence
1050	FLIR	600 (1968)	2.10	Second impact in multiple sequence
1051	A(G-2)	505 (1658)	2.10	Third impact in multiple sequence
1052	A(G-2)	514 (1703)	2.14	

*Specimens sectioned for microscopic examination.

To our knowledge single water drop impacts on zinc sulfide, or zinc selenide, above 342 ms^{-1} (1120 fps) have not been investigated. Hackworth and Kocher (1978) have reported single drop impacts on ZnS and ZnSe at velocities to 340 ms^{-1}. Their experimental facility does not allow verification of the drop sizes and shapes. A number of multiple drop impact sequences have been reported in their work (Hackworth and Kocher, 1977, 1978). A series of interacting spherical drop impacts at 512 ms^{-1} was initiated in order to assess the erosion pit nucleation process at this higher velocity (shot numbers 1049, 1051, 1052). However shortly after obtaining these three shots, the quality of the impacts was declining due to gun barrel erosion which did not allow the gases generated by the gunpowder burn to be completely sealed by the sabot. The gun barrel is being replaced, so the multiple impact sequence has been terminated until the previous high level of perfection in the water drop collisions is once again achieved.

Qualitatively the nature of single drop impact damage in polycrystalline ZnS over the velocity range investigated (237 to 640 ms^{-1}) shows a characteristic fracture pattern whose extent depends strongly on the impact velocity. The characteristic fracture pattern as viewed in the direction of impact with transmitted illumination is apparent in Figure 5. Both the velocity dependence of damage and the characteristic cross sectional fractures due to single drop impacts can be seen in Figure 6. Figure 6 shows the dramatic difference in the extent of the damage for a water drop impact at 299 ms^{-1} compared with a drop impact at 517 ms^{-1}. The same magnification is used for both micrographs.

When viewed with reflected light single drop impacts characteristically appear as in Figure 7(a). Figure 7(b) is the same impact (as in Figure 7(a)) but photographed with transmitted illumination. In both transmitted and reflected illumination, it is apparent that the fracture pattern in Figure 7 has been altered by interaction with linear surface scratches. The surface of the specimen in Figure 7 (shot no. 836) is from the initial sequence which had a high occurrence of surface polishing scratches. The impact damage for the multiple impact sequence is shown in transmitted illumination in Figure 8.

200 μm
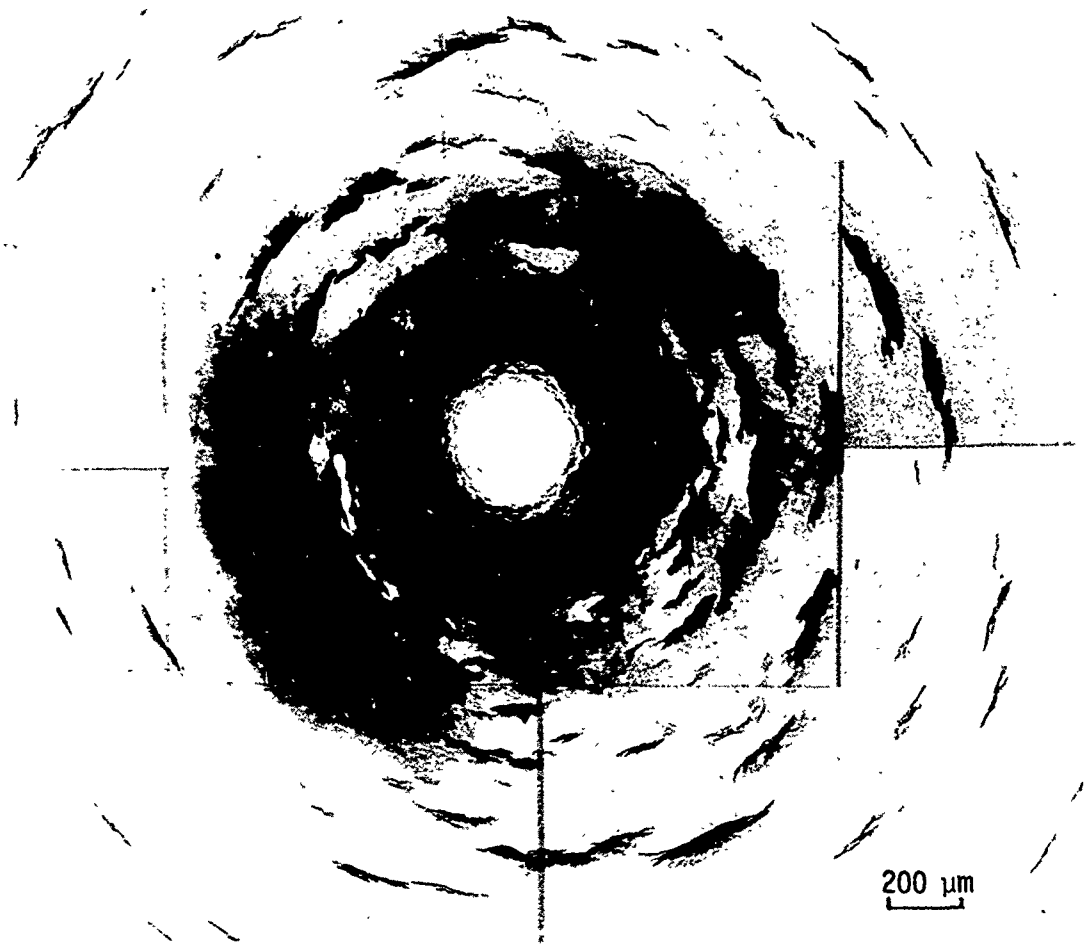
Figure 5. Shot No. 985 (Transmitted Light Illumination).
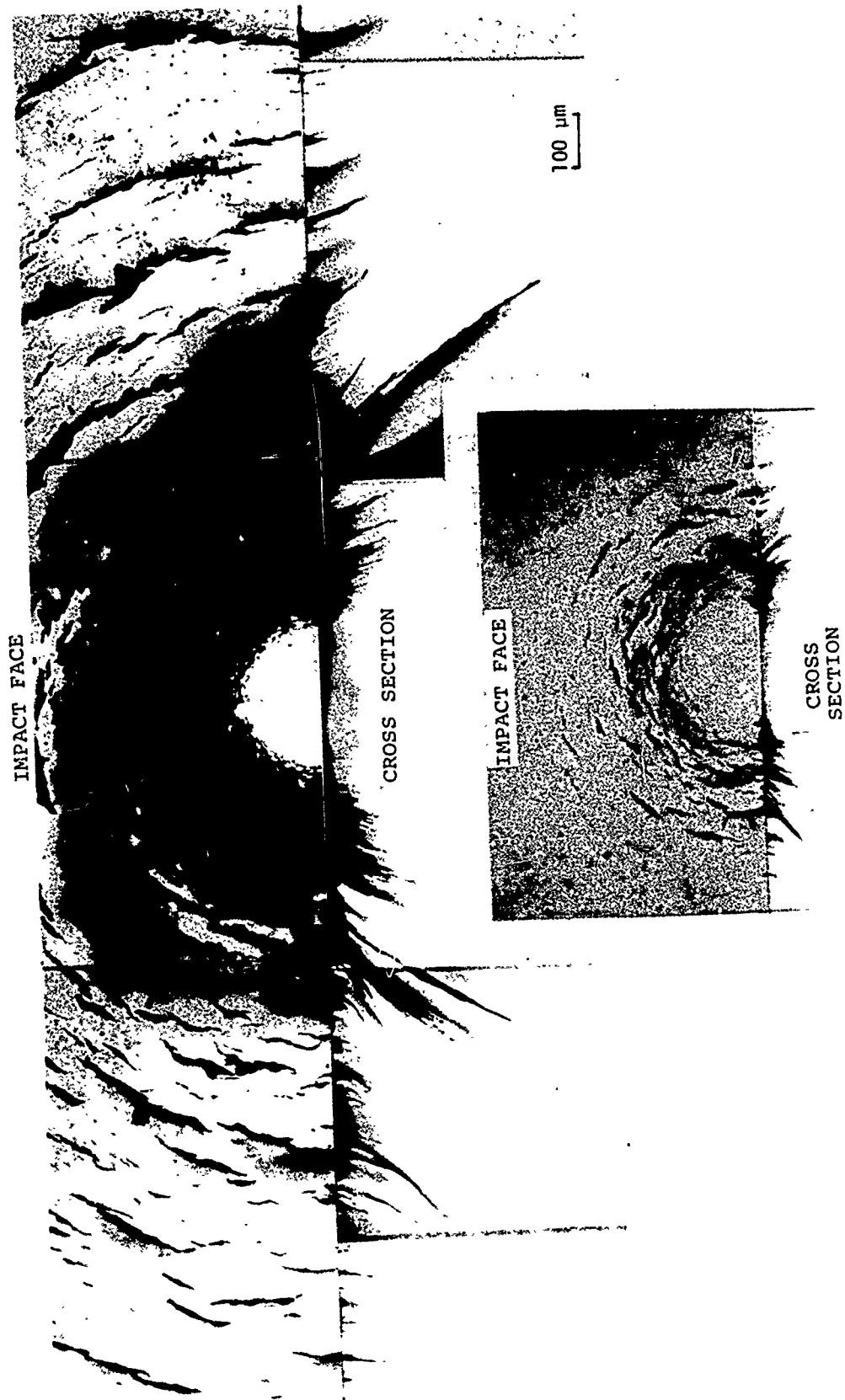
Figure 6. Comparison of Damage Produced at 299 ms^{-1} (Shot No. 1036) and 517 ms^{-1} (Shot No. 1038) as Seen on Impact Face and in Cross Section.
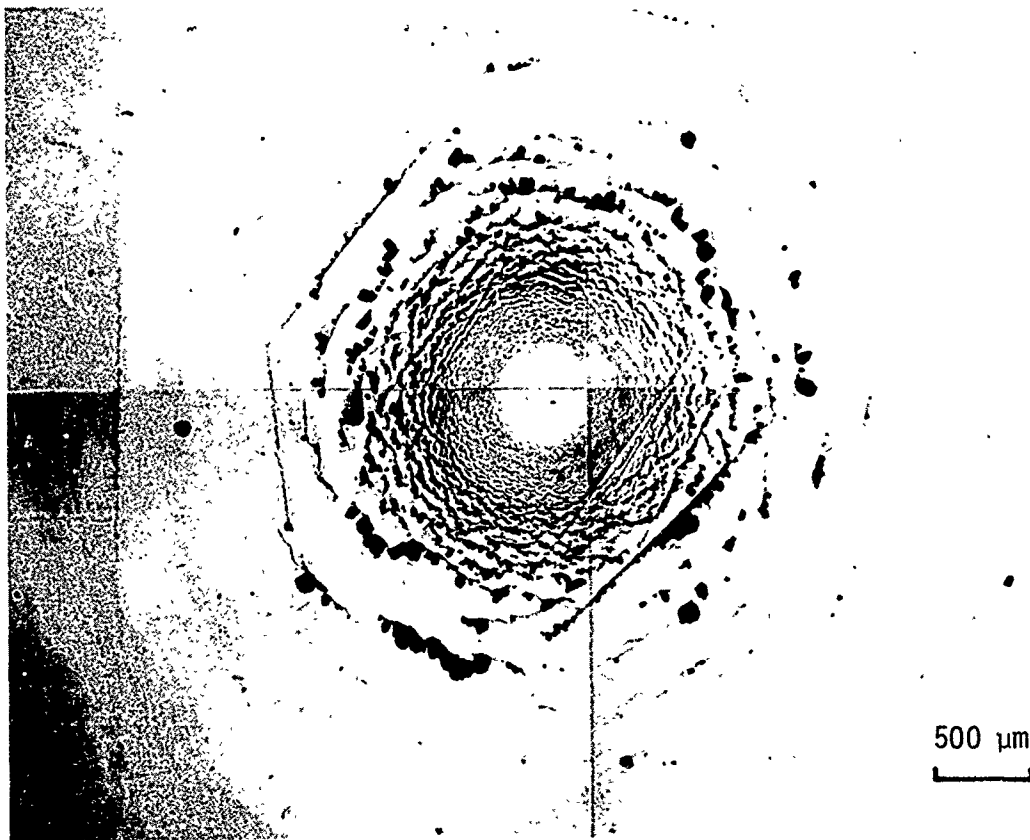
a) Photographed with Reflected Light Showing the
   Lateral Outflow Chipping Damage.

Figure 7. Impact Face of Shot No. 836 Impacted at 640 ms^{-1}.
Note Strong Interaction of Fracture Pattern with
Polishing Marks.

25

500 μm
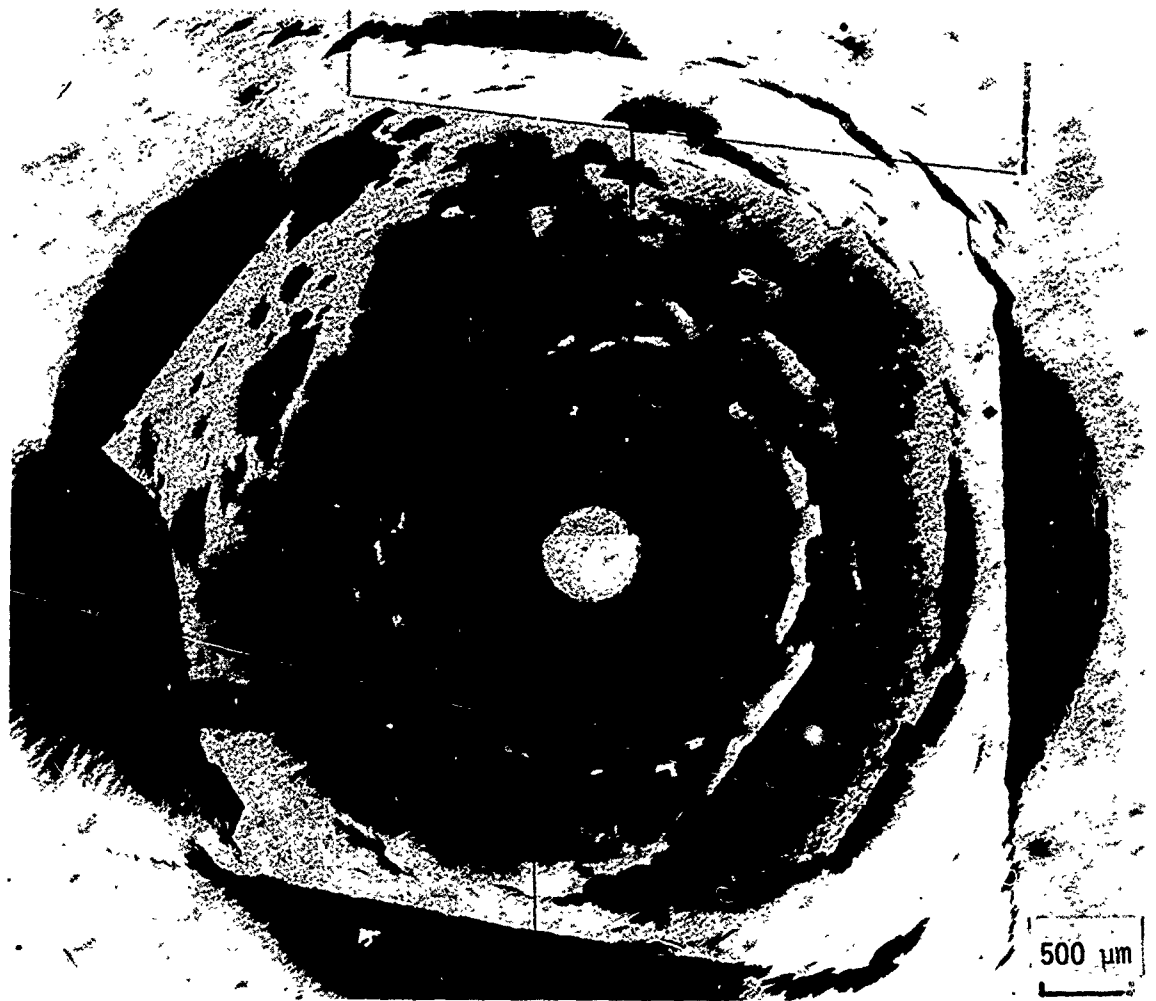
b) Photographed with Transmitted Light Showing
Radial Extent of Subsurface Fractures.

Figure 7. (continued). Impact Face of Shot No. 836 Impacted
at 640 ms^{-1}. Note Strong Interaction of Fracture
Pattern with Polishing Marks.
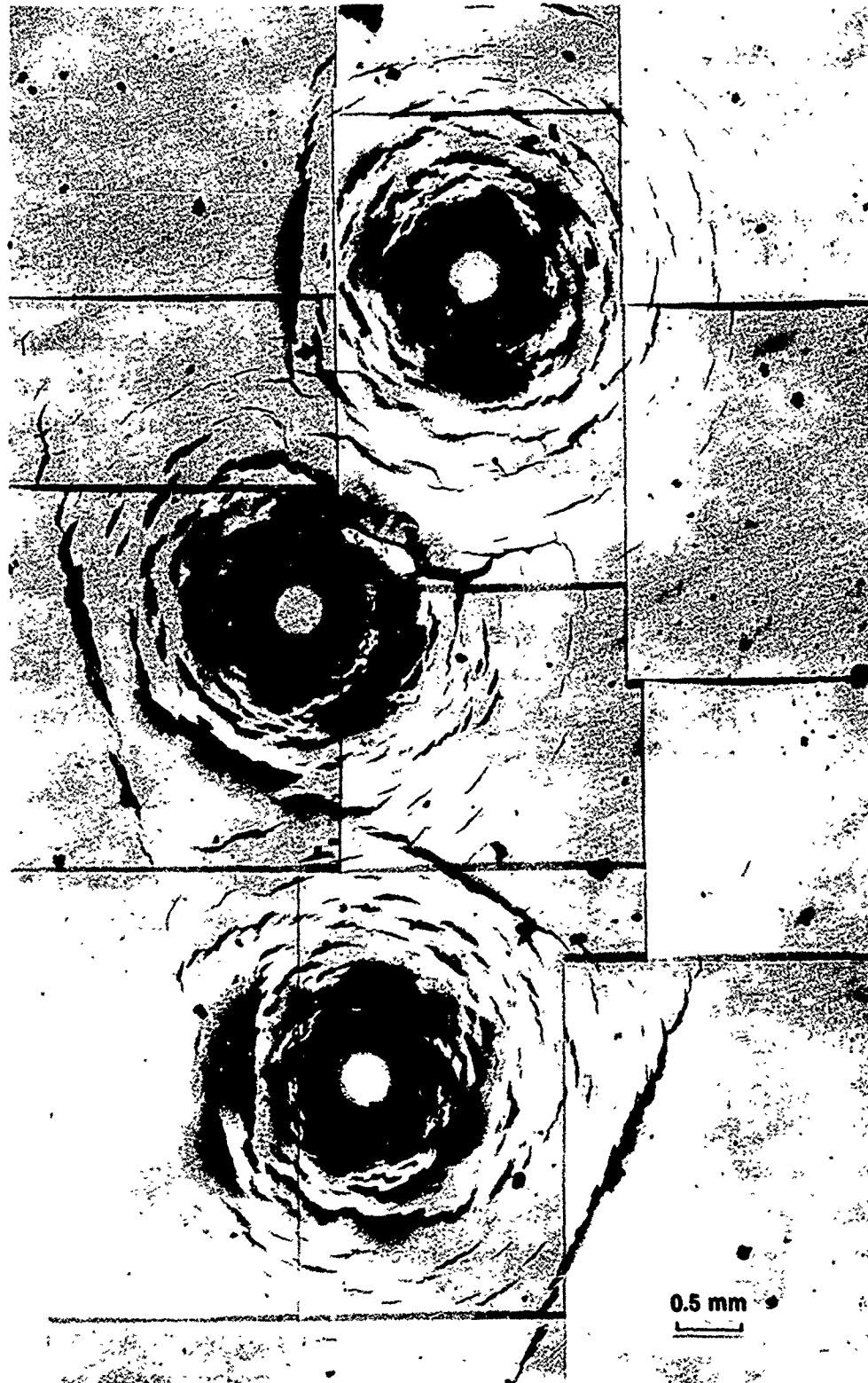
Figure 8. Multiple Water Drop Impacts on CVD Zinc Sulfide. 2 mm Diameter Drops Impacting at 510 ms^{-1} (Transmitted Light Illumination).

b.   Crack Morphologies and Dimensions

In order to obtain data on the nature of the fractures produced in
the interior of a specimen, cross sectional views on a plane normal to the
impact surface passing near and through the center of the damage zone are
employed. Three distinct fracture zones can be identified by the crack
trajectories observed in these cross sections. The three primary fracture
zones are believed to correspond to the nature of the surface loading con-
ditions and the resulting transient stress states within the target. The
fracture zones will be labeled numerically beginning at the point of impact
and moving outward in a radial direction.

A typical impact fracture pattern at Mach 1 is shown in Figure 9.
A portion of the impact face and the principal cross section is shown.
Readily visible in the center of this figure as a region free of fracture
is zone 1, alternatively called the central undamaged zone. The central
undamaged zone exists since the initial stresses within the material are
predominantly compressive (Adler, 1977).

Radially outward from the undamaged zone is an annulus of densely
spaced (both circumferentially as well as radially) fractures which in
cross section are monotonically increasing in depth with increasing radial
distance. The fractures adjacent to zone 1 are numerous and shallow ranging
from 3 to 50 μm in depth, which is on the order of the columnar grain dimen-
sions (Table 3).   Progressing radially outward the fractures become less
densely distributed, deeper, and approach the surface at a shallow angle
(that is, more nearly tangent to the surface). The cross sectional views
of the midplane fractures show a very distinct transition to fractures
which are nearly normal to the impact surface at the face of the specimen
and then penetrate the interior of the specimen in an initially concave
outward direction; however, if the penetration is deep enough, the frac-
ture path will exhibit a reversed curvature. Fracture paths with double
curvature (concave outward near the surface and concave in at greater
depths) are observed for all the velocities and appear to form a transi-
tion from the fractures which are essentially tangent to the surface to

IMPACT FACE

CROSS SECTION

100 μm
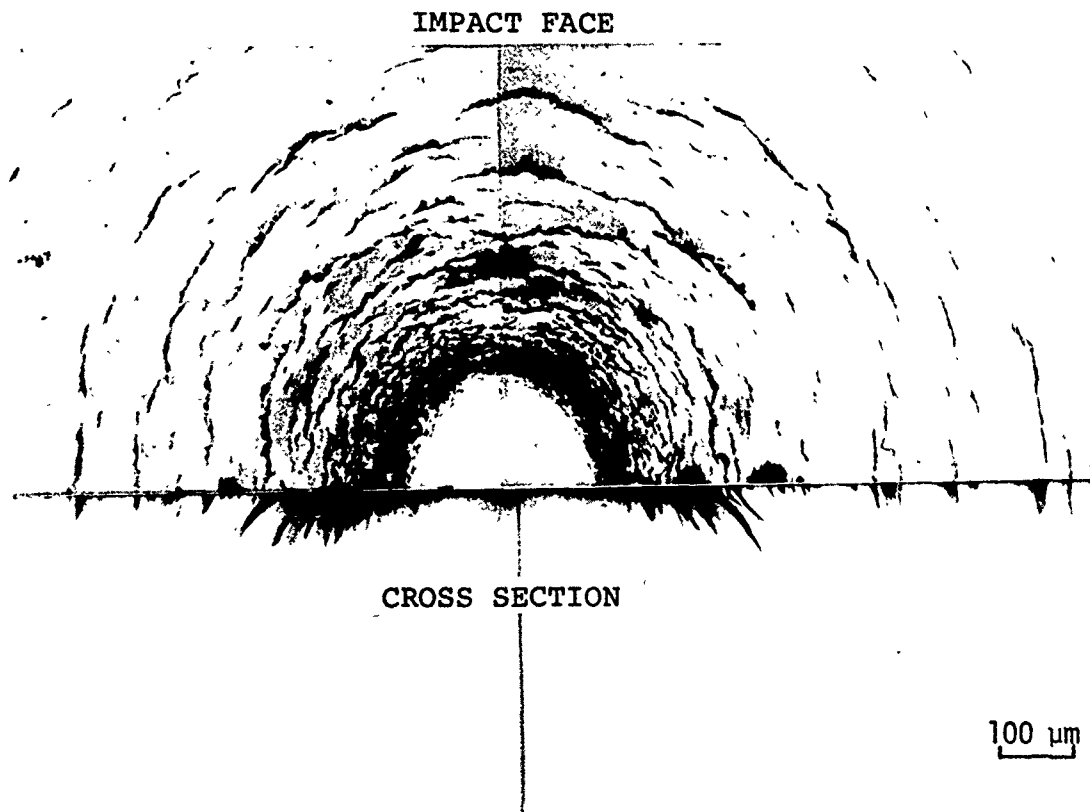
Figure 9. Impact Face and Cross Section of Shot No. 1016
(331 ms^{-1}) Showing Characteristic Fracture Zones.

those which tend to be more normal to the surface at larger radial distances. This fairly well-defined transition in the orientation of the fracture trajectories will define the outer boundary of zone 2. The general character of the fractures within zone 2 is shown in Figure 10. The deepest fractures occur predominantly at the outer radius of zone 2, or occasionally at the extreme inner radius of the next zone, zone 3. Zone 3 encompasses all of the fractures outside of zone 2.

The zone 3 fractures are characterized by a nearly vertical approach to the impact surface for the first 10 to 50 μm of depth depending on the impact velocity. The innermost fractures which are the deepest in zone 3 exhibit a double curvature as mentioned earlier which can be seen fairly clearly in Figure 6. The depth of fracture in zone 3 decreases initially quite rapidly and the fractures lose their double curvature becoming relatively shallow and both radially and circumferentially sparse.

In addition to bulk fracturing of the target material water drop impacts also produce lateral outflow chipping at the surface crack openings (Adler, 1979a). The chipping results from the impingement of the lateral outflow jets upon the outer upraised edges of the bulk fractures which are a characteristic feature of water drop impact fractures. The outflow chipping damage is most readily seen with reflected illumination as in Figure 7(a).

Characteristic dimensions of the radial extent and maximum fracture depths for the fracture zones were measured on the impacts which were sectioned as noted in Table 4 and 5. The dimensions of the various features of the impact damage described above are summarized in Tables 6 and 7. Due to the level of variability inherent in the fracture formation process, a considerably greater number of measurements would have to be made to provide statistical data which could then be used to interpret the trends in the observed fracture zones. The measurements in Tables 6 and 7 are simply intended to illustrate the velocity dependence of the characteristic features of the damage region which have been identified.
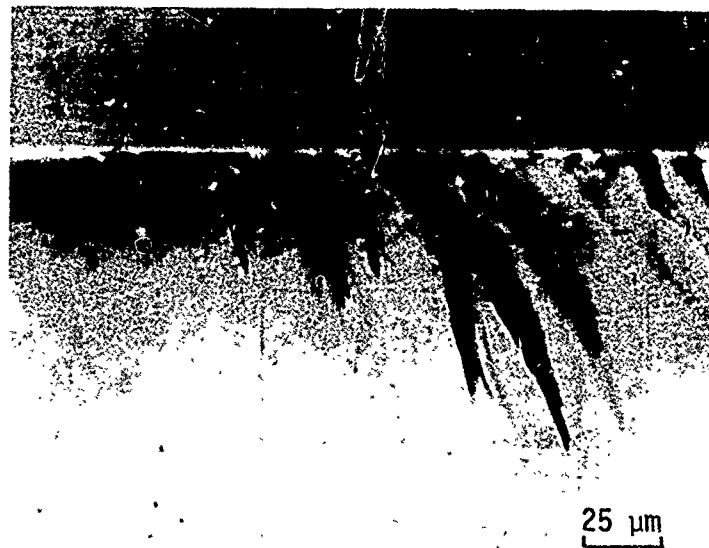
Figure 10.   Detail of Zone 2 Fractures for Shot No. 1016
(Shown in Figure 9).

TABLE 6. Summary of Water Drop Impact Damage Dimensions (Initial Sequence).

SHOT NO.	MATERIAL	VELOCITY (ms^{-1})	MAX.RADIUS OF ZONE 1 (mm)	MAX.RADIUS OF ZONE 2 (mm)	FRACTURE DEPTH MIN. (μm)	FRACTURE DEPTH MAX. (μm)	MAX.RADIUS OF ZONE 3 (mm)	FRACTURE DEPTH MIN. (μm)	FRACTURE DEPTH MAX. (μm)	LATERAL OUTFLOW RADII INITIATION (mm)	LATERAL OUTFLOW RADII TERMINATION (mm)
815	A(B-2)	237	0.13	0.25	3	20	0.40	--	40	--	--
813	A(B-2)	368	0.16	0.42	2	180	1.00	2	270	0.32	0.70
819	A(B-2)	518	0.18	0.65	10	520	2.30	8	320	0.46	1.15
836	A(B-2)	640	0.25	0.80	5	1200	3.80	10	1000	0.39	1.35
838	A(B-2)	372	0.18	0.40	5	280	1.20	10	240	0.20	0.85
847	C	350	0.14	0.40	5	150	1.10	10	200	0.30	0.80

TABLE 7.   Summary of Spherical Water Drop Impact Damage Dimensions.

SHOT NO.	MATERIAL	DROP DIAMETER (mm)	VELOCITY (ms^{-1})	MAX.RADIUS OF ZONE 1 (mm)	MAX.RADIUS OF ZONE 2 (mm)	FRACTURE DEPTH MIN. (μm)	FRACTURE DEPTH MAX. (μm)	MAX.RADIUS OF ZONE 3 (mm)	FRACTURE DEPTH MIN. (μm)	FRACTURE DEPTH MAX. (μm)	LATERAL OUTFLOW RADII INITIATION (mm)	LATERAL OUTFLOW RADII TERMINATION (mm)
10.6	A(B-2)	1.70	331	0.11-.125	0.26	5	90	1.00	10	100	0.23	0.56
985	A(B-2)	—	510	0.17	0.38	5	340	1.85	10	360	0.33	0.76
971	A(B-2)	1.62	515	0.13	0.40	4	320	1.85	15	300	0.30	0.90
1036	F	1.70	299	0.115	0.19	4	75	0.43	10	75	0.18	0.32
1038	B	1.72	517	0.160-.165	0.42	10	470	2.0	10	320	0.37	0.90
1017	C	1.56	338	.105-.11	0.275	2	130	0.80	10	100	0.20	0.45
978	C	1.68	512	.15-.16	0.36	10	300	1.50	30	400	0.35	1.00

Some of these dimensions are better defined than others, such as the radius of the central undamaged zone, zone 1, the onset of lateral outflow damage, and the maximum radius of zone 2. No attempt has been made to develop a normalization procedure to account for differences in the drop diameters or shapes.

3. MECHANICS OF WATER DROP IMPACTS

The experimentally observed damage was produced by both spherical and ellipsoidal shaped drops. The difference between the surface loading characteristics of ellipsoidal drops will be investigated for comparison with spherical drop impact conditions. In addition, the general features of the transient stress conditions within the ZnS specimens will be considered in relation to the impact conditions represented by the experimental program in order to interpret and correlate the experimental results. The need for further refinements in the analytical approach is pointed out and an initial effort to broaden the scope of the stress wave analysis is undertaken in Section V.

a. Ellipsoidal Drop Collisions

The analysis of ellipsoidal drop impacts on rigid surfaces has been formulated by Adler and James (1979). This analysis will be extended here, since it is relevant to the assessment of the water drop impact damage observed in the ZnS specimens.

The geometry associated with a perfectly compressible ellipsoid colliding with a rigid plane is indicated in Figure 11. The equation for the elliptical section is

$$\frac{r^2 \sin^2 \alpha}{b_1^2} + \frac{r^2 \cos^2 \alpha}{b_2^2} = 1 \quad . \tag{3.2}$$

34
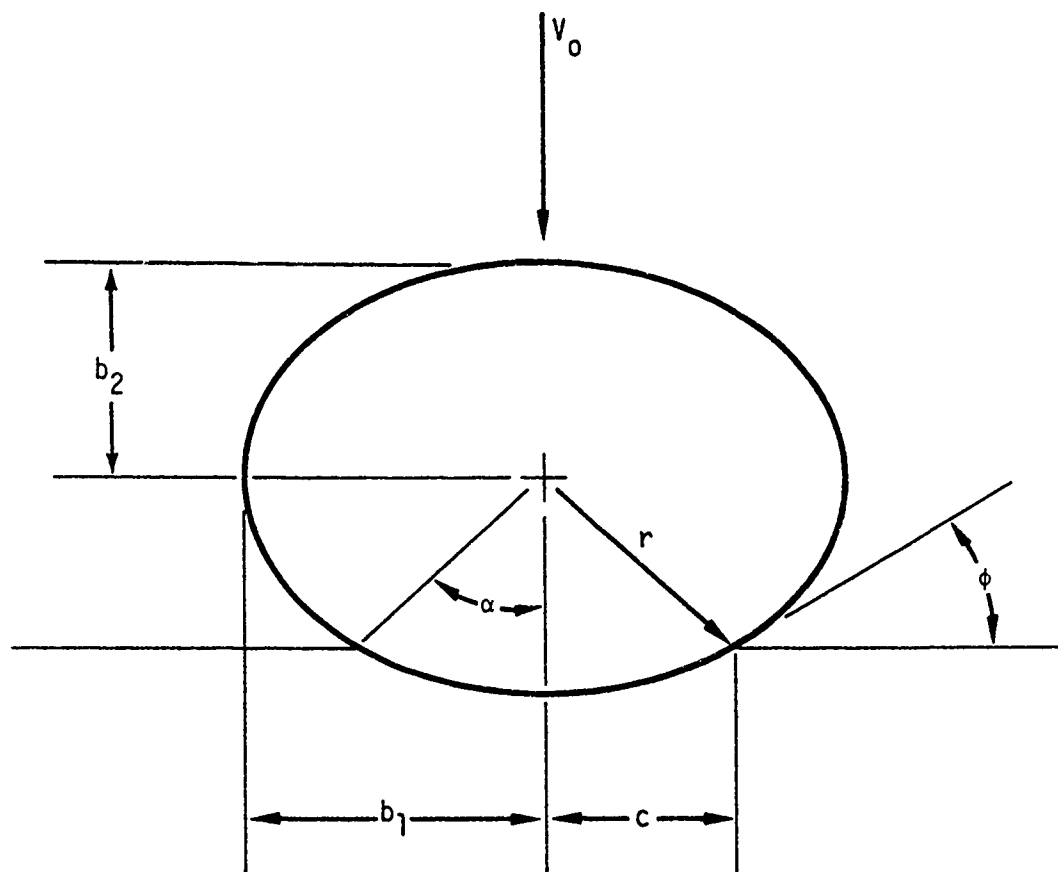
Figure 11.   Ellipsoidal Drop Geometry.

In terms of the relevant impact parameters,

$$\frac{c^2}{b_1^2} + \frac{(b_2 - v_o t)^2}{b_2^2} = 1 \tag{3.3}$$

and

$$\tan \alpha = \left(\frac{b_1}{b_2}\right)^2 \tan \phi \tag{3.4}$$

where   c is the radius of the circular contact area

v_o is the impact velocity

t is the time elapsed from initial contact

ϕ is the contact angle between the surface of the ellipsoid and the rigid plane.

The time-dependent radius of the contact area is found from Eq.(3.3),

$$c(t) = \left(\frac{b_1}{b_2}\right) \sqrt{2 b_2 v_o t - (v_o t)^2} \qquad . \tag{3.5}$$

Differentiating Eq.(3.5) yields the rate of expansion of the contact radius,

$$\dot{c}(t) = \left(\frac{b_1}{b_2}\right) \frac{v_o(b_2 - v_o t)}{\left[2 b_2 v_o t - (v_o t)^2\right]^{1/2}} = \left(\frac{b_1}{b_2}\right)^2 \frac{v_o(b_2 - v_o t)}{c} \quad . \tag{3.6}$$

According to Figure 10, Eq.(3.6) can also be written

$$\dot{c}(t) = \left(\frac{b_1}{b_2}\right)^2 \frac{v_o}{\tan \alpha(t)} \qquad . \tag{3.7}$$

Using Eq.(3.4), Eq.(3.7) becomes

$$\dot{c}(t) = \frac{v_o}{\tan \phi(t)} \qquad . \tag{3.8}$$

36

The expression in Eq.(3.8) is identical to that for a spherical body. This observation implies that the velocity of the boundary of the expanding contact area will be the same for these two cases when the contact angles are equal. The corresponding contact radii at which this occurs can be evaluated. Using the equation for an elliptical section in Eq.(3.2), it is easy to show

$$c = r\sin\alpha = \frac{b_1 \left(\frac{b_1}{b_2}\right) \sin\phi}{\left[1 + \left(\left(\frac{b_1}{b_2}\right)^2 - 1\right) \sin^2\phi\right]^{1/2}} \quad . \tag{3.9}$$

Denoting the radius of the contact zone for a spherical drop collision by a, then

$$a = r_0 \sin\phi \tag{3.10}$$

where r_0 is the radius of the spherical drop.

As stated in Section III.2.a an ellipsoidal drop will be considered equivalent to a spherical drop when they have the same mass. The equivalent drop radius is determined from Eq.(3.1). The major and minor semi-axes of the equivalent ellipse can be determined by reorganizing the parameters in Eq.(3.1) such that

$$b_2 = \frac{r_0}{\sqrt[3]{\left(b_1/b_2\right)^2}} \tag{3.11}$$

When the radius and distortion of the spherical drop are prescribed, b_2 and b_1 can be evaluated. As an example, consider when $r_0 = 1$ mm and $b_1/b_2 = 1.5$, then $b_2 = 0.765$ mm and $b_1 = 1.5 b_2 = 1.145$ mm. The

dimensions of the equivalent ellipsoid can be found in general from the graphical representation of the relations for the equivalent ellipsoid provided in Figure 12. The cross sectional shapes of ellipsoids covering the general range of possible interest are also shown in Figure 12, so some idea of the extent of the drop deformation can be realized.

The previous analysis assumes the drop is perfectly compressible which is a reasonable assumption for the initial stages of the impact event. However incompressibility effects will become significant in conjunction with the onset of lateral outflow (Adler, 1979a), and it would seem that differences in the nature of the lateral outflow velocities would occur between a spherical and ellipsoidal drop impact. It is our conjecture that whatever differences may arise would be relatively small. Furthermore, it is Adler's finding (Adler, 1979a) that an adequate criterion for the onset of lateral outflow for a spherical drop does not exist, although a number of analyses can be found in the literature. A fairly wide dicotomy prevails between the elementary analyses, numerical calculations, and experimental measurements for disc-shaped drops. To date, there are no direct measurements of the critical lateral outflow parameters for spherical drop impacts. In view of this situation the widely accepted lateral outflow condition stipulated by Bowden and Field (1964) is generally employed. Their criterion is simply

$$\sin\phi_c = \frac{v_o}{C_w} \tag{3.12}$$

where C_w is the compressional wave speed for water which is approximately 1.5 mm/μs. For the range of impact velocities under investigation the wave speed C_w should be replaced in Eq.(3.12) by the shock wave speed for water, U_w. According to Heymann (1968),

$$U_w = C_w (1 + 2M_o) \tag{3.13}$$
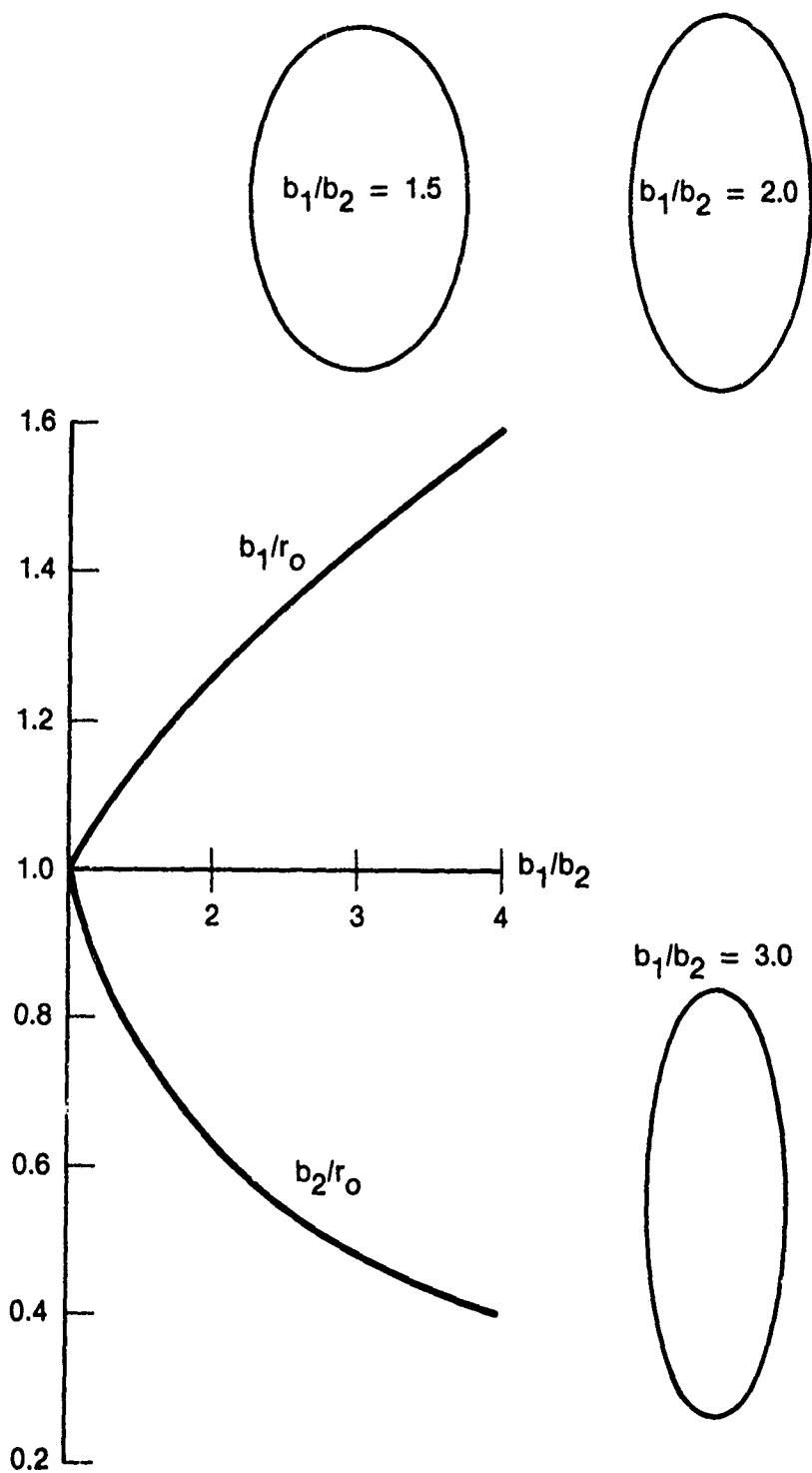
Figure 12. Ellipsoidal Drop Dimensions as a Function of the Oblateness Ratio.

where $M_o = v_o/C_w$. The relation in Eq.(3.13) is valid for impacts on a rigid surface when $M_o < 1.2$. Eq.(3.12) now takes the form

$$\sin\phi_c = \frac{a_c}{r_o} = \frac{M_o}{1 + 2M_o} \quad . \tag{3.14}$$

This is a lateral outflow criterion for spherical drops, however the same condition pertains to elliptical drops, since this is a condition on velocity components at the periphery of the contact zone, namely

$$\dot{c}_c^2 + v_o^2 = U_w^2 \tag{3.15}$$

It was already shown that the expansion velocities of the contact zone were identical for a sphere and an ellipsoid for the same value of the contact angle ϕ (Eq.(3.8)). The critical contact radii for which this condition pertains are determined from Eq.(3.9) and (3.10) upon substitution of Eq.(3.14), then

$$\frac{c_c}{b_1} = \frac{\left(\frac{b_1}{b_2}\right)\left(\frac{M_o}{1+2M_o}\right)}{\left[1 + \left(\left(\frac{b_1}{b_2}\right)^2 - 1\right)\left(\frac{M_o}{1+2M_o}\right)^2\right]^{1/2}} \tag{3.16}$$

Alternatively the condition that

$$\dot{c}_c = U_w \tag{3.17}$$

has also been used as a criterion for estimating the onset of lateral outflow. However the relation $\dot{a}_c = C_w$ was conjectured to be related to the location of the peak pressures in the pressure distribution found from numerical studies of water drop collisions on rigid surfaces (Rosenblatt, et al., 1979). The occurrence of the peak pressures at the critical radii computed from Eq.(3.17) appears to conform to the experimental

results obtained for spherical water drop impacts on polymethylmethacrylate specimens (Adler, 1979b). The critical contact radii for ellipsoidal water drops are found from

$$\frac{c_c}{b_1} = \frac{\left(\dfrac{b_1}{b_2}\right)\left(\dfrac{M_o}{1+2M_o}\right)}{\left[1 + \left(\dfrac{b_1}{b_2}\right)^2 \left(\dfrac{M_o}{1+2M_o}\right)^2\right]^{1/2}} \qquad (3.18)$$

The numerical evaluation of this expression is quite close to the value obtained from Eq.(3.16): the values from Eq.(3.16) being slightly higher. The critical radii are plotted in Figure 13 as a function of the impact velocity v_o.

The influence of water drop distortions prior to impact on the dimensions of the contact zone between the drop and the target (which is assumed to be directly related to the central undamaged zone) can now be evaluated explicitly. Consider a 2 mm spherical water drop impinging at 500 ms^{-1}. The radius of the contact zone is 0.2 mm as determined from Eq.(3.18). However, based on the plots in Figures 12 and 13, if the initially spherical water drop deforms into an ellipsoid prior to colli- sion with the target, the critical contact radius increases to 0.328 mm (b_1/b_2=1.5), 0.466 mm (b_1/b_2 = 2.0), and 0.734 mm (b_1/b_2 = 3.0). It is seen that the size of the contact zone can be increased significantly for even relatively minor drop distortions assuming the stated criteria for lateral outflow and the location of the peak pressure are applicable in general.

The time after impact for which the critical contact radii are reached corresponding to Eq.(3.16) and (3.18) can also be specified. The critical time t_c corresponding to Eq.(3.16) is

41

$$C_c/b_1 = \frac{(b_1/b_2)(M_o/1 + 2M_o)}{[1 + (b_1/b_2)^2(M_o/1 + 2M_o)^2]^{1/2}}$$
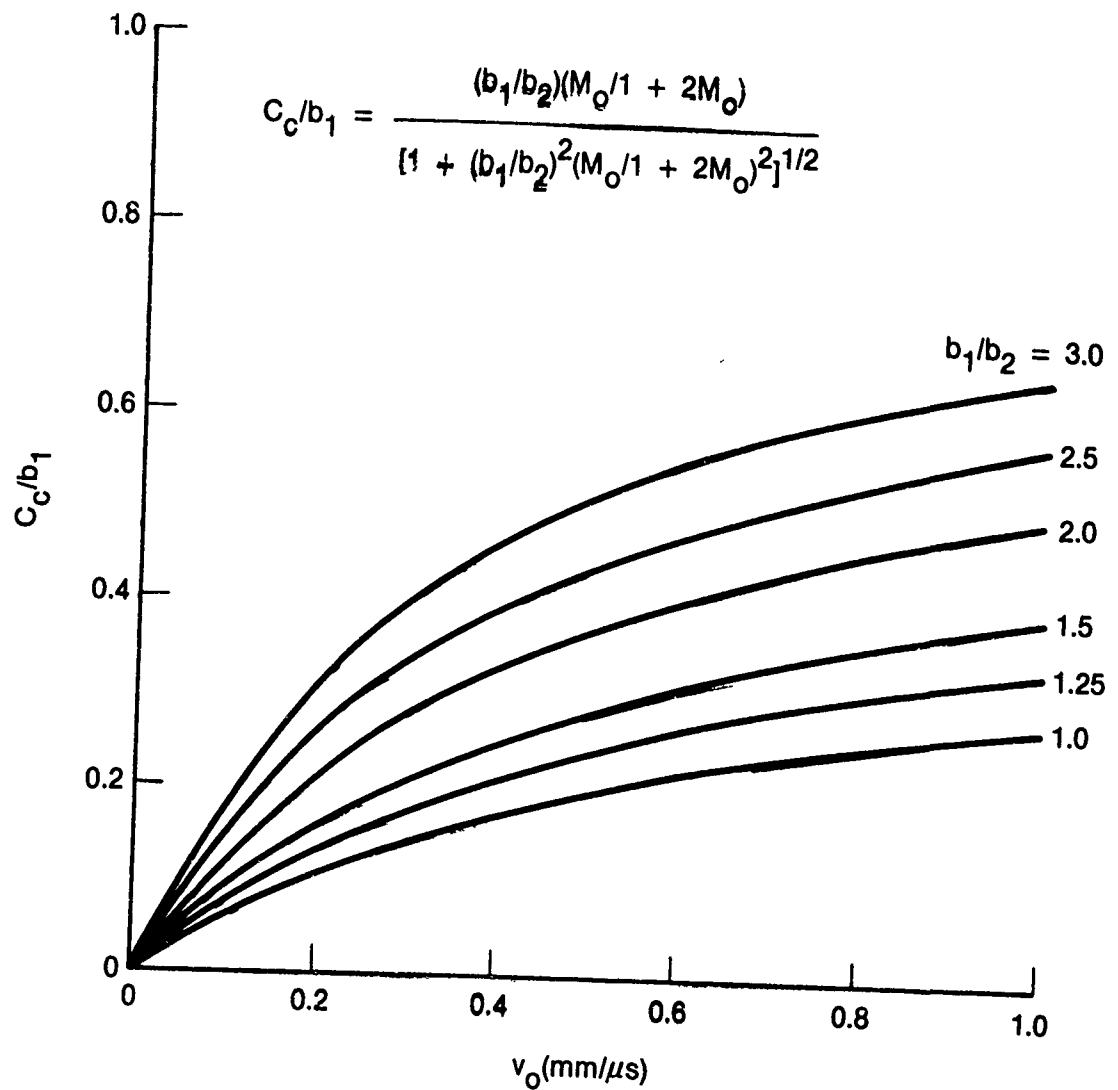
Figure 13. Contact Radii for Spherical and Ellipsoidal Drops at which the Peak Pressure is Assumed to be Reached as a Function of the Impact Velocity.

42

$$\frac{t_c v_o}{b_2} = 1 - \left[\frac{1 - \left(\frac{M_o}{1+2M_o}\right)^2}{1 + \left(\left(\frac{b_1}{b_2}\right)^2 - 1\right)\left(\frac{M_o}{1+2M_o}\right)^2} \right]^{1/2}, \qquad (3.19)$$

and the critical time corresponding to Eq.(3.18) is

$$\frac{t_c v_o}{b_2} = 1 - \left[1 + \left(\frac{b_1}{b_2}\right)^2 \left(\frac{M_o}{1+2M_o}\right)^2 \right]^{-1/2} \qquad (3.20)$$

The duration of the loading time is also greater for ellipsoidal drops compared with spherical drops.

The aforementioned effects should have relatively little influence on the pressure distribution applied to the surface of the target, since lateral outflow for the ellipsoidal drops considered will occur before the shock wave in the liquid reaches the back surface of the drop. In contrast, note the different conditions which would prevail for a pancake-shaped drop. On the basis of the previous analysis the major difference is that the direct pressure would be applied over a larger contact zone for a longer duration for the ellipsoidal drop as compared with a spherical drop of the same mass, but the magnitude of the applied pressure should be roughly the same in both cases. The pressure distribution on the interface would have to be determined from a detailed analysis of the flow conditions at the expanding interface as already carried out by Huang (1971), Hwang (1975), and Rosenblatt, et al. (1979).

The estimates for the dimensions of the contact zone are derived for a rigid surface, however the difference for water impacts on a zinc sulfide surface is not too significant: the difference in the shock wave velocity for the two cases is less than 6%. The magnitude of the uniform pressures which develop over the contact zone according to a one-dimensional wave analysis were determined and are shown in Figure 14 as a function of the impact velocity.
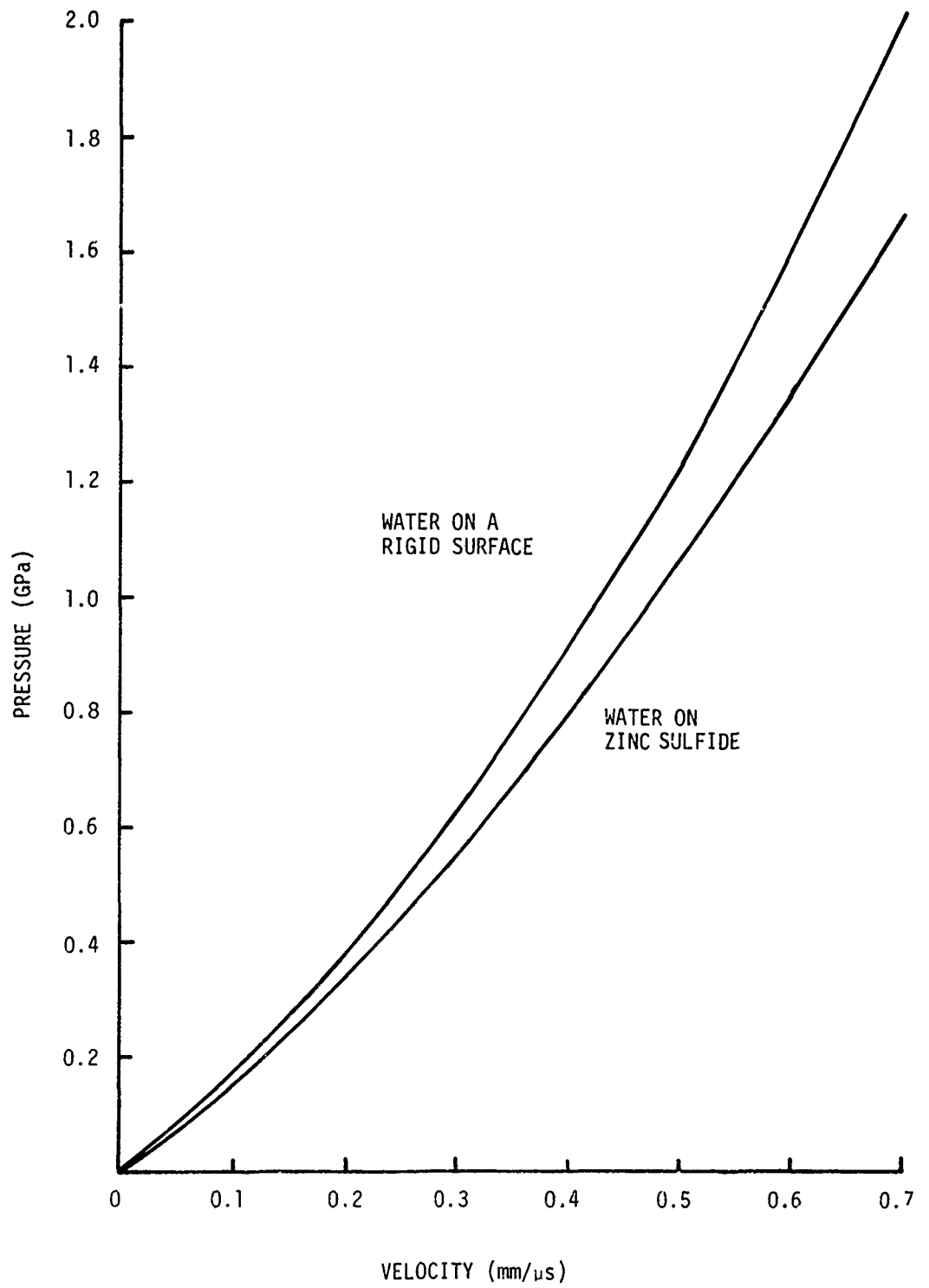
Figure 14.   Magnitude of Pressure at Water/Target Interface
as a Function of the Impact Velocity.

44

Aerodynamic effects should have a perturbing influence on water drop geometry prior to impact in all water drop impact facilities employing a specimen moving at high subsonic to supersonic velocities. If severe perturbations are not produced (small eccentricities), it is extremely difficult to identify the ellipsoidal drop collisions from post-test examinations of the impact specimens. Therefore, the photographic records of the actual collision in the ETI Liquid Drop Impact Facility are very useful because they afford the opportunity to quantify and correct these subtleties in the water drop impact conditions and the extent of the resulting damage which have gone unnoticed in most liquid drop erosion studies.

b.   Transient Conditions Within the Target Materials

The generation of stress waves due to water drop collisions on zinc sulfide specimens will be considered in order to better realize the manner by which the material fails and for the development of correlations with the loading cycle. Blowers' analysis (1969) has been employed by Adler (1977), Hackworth and Kocher (1977, 1978), and Hackworth, et al. (1979) to describe the state of stress in an elastic half-space due to a water drop collision. Rosenblatt, et al. (1977, 1979) have employed finite difference procedures to address this problem. Representative results from the analytical approach have been described (Adler, 1977, 1979a) and only a few observations will be made which will be used to show the relation between the fracture patterns for the zinc sulfide specimens and the form of the stresses imposed. A new and more general analytical approach for the determination of the transient stress states due to an arbitrary, local pressure distribution has been formulated in Section V. The analysis of the water drop/surface crack interactions is derived in Section VI.

The characteristic fracture pattern for water drop impacts on ZnS over a velocity range from 222 to 684 ms^{-1} is shown in Figure 6. The fractures are arrayed along circumferential paths around a central undamaged zone, zone 1 defined in Section III.2.b. The fracture concentration

decreases with radial distance. The subsurface character of the fractures (depth and general trajectory) also varies with radial distance as shown on a central cross section in Figure 9. The characteristic fractures are formed at or near the surface; all of the damage produced over the specified velocity range lies within an annulus around the central undamaged zone and extends to relatively shallow depths within the specimen. The analyses which follows will accordingly focus on the conditions at and near the surface of the specimen during the water drop loading cycle.

When a spherical water drop strikes the surface the boundary of the contact zone will expand in accordance with Eq.(3.5) when $b_1 = b_2 = r_o$. The initial velocities of the boundary of the contact zone, Eq.(3.6), are quite high, but decrease essentially as $t^{-1/2}$. As described by Blowers (1969) a condition is reached whereby the dilatational wave for the target material moves ahead of the contact zone followed by the shear wave at a later time. The time and radial distance at which these separations occur can be found by equating the velocity of the contact zone, $\dot{a}(t)$, in turn to the dilatational wave speed for zinc sulfide, $C_1 = 4.96$ mm/μs, and to the shear wave speed, $C_2 = 2.60$ mm/μs. The derivation is analogous to that carried out for a similar condition in Eq.(3.17). The final results are plotted in Figure 14, which clearly shows the relation between the propagation of stress waves and the hypothesized attainment of the peak pressure and the ensuing precipitous pressure release phase of the collision process. It is interesting to note that for impacts above 550 ms^{-1} this analysis indicates that the shear wave will move ahead of the contact zone boundary after the peak pressure has been reached. Also due to the increasing shock wave velocity in water as the impact velocity increases, the time required for the attainment of the peak pressure remains fairly constant over an extended range of impact velocities.

The relations provided in Figure 15 provide some perspective on the size of the loaded region during the pressure buildup phase and the time duration required for the indicated sequence of events to occur. The temporal development of the radial stresses for a 2 mm water drop impacting a ZnS target at 200 ms^{-1} is provided in Figure 16. The stresses are computed at a depth of 5 μm below the surface from Blowers' solution to the water

46
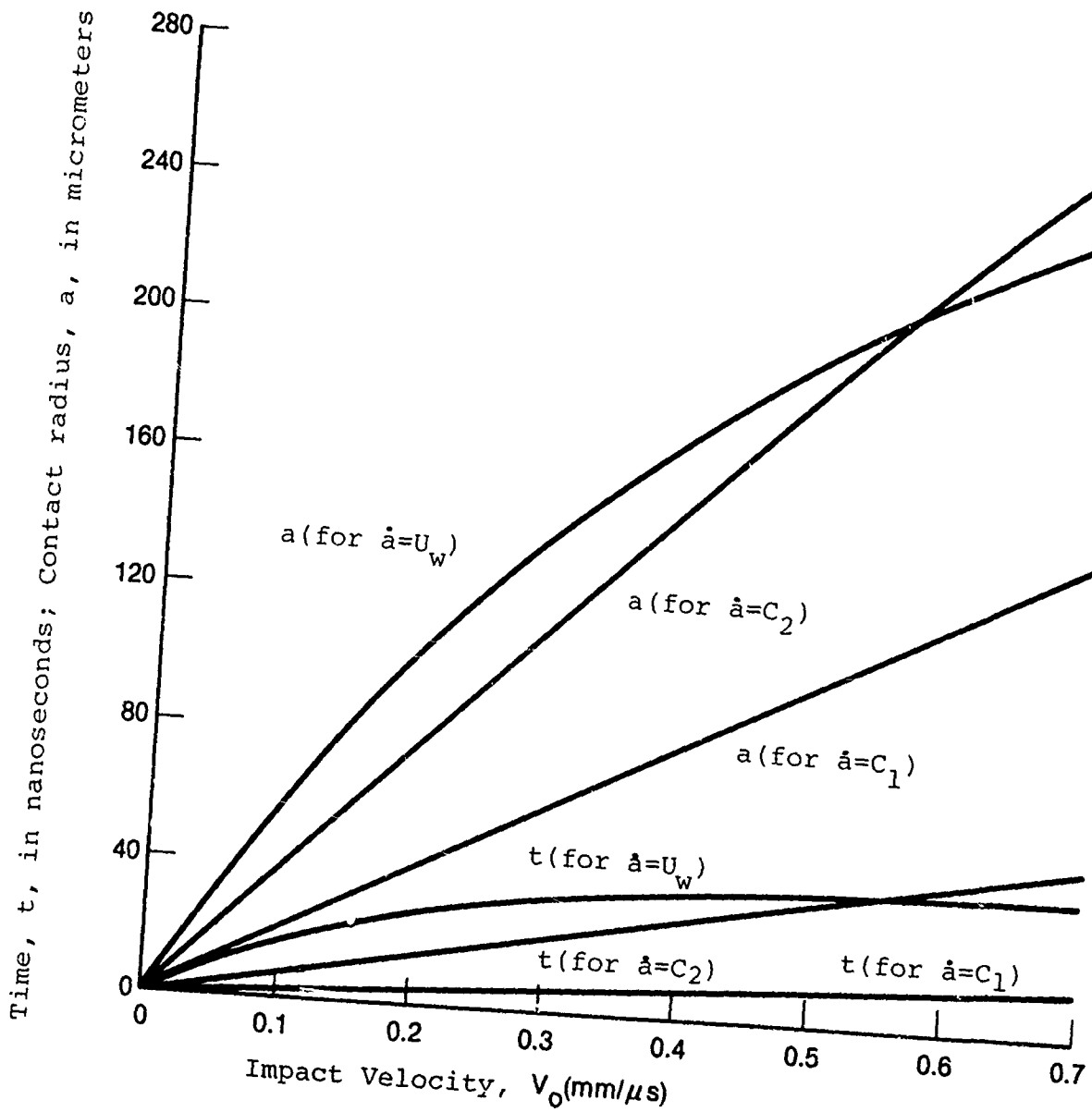
Figure 15.   Contact Radii and Times of Occurrence of Stress
Wave Separation from Contact Zone and Achievement
of Peak Interfacial Pressure for a 2 mm Water Drop.

47
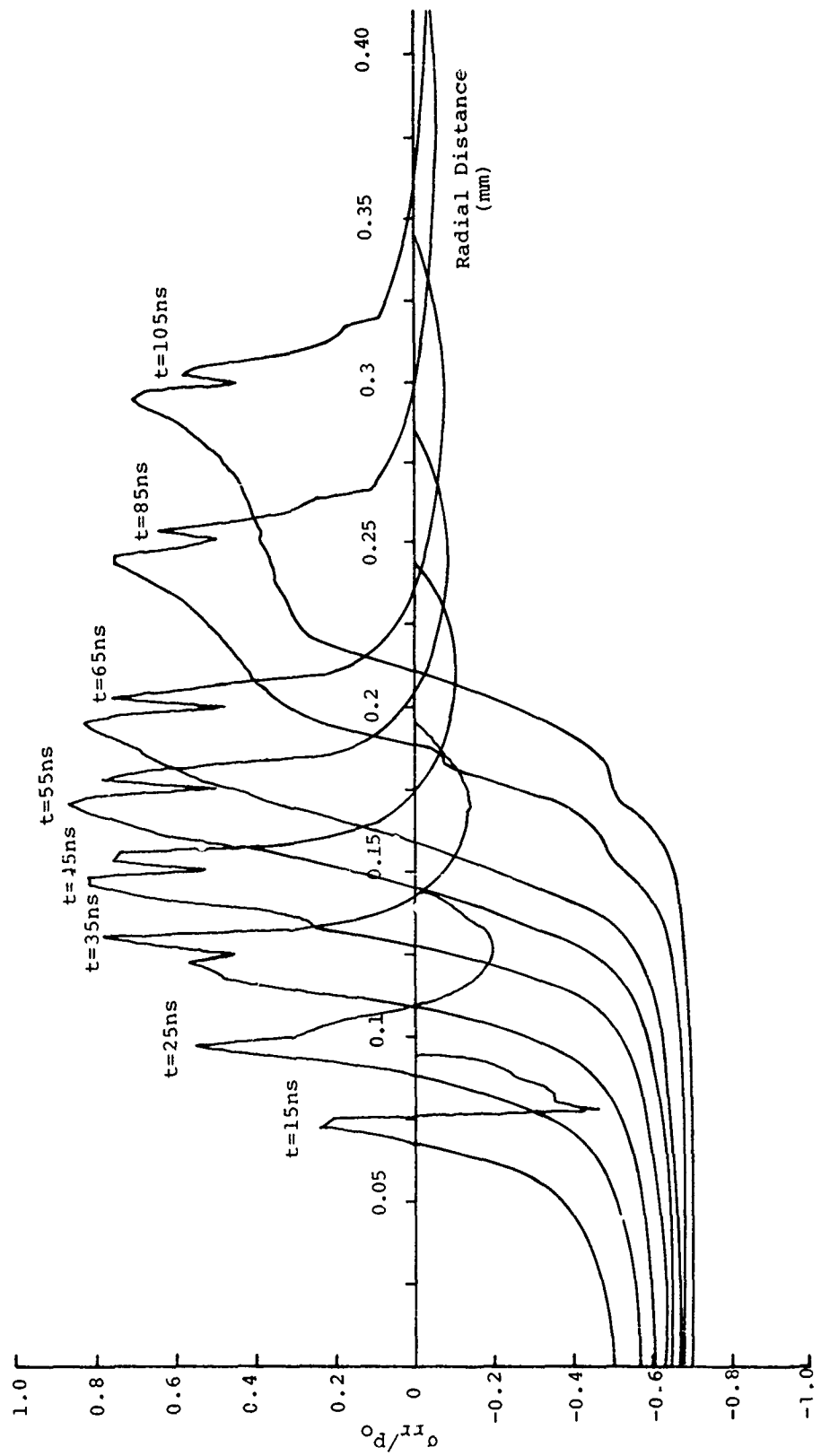
Figure 16. Temporal Development of the Normalized Radial Stress Component for a 2 mm Water Drop Impacting a Zinc Sulfide Target at 200 ms^{-1}.

drop impact problem which is for a uniformly loaded circular region whose boundary is expanding as the square root of the time after impact. Neglecting the variation in the pressure distribution during the loading phase the computed stress levels up to 35 ns should be reasonable. The subsequent decline in pressure predicted from Figure 15 to occur at 27 ns is not reflected in these calculations. The succeeding time increments are provided to show the evolution of the radial stress for this special case and to illustrate the general character of the radial stress as it propagates through fracture zones 2 and 3. The valley between the two peaks in the tensile stress distribution seen when the contact time exceeds 35 ns corresponds to the location of the Rayleigh surface wave: the shear wave is propagating just slightly ahead of the Rayleigh wave. The maximum extent of the radial stress values corresponds to the location of the dilatational wave front. The magnitude of the stress is normalized with respect to the magnitude of the impact pressure. For a water drop impact on zinc sulfide, Figure 14 indicates the magnitude of the impact pressure is 340 MPa. For example the magnitude of the peak radial tensile stress when $t = 45$ ns is 279 MPa.

A significant state of triaxial tensile stress develops in conjunction with the Rayleigh wave. At a depth of 5 μm and when $t = 45$ ns, $\sigma_{rr}=179$ MPa, $\sigma_{\theta\theta}=89$ MPa, and $\sigma_{zz}=169$ MPa. The spatial extent of this stress condition is on the order of a few micrometers and is quite localized in the vicinity of the surface of the target.

Referring to Figure 16, it is seen that significant radial tensile stresses are present at a radial distance of 0.1 mm when $t = 25$ ns . The potential exists for the initiation of circumferential fractures. According to the plot in Figure 15, the peak pressure on the surface will be achieved when $a_c = 0.105$ mm. At this time the distortional wave would have advanced beyond the contact zone, but the occurrence of this condition is dependent on the magnitude of the stress wave velocities in the target material.

Similar plots can be given for the higher impact velocities. The magnitude of the impact pressure would be increased as shown in Figure 14, so the magnitude of the stresses would be correspondingly increased; however the general evolution of the radial stress component follows a pattern analogous to that in Figure 16. The temporal evolution of the radial stress component for a 2 mm drop impacting at 600 ms^{-1} is shown in Figure 17. The larger radial distance compared with the collision at 200 ms^{-1} prior to the development of significant tensile stresses is apparent. This effect would be reflected in the larger dimension of the central undamaged zone as the impact velocity is increased. When $t = 45$ ns, the plot in Figure 17 indicates the peak radial tensile stress is 0.75 p_o. Referring to Figure 14 for the value of p_o, the magnitude of the radial stress is about 1 GPa. This stress level is more than sufficient to initiate fracture. The time $t = 45$ ns corresponds to the peak pressure loading as seen from Figure 15 when $v_o = 600$ ms^{-1}. The continued increase in the radial stress components after $t = 45$ ns due to the continuous loading condition inherent in Blowers' analysis has to be viewed with caution. However for times greater than 45 ns the characteristic form of the radial stress component is indicated after the Rayleigh wave has separated from the contact zone.

The rapid change in the nature of the radial stress with depth into the target is shown in Figure 18 when $v_o = 600$ ms^{-1} and $t = 65$ ns. The need for an accurate analysis of the transient stresses at shallow depths below the surface of the target is amply demonstrated for establishing the fracture response of the target material.

The development of significant radial tensile stresses should correspond to the initiation of fractures at the periphery of the central undamaged zone (zone 1). This condition appears to occur in the vicinity of the location of the peak pressure on the surface of the target. However this criterion cannot be taken as a general relationship, since the radial location of the peak pressure is determined solely from the shock wave relations for water and the stress state in the target is dependent on the
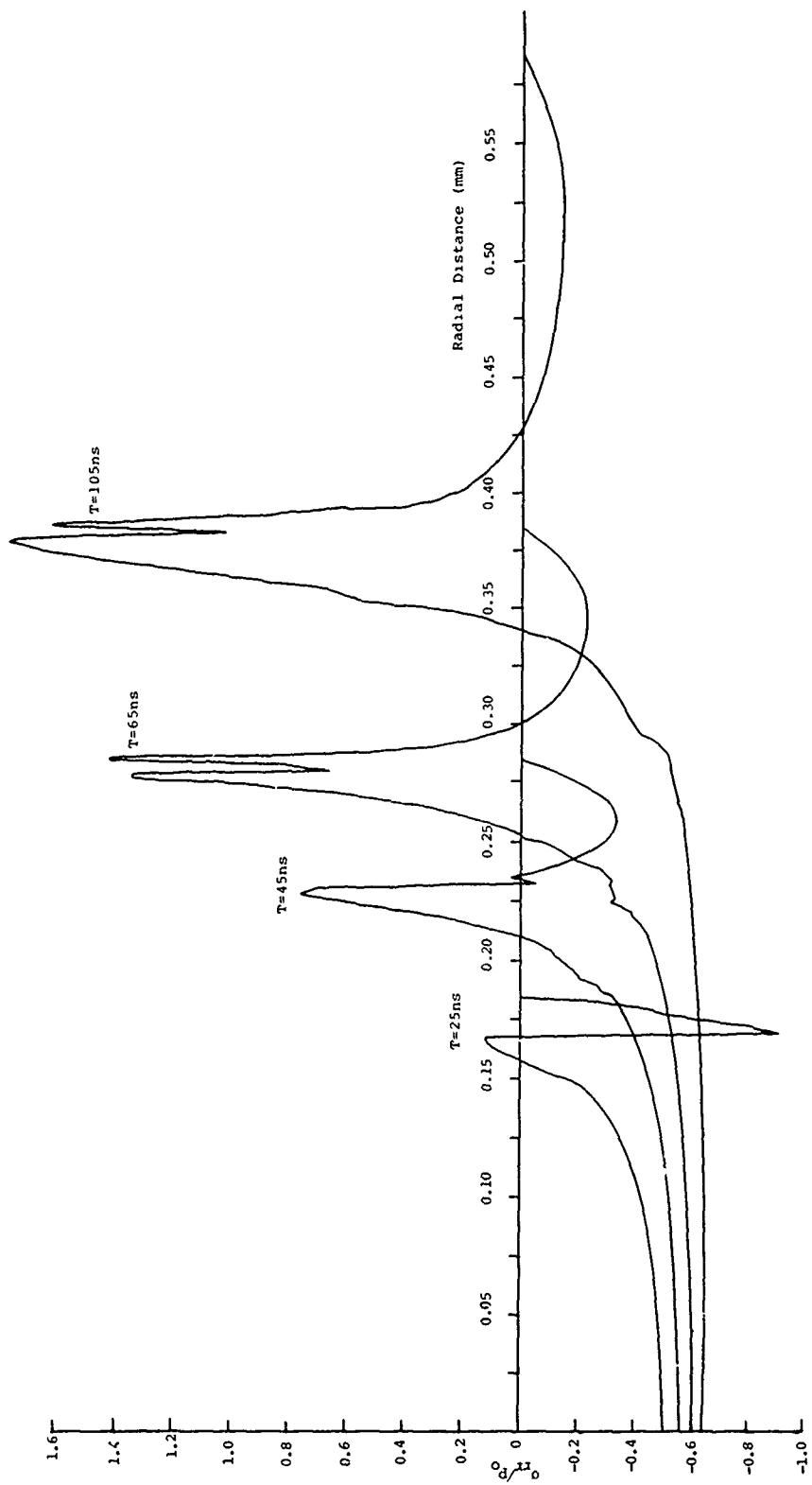
Figure 17. Temporal Development of the Normalized Radial Stress Component for a 2 mm Water Drop Impacting a Zinc Sulfide Target at 600 ms^{-1}.

51
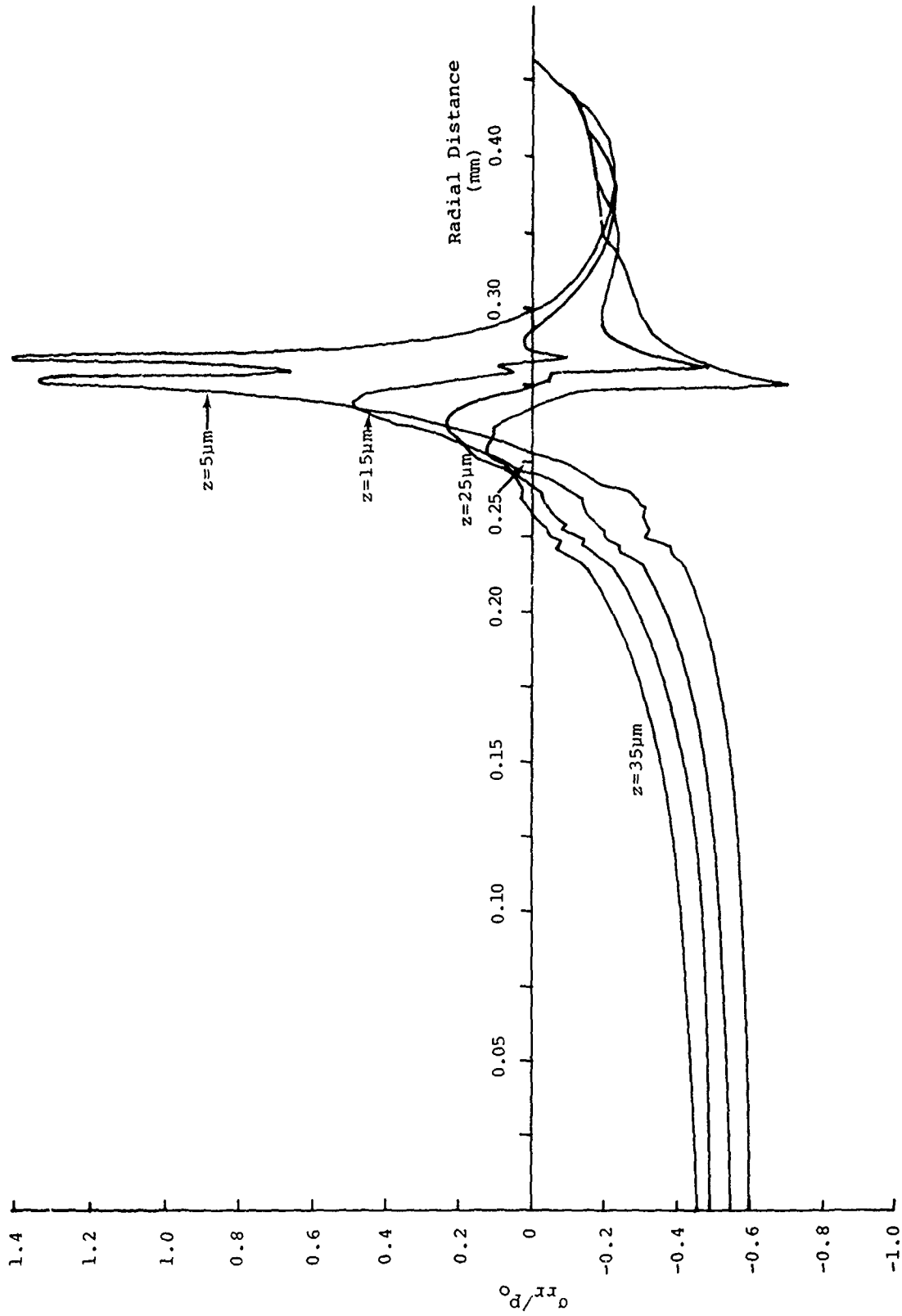
Figure 18. Variation of Normalized Radial Stress Component with Depth into a Zinc Sulfide Target for a 2 mm Water Drop Impacting at 600 ms^{-1} when t=65 ns.

stress wave velocities inherent in the target material. With this proviso the relationship between the location of the peak pressure and the onset of fracture (boundary of zone 1) will be evaluated from the available data. The relevant data from Tables 5 and 7 is consolidated in Table 8 along with the calculated values of the critical contact radii determined from Figure 15. The comparison between the measured values of the outer boundary of fracture zone 1 and the calculated values of the location of the peak pressure indicates a fairly close correspondence within the level of cumulative experimental error in the measurements required. The variation in the measured dimensions is due to the circumferential nonuniformity in the initiation of fracture and the differences which arise depending on whether or not the specimens have been etched. This measure of the fracture response is independent of the zinc sulfide formulation investigated as demonstrated by the comparison in Table 8.

TABLE 8. Comparison of the Calculated and Measured Values
of the Critical Radii for Spherical Drop Impacts
on Zinc Sulfide.

Shot No.	Material	Impact Velocity (ms^{-1})	Drop Radius (mm)	a_c/r_o	a_c (calculated) (mm)	a_c (measured) (mm)
1036	B	299	0.85	0.141	0.120	0.115
1016	A(B-2)	331	.85	.151	.128	.11-.125
1012	A(G-2)	336	.81	.153	.124	.125-.130
1017	C	338	.78	.153	.119	.105-.110
1040	FLIR	401	1.01	.172	.174	.180
1041	FLIR	497	1.05	.196	.206	.192
1051	A(G-2)	505	1.05	.198	.208	.200
978	C	512	0.84	.199	.167	.15-.16
1052	A(G-2)	514	1.07	.200	.214	.200
1048	FLIR	516	1.05	.200	.210	.200-.220
1038	B	517	0.86	.200	.172	.160-.165
1049	A(G-2)	518	1.05	.200	.210	.200
1042	FLIR	594	1.05	.216	.227	.215-.225
1050	FLIR	600	1.05	.217	.230	.230

SECTION IV

POST-TEST EXAMINATION OF ZINC SULFIDE SPECIMENS

The general features of the grain structure in CVD zinc sulfide have been described in Section II.1. The influence of the grain size, grain orientation, grain growth patterns, inclusions, surface imperfections, and hardness on the nature of the damage produced by water drop collisions has been considered here. Overviews of water drop impact damage on CVD zinc sulfide have been given previously, but it does not appear that a systematic analysis of the above-mentioned characteristics has been pursued (Adler and Hooker, 1976, 1978; Graves, et al., 1977; Hackworth and Kocher, 1977; Hackworth, et al., 1979; Peterson, 1975, 1979). Detailed microscopic examination of both the impact face and cross section of impacts on the three materials described in Section II.1 over the velocity range from 237 to 640 ms^{-1} have been carried out to examine the most damaging aspects of the inherent microstructure in CVD ZnS.

Variations in surface finish have the greatest effect upon the resultant extent and type of fractures observed for a given velocity-drop size condition. The strong effect of surface scratches upon the fracture pattern, especially the fractures in zone 3 (the fracture zones were defined in Section III.2.b can be readily seen in Figure 7b. Zone 3 now contains in addition to fractures decreasing in depth with radius some large and deep fractures nucleated at surface scratches.

The influence of the surface grain structures and orientation was investigated using scanning electron microscopy (SEM) and transmission electron microscopy (TEM) of surface replicas. The results of the SEM investigation will be discussed first. SEM micrographs of shot no. 838 are provided in Figures 19 and 20. The impact face of shot no. 838 is oriented to coincide with the growth direction; i.e., along the major axis of the columnar grains as can be seen in the figures.

The circumferential fractures on the impact face display significant interaction with the surface grains in fracture zone 2. Figure 19 shows two views of the fractures in zone 2 of the etched impact face of shot no. 838 for the major axes of the grains oriented tangent and perpendicular
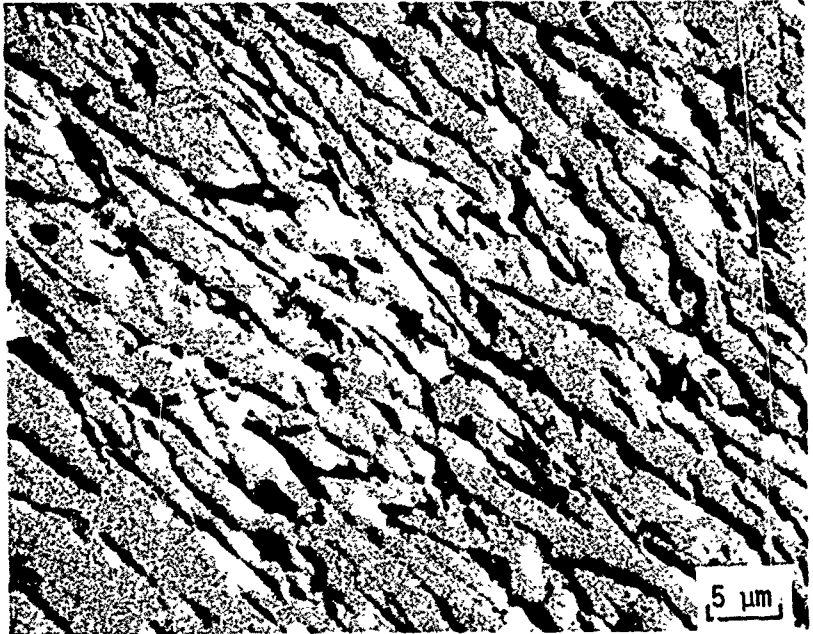
a. Major Axes of Grains Tangent to
Circumferential Fractures.
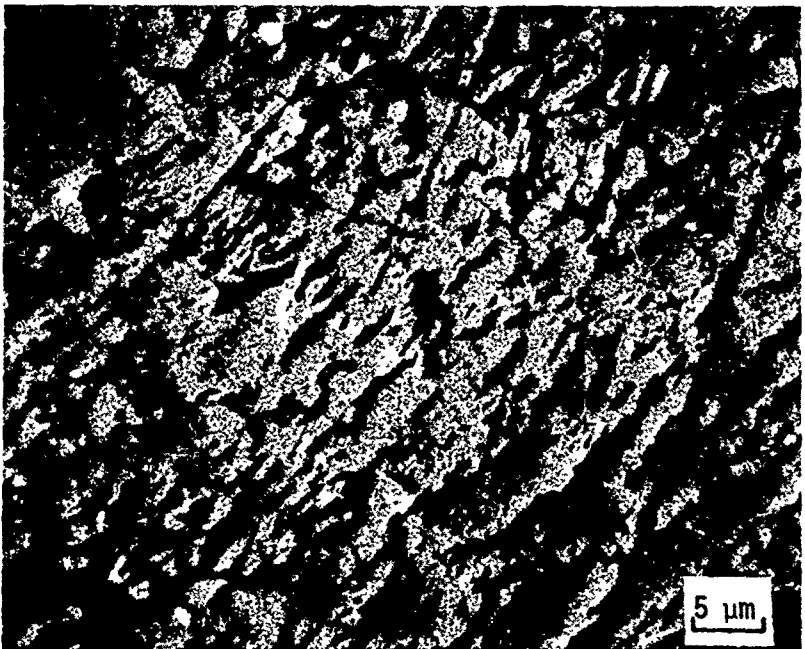
b. Major Axes of Grains Perpendicular
to Circumferential Fractures.

Figure 19.   SEM Micrograph of Impact Face (etched) of Zone 2
for Shot No. 838.
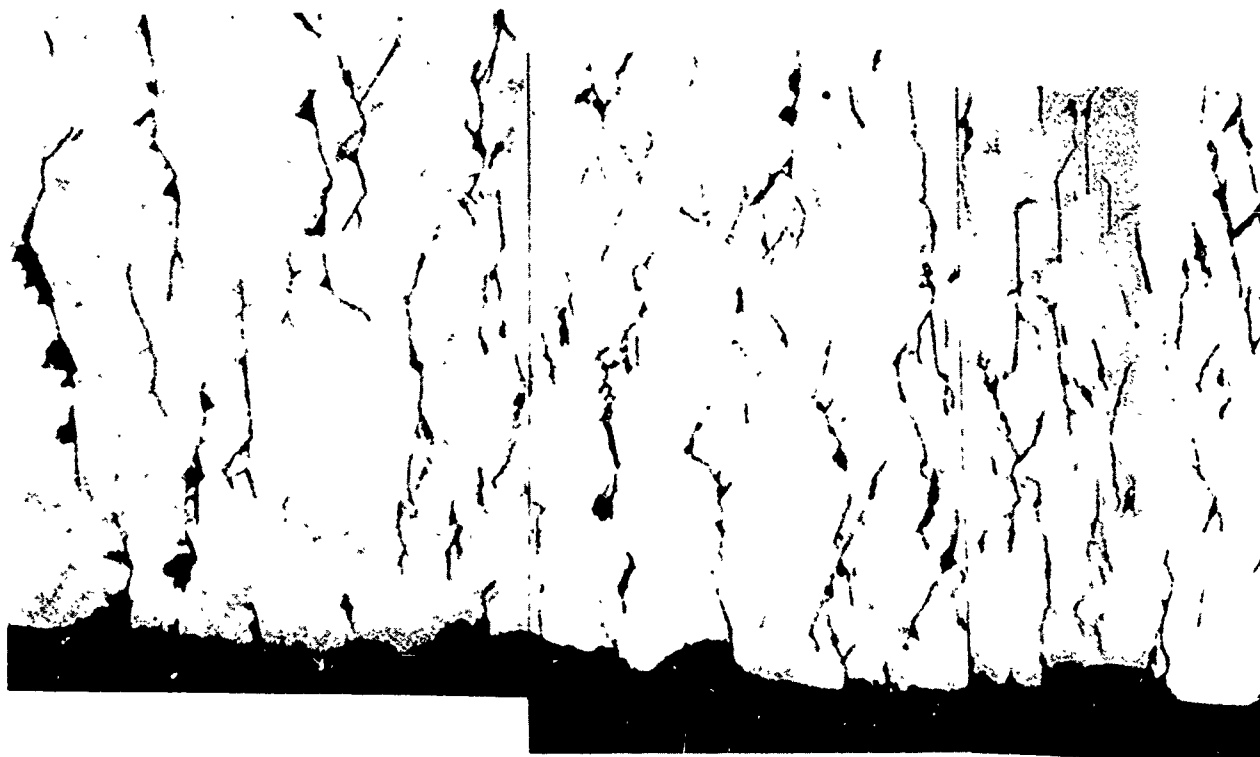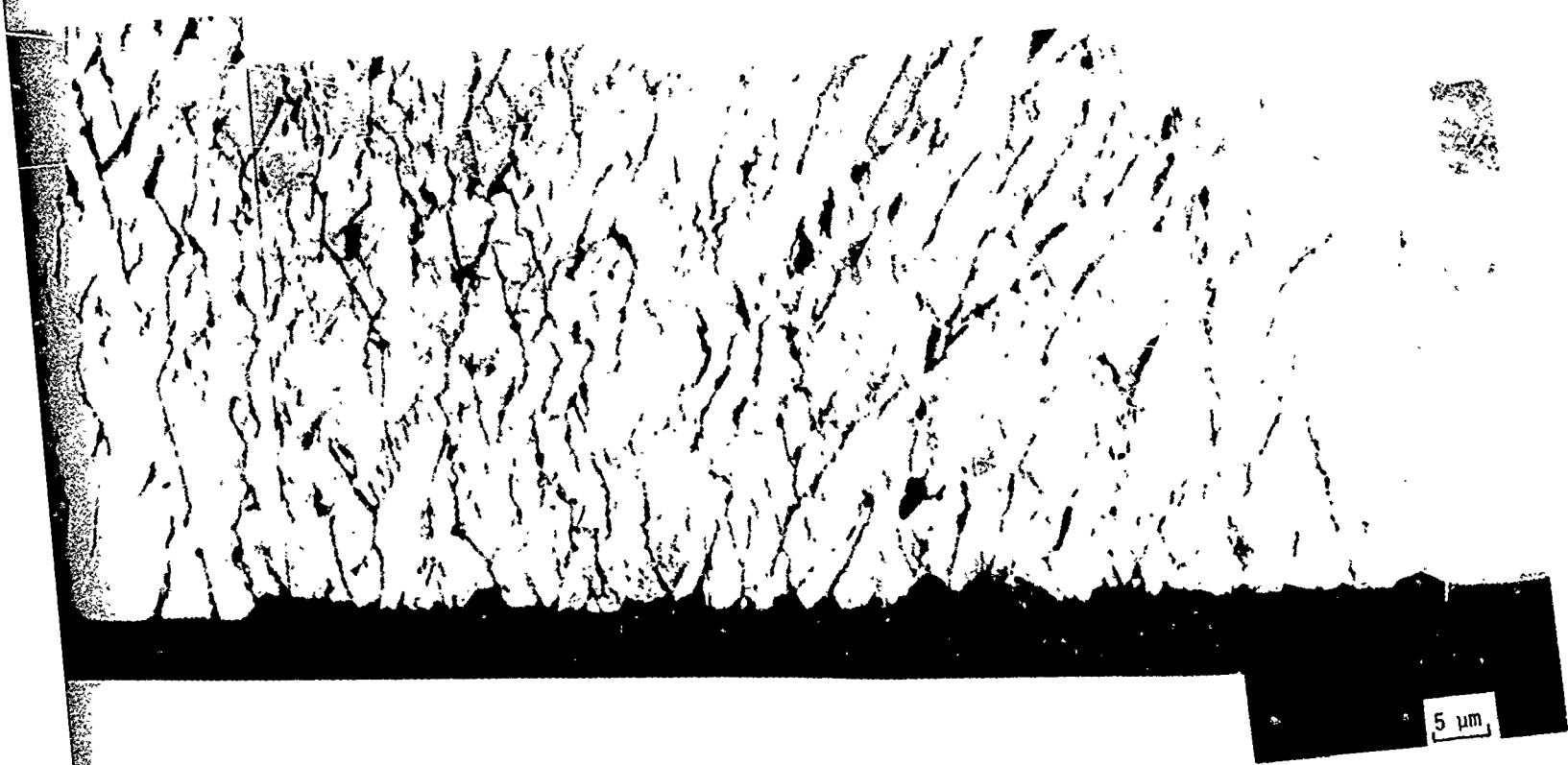
Figure 20. SEM Micrograph of Impact Face of Shot No. 838 from Central Un-damaged Zone (Zone 1) to Initiation of Lateral Outflow.

5 μm

to the stress wave front. The stress wave/grain orientation interaction controls the character of the circumferential fractures. For the conditions represented in Figure 19, major axes of the grains tangent to the stress wave propagation direction, the fractures are almost entirely intergranular. When the grain major axes are perpendicular to the stress wave propagation direction, Figure 19b, the circumferential fractures tend to be shorter than in Figure 19a, less continuous, and there is relatively little tendency for the fractures to follow grain boundaries.

Figure 20 shows the radial variation in the circumferential fracture concentration in a region originating at the boundary of the central undamaged zone (right hand side of figure) to the region at which lateral outflow damage is initiating (left hand side of figure). The composite micrograph is along the stress wave propagation direction which is from right to left. The major axes of the grains are oriented at approximately 50° to the stress wave propagation directions. A higher concentration of short circumferential fractures is evident at the periphery of the undamaged zone than at larger radial distances. The circumferential fracture lengths tend to increase with radial distance. The onset of lateral outflow damage would indicate that the loading phase of the water drop collision has terminated.

Two preferential crack orientations can be distinguished in the high crack concentration annulus (zone 2). One system of fractures represents intergranular fractures oriented predominantly along the grain boundaries parallel to the major axes of the grains. These fractures are accordingly directed at angles from roughly 40 to 60° to the wave propagation direction extending from lower left to upper right in Figure 20. The second system of fractures is due to a distribution of fine polishing scratches and are oriented at an angle in the vicinity of 75° to the wave propagation direction extending from the lower right to upper left in Figure 20. The orientations of the major axes of the grains and the wave propagation direction represent an intermediate condition to those shown in Figure 19a and b.

As the radial distance from the point of impact increases the concentration and orientation of the circumferential fractures change. The orientation of the circumferential fractures becomes normal to the wave propagation direction thereby essentially ignoring the grain structure. The fracture mode is now transgranular with little preference for grain boundaries, unless the grain orientation is highly favorable. This mode of fracture prevails in the intermediate fracture zone as the concentration of circumferential fractures drastically decreases and the fracture lengths increase significantly. The occasional cracks observed far from the point of impact (at the outer boundaries of zone 3) generally are associated with some form of microstructural defect. Some form of stress concentration is necessary to nucleate and propagate a crack at the low stress levels which would prevail in this region.

The surface of shot no. 838 contained some polishing scratches which interacted with the fracture pattern on a very small scale, although the gross fracture behavior did not show interactions with the polishing flaws. In contrast shot no. 1012 which was polished by a commercial polisher to above average optical window tolerances showed no scratch interaction with the fracture pattern on either a micro or macroscopic scale. Shot no. 1012 was on a surface parallel to the growth plane (i.e., the columnar grains were perpendicular to the impact plane) at an impact velocity of 336 ms^{-1}. The impact surface was examined by TEM microscopy of a shadowed carbon replica. Figure 21 is a region within zone 2 adjacent to the central un-damaged zone which appears in the lower left of the figure. The fractures tend to be of two types: those that are small ($<1\mu$) and wholly contained within the grains and those which are somewhat longer ($\sim3\mu m$) and are associated with grain boundaries. This behavior is very similar to that of Figure 19b without the perturbing influence of the surface scratches. Figure 22 shows the fractures at the inner radius of zone 3 (i.e., adjacent to zone 2) in which the fractures are transgranular with no influence from the grain structure or orientation.

The critical stress states due to a water drop impact on an elastic half-space have been described in Section III.3.b. For brittle materials the magnitude and duration of the radial stress component when it is tensile at

60

Figure 21.   TEM Micrograph of a Surface Replica of Impact Face
of Shot No. 1012 in the Region of the Inner Radius
of Zone 2. Note the Very Short Circumferential
Extent of the Fractures.

Figure 22.   TEM Micrograph of a Surface Replica of the Impact
              Face of Shot No. 1012 in the Inner Region of Zone 3.
              Note the Transgranular Character of the Fractures.

and near the specimen's surface are the dominant contributions to fracture initiation and propagation. The magnitude and duration of these tensile stresses are related to the size of the drop and its velocity at impact. Once the tensile stresses develop in advance of the expanding water drop/ target interface, they are of a magnitude which more than exceeds the critical stress intensity factor of the zinc sulfide target. The surface cracks surrounding the central undamaged zone consisting of the major portions of fracture zones 2 and 3 show relatively little interaction with the surface grain structure and near surface inclusions. Figure 19a shows that in this region the grain boundaries provide paths for the crack trajectories when the major axes of the grains are approximately normal to the stress wave propagation direction. As the stress waves propagate away from the impact site, they are attenuated due to the inherent attenuation of the material as well as due to the energy lost in creating and extending cracks. Thus fractures at the more distant points in zone 3 will tend to show the greatest dependence on the material's microstructural features. The interactions between the fractures found in this region and those features which are able to provide sites for stress amplification of the low amplitude stress waves of moderately long duration propagating through zone 3 were examined in moderate detail. Interactions did occur with some of haystack structures described in Section II.1, however this contribution to the general degradation of the specimen is essentially inconsequential.

The fracture interaction with the haystack grain formations may be a result of the presence of the same inclusion that nucleated the haystack or could be a result of the grain orientation interface. Wimmer and Graves (1977) note that the columnar grain structure results in some anisotropy in strength, hardness, and Poisson's ratio. Their strength and elastic property tests were on a macroscopic scale, so it is conceivable that the effects of local anisotropy could be much greater than their mechanical property evaluations indicate. The local anisotropy of the CVD zinc sulfide could in itself produce critical stress conditions for fracture initiation.

The major crack; for specimens with a moderate distribution of fine polishing scratches are relatively large semi-elliptical fractures nucleated at surface scratches as can be seen in Figure 7b. These fracture surfaces exhibit a large orientational dependence between the stress wave direction and the surface scratch. Surface scratch nucleated cracks are typically bounded in extent by the points at which the included angle reaches 45° between the line of the scratch and the tangent to an expanding circle centered at the impact site intersecting the scratch. Even if the scratch is composed of a series of small disjointed segments oriented differently than the composite scratch direction, the resultant fractures will only interact with these segments very weakly, if at all, until they satisfy the included angle requirement described above. The scratch nucleated fractures tend to be more pronounced in fracture zone 3 than in fracture zone 2. This may be due to the longer duration but decreased amplitude of the stress pulse. The decreased stress amplitude is compensated by the ease of fracture nucleation at a fine surface scratch.

In addition to the influence of grain boundaries and surface polishing scratches on impact fracture behavior, the influence of grain size, inclusion content, and hardness were also investigated.

Three different formulations of ZnS (materials A, B, and C) as described in Section II.1, whose properties are tabulated in Tables 1 to 3, provided variations in grain size and hardness. Material C has both a lower microhardness and a larger grain size than both material A of B which are similar in grain size and hardness. Comparison of the impact damage due to single drop impacts on these materials reveals no significant difference in the extent or nature of the fractures produced. Cross sectional views of the fracture patterns are shown in Figures 6 and 23 for impact velocities of 517, 515, and 512 ms^{-1} on materials B, A, and C, respectively. It is apparent from these figures that the variations in hardness, grain size, grain shape, and inclusion content represented by these three materials does not significantly affect the impact damage. Comparisons of the measurements of the fracture zone boundaries and fracture depth dimensions tabulated in Tables 6 and 7 corroborate this conclusion.

Figure 23. Cross Sectional Views of Water Drop Impacts for Comparison of Two Formulations of CVD Zinc Sulfide. Upper Figure: Material A, Shot No. 971 at 515 ms^{-1}. Lower Figure: Material C, Shot No. 978 at 512 ms^{-1}.

In order to extend the range of available grain structures, specimens were also cut from material A parallel to the deposition direction to yield specimens in which the exposed face has the elongated grain structure illustrated in Figure 1a. Comparable water drop impact conditions (shot no. 813 and 838), representing the difference in grain structure shown in Figure 1, produced no obvious difference in the fracture pattern observable on both a microscopic and macroscopic scale.

SECTION V

ANALYSIS OF WATER DROP IMPACTS ON ELASTIC SOLIDS

Knowledge of the stress states in a target material due to a water drop collision is an essential prerequisite for analyzing the extent of the resulting crack growth which occurs when the impact velocity exceeds the fracture threshold. In general, the motion of the drop and the material is a coupled problem and should be treated as such, since the contact pressure is a function of the deceleration of the drop which depends in turn on the deformation of the surface. This leads to a complex non-linear interdependence between the pressure and the surface deformation. We will side-step this issue, however, by assuming that for the purpose of calculating the pressure, the material surface can be assumed to be rigid. This will result in an c erestimation of the pressure which for materials with the hardness of zinc sulfide is not too significant. This can be corrected if desired by using an iterative procedure once the general solution for the surface deformation has been obtained.

The analytic approach developed here is based on the use of Green's functions and a Green's theorem relation derived from the divergence theorem. For these techniques to be useful, it is necessary that the problem be linear which imposes some restrictions on the drop speed and material properties. In particular, deformations must be sufficiently small that a linear stress-strain relation is valid. This eliminates from consideration, for example, those events which result in substantial cratering. The linearity assumption is bound to fail at crack tips however, since a strictly linear material would never crack and consequently, some special treatment of these regions is required. From the ETI experimental work on ZnS, it appears that in the velocity range of interest, namely 222 to 684 ms^{-1}, the response of the material is reasonably linear except for the creation of the cracks. This is deduced from the fact that any permanent deformations of the surface as a result of the impact are negligible compared to the dimensions of the impact zone. For simplification, the material will also be assumed isotropic. This assumption is supported by experiments on ZnS conducted by ETI which do not show any strong dependence of impact damage on grain orientation for the typical grain dimensions in the current production of CVD ZnS windows.

67

1. PREVIOUS WORK

A few comments concerning some previous work on this problem will be made. Rosenblatt, et al. (1976,1977), have developed a numerical solution to the crack growth problem in ZnSe using explicit numerical methods. In comparing their results with the experimental results obtained in this program for ZnS, it is seen that the numerical solution produces cracks whose spacial extent essentially encompasses the annulus corresponding to zone 2 cracks (ETI notation) observed in the cross sections in Section IV. The cracks in the numerical solution are not as clearly defined as in the experiments: they tend to appear more in the form of a completely cracked zone than as a distribution of distinct cracks. Also, the experimentally observed zone 3 cracks appear to be almost completely absent in the numerical solution. Since ZnS has a greater strength than ZnSe, this discrepancy is not likely to be explained by the difference in the materials. A more likely explanation is that the crack model used by Rosenblatt and co-workers is incomplete, since according to their fracture criterion only tensile cracks are allowed. Cracks can occur in any cell in the finite difference grid once the tensile stress criterion is satisfied. This is not an appropriate representation for the preferential crack formations controlled by the imposed transient stresses and a surface flaw distribution. Considerable improvements in the basic fracture model appear to be required before the finite difference computations can begin to reproduce the physics of the actual impact induced fracture patterns. This points to an area of concern which requires further study and points out the danger of relying too heavily on numerical results alone.

A second point examined by Rosenblatt, et al. (1977) was the pressure-surface deformation interdependence. It was found that assuming a rigid surface for the purposes of calculating the pressure does not introduce intolerable errors over the velocity range of interest.

The analytic approach used by Hackworth and Kocher (1978) will also be mentioned, since their analysis was to provide the local stress conditions at various locations within the half-space for the purpose of estimating the crack growth which would occur. However detailed examination of their work revealed an apparent error in their contribution to an extension of the initial analysis of the stress wave problem (Blowers, 1969; Adler, 1977). Their starting point is the TURBAN computer program which evaluates the stresses in an elastic half-space due to a pressure distribution given by $P(r,t) = P_o \theta(k\sqrt{t}-r)$ where $\theta(x)$ is the Heaviside function

$$\theta(x) = \begin{cases} 1 & x>0 \\ 0 & x<0 \end{cases} \tag{5.1}$$

The analytic solution was determined by Blowers (1969) for this pressure distribution in terms of several integrals which are evaluated by TURBAN. Hackworth and Kocher's extension of Blowers' idealization of the water drop impact problem to time-dependent pressure loadings is based on Duhamel's superposition relations which utilized Blowers solution, σ_o. They proposed that $\sigma(r,z;t)$, the solution for the general time-dependent distribution $P(r,t)$, is given in terms of the solution, $\sigma_o(r,z;t)$, for the restricted distribution $P_o(r)$ by the expression

$$\sigma(r,z;t) = \sigma_o(r,z;t) + \int_0^t \sigma_o(r,z,t-\tau) \frac{\dot{P}(\tau)}{P(o)} \, d\tau \tag{5.2}$$

where the final pressure distribution is given by

$$P(r,t) = P_o(r) \, P(t) \, . \tag{5.3a}$$

$$\dot{P}(\tau) \equiv \frac{dP}{dt} \bigg|_{t=\tau} \tag{5.3b}$$

This is correct as far as it goes, but Eq.(5.2) is valid only for the limited class of distributions f.. which the restricted distribution is independent of time, a point which is not clearly made in the report. This however excludes Blowers' solution upon which TURBAN is based. A more general relation similar to Eq.(5.2) can easily be found, however, which is valid for Blowers' distribution although the final pressure distribution does not have the simple product form sought by Hackworth and Kocher. The general solution as will be shown later (see Eq.(5.50)) for the physical stress matrix at location $(\vec{y},t)$ in a half-space due to a prescribed pressure distribution on the surface is given by

$$\sigma_{ij}(\vec{y},t) = \oint_S da_x \int_0^t d\tau \ P(\vec{x},t-\tau) \ \Sigma_{3ij}(\vec{x},\vec{y};\tau) \qquad (5.4)$$

where $\oint_S da_x$ denotes the integral over the surface S, specified by $x_3=0$, of the half-space. On this surface the coordinate vector is $\vec{x}$, the pressure distribution is $P(\vec{x},t)$ and the appropriate Green's tensor is $\Sigma_{3ij}(\vec{x},\vec{y};\tau)$. Taking the Laplace transform of this expression, we find

$$\bar{\sigma}_{ij}(\vec{y},s) = \oint_S da_x \bar{P}(\vec{x},s) \ \bar{\Sigma}_{3ij}(\vec{x},\vec{y};s) \qquad (5.5)$$

Since the problem is axisymmetric, Eq.(5.5) can be written in cylindrical coordinates. Thus (dropping the tensor indices and incorporating numerical constants into the definition of $\bar{P}(r',s)$)

$$\bar{\sigma}(r,z;s) = \int_0^\infty dr' \ \bar{P}(r',s) \ \bar{\Sigma}(r',r,z;s) \qquad (5.6)$$

In order to reproduce the result given by Hackworth and Kocher (1978), we will first assume a pressure distribution which is independent of time. Later, we will extend these results for a general pressure distribution.

Suppose we know the solution for a constant pressure $P_o(r)$. Then

$$\bar{P}_o(r,s) = \int_0^\infty e^{-st} P_o(r)dt = \frac{P_o(r)}{s} \tag{5.7}$$

and

$$\bar{\sigma}(r,z,s) - \bar{\sigma}_o(r,z,s) = \int_0^\infty dr' \ \bar{\Sigma}(r',r,z;s) \left[\frac{s\bar{P}(r',s) - P_o(r')}{s} \right] \tag{5.8}$$

Since

$$\bar{\dot{P}}(r,s) \equiv \overline{\frac{dP}{dt}} = \int_0^\infty e^{-st} \frac{dP}{dt}dt = s\bar{P}(r,s) - P(r,o) \tag{5.9}$$

and provided that $P_o(r) = P(r,o)$

$$\bar{\sigma}(r,z,s) - \bar{\sigma}_o(r,z,s) = \int_0^\infty dr' \ \bar{\Sigma}(r',r,z;s) \frac{\bar{\dot{P}}(r',s)}{s}$$

$$= \int_0^\infty dr' \bar{\Sigma}(r',r,z;s) \frac{P_o(r')}{s} \frac{\bar{\dot{P}}(r',s)}{P_o(r')} \tag{5.10}$$

The Laplace transform of Eq.(5.2) gives

$$\bar{\sigma}(r,z,s) - \bar{\sigma}_o(r,z,s) = \bar{\sigma}_o(r,z,s) \frac{\bar{\dot{P}}(s)}{P(o)} \tag{5.11}$$

Comparing the expressions in Eq.(5.10) and (5.11), it is seen that Eq. (5.2) can only be valid for those pressure distributions for which

$$\frac{\bar{\dot{P}}(r',s)}{P_o(r')} \text{ is independent of } r'.$$

71

This requires

$$\dot{\bar{P}}(r,s) = P_0(r)\bar{H}(s) .$$ (5.12)

where $\bar{H}(s)$ is an arbitrary function of s .

In view of Eq.(5.9), we find

$$\bar{P}(r,s) = P_0(r) \left(\frac{1+\bar{H}(s)}{s} \right)$$ (5.13)

and it follows that

$$P(r,t) = P_0(r) \ F(t)$$ (5.14)

where

$$F(t) = 1 + \int_0^t H(\tau)d\tau .$$ (5.15)

Thus, Eq.(5.2) is only valid for restricted pressure distributions $P_0(r)$ which are functions only of r . This excludes, for example, Blowers' distribution since it depends on both r and t . It is natural to ask then whether a product form might in fact be more useful than Blowers' solution since then one would be able to include the time dependence of the pressure at any given point. This is not likely to be the case, however, since such a distribution does not model the expansion of the contact zone of the drop. Since the waves are expanding outward from the contact zone, the fact that the source is expanding is certainly as important as the fact that its magnitude changes with time at a fixed point.

These results are easily extended, however, to general distributions $P_o(r,t)$ which do include Blowers' distribution as a special case, although the resulting final pressure distributions are not simply the products of the restricted distributions and arbitrary functions of time.

If we know the stress state due to a pressure distribution $P_o(r,t)$, then

$$\bar{\sigma}(r,z;s) - \bar{\sigma}_o(r,z;s) = \int_0^\infty dr'\ \bar{\Sigma}(r',r,z;s)\left[\bar{P}(r',s) - \bar{P}_o(r',s)\right]$$

$$= \int_0^\infty dr'\ \bar{\Sigma}(r',r,z;s)\ \bar{P}_o(r',s)\ \times \left[\frac{\bar{P}(r',s)}{\bar{P}_o(r',s)} - 1\right] \qquad (5.16)$$

As before, the right hand side of this relation can be factored provided

$$\frac{\bar{P}(r',s)}{\bar{P}_o(r',s)} - 1 = \bar{H}(s) \qquad (5.17)$$

in which case

$$\bar{\sigma}(r,z;s) - \bar{\sigma}_o(r,z;s) = \bar{\sigma}_o(r,z;s)\ \bar{H}(s) \qquad (5.18)$$

or

$$\sigma(r,z;t) = \sigma_o(r,z;t) + \int_0^t d\tau\ \sigma_o(r,z;t-\tau)\ H(\tau) \qquad (5.19)$$

From Eq.(5.17)

$$\bar{P}(r,s) = \bar{P}_o(r,s)\left(1+\bar{H}(s)\right) \qquad (5.20)$$

which implies

$$P(r,t) = P_o(r,t) + \int_0^t P_o(r,t-\tau)\ H(\tau)\ d\tau\ . \qquad (5.21)$$

It is easy to show that this reduces to the previous result when $P_o(r,t)$ is independent of time. In the general case, $H(\tau)$ is not equal to the normalized time derivative of the pressure function nor is the final pressure a simple product of the restricted pressure, $P_o(r,t)$, and an arbitrary function of time. For example, using Blowers' distribution

$$P_o(r,t) = P_o \theta(k\sqrt{t}-r) \tag{5.22}$$

where P_o is a constant. We find after some manipulation,

$$P(r,t) = P_o(r,t) \left[1+I(r,t)\right] \tag{5.23}$$

where

$$I(r,t) = \theta(k\sqrt{t}-r) \int_o^{t-\frac{r^2}{k^2}} d\tau \, H(\tau) \ . \tag{5.24}$$

This does not have the simple product form sought by Hackworth and Kocher because of the radial dependence of $I(r,t)$. Using the fact that

$$\theta(k\sqrt{t}-r) = \theta\left(t-\frac{r^2}{k^2}\right) \tag{5.25}$$

we notice that Eq. (5.23) can be rewritten in the form

$$P(r,T) = P_o(r,T) \left[1+I(T)\right] \tag{5.26}$$

where

$$T \equiv t - \frac{r^2}{k^2} \tag{5.27}$$

$$P_o(r,T) = P_o \, \theta(T) \tag{5.28}$$

Thus it is apparent that within the confines of Eq.(5.21) generalizations of Blowers' problem can be generated through the use of Eq.(5.23). If our only interest was the stress state for the axisymmetric problem and this rather restricted class of pressure distributions, we would in fact use these results without introducing the additional complexity of the Green's tensor. The latter is central also, however, in developing a systematic treatment of wave diffraction from cracks and for treating asymmetric pressure distributions. An example of the latter is the distribution due to a drop impact at an angle of incidence other than 90°.

2. A FORMAL SOLUTION TO THE PROBLEM OF CALCULATING THE STRESS DISTRIBUTION IN AN ELASTIC HALF-SPACE DUE TO AN ARBITRARY PRESSURE DISTRIBUTION ON ITS SURFACE

The formal solution for the determination of the stresses in a half-space due to a localized pressure distribution on its surface is formulated in terms of a Green's theorem derived from the divergence theorem. The derivation of this relation will be outlined because a clear understanding of its origin will be necessary later. Consider two solutions to the wave equation in the half-space denoted by $(u_\ell, t_{k\ell})$ and $(u_\ell', t_{k\ell}')$ where u_ℓ and $t_{k\ell}$ denote the displacement vector and stress tensor, respectively. (The physical stress matrix $\sigma_{k\ell}$ is not a tensor because it does not transform as such for curvilinear coordinates. If needed, the relation between $t_{k\ell}$ and $\sigma_{k\ell}$ is easily found using the metric tensor for the coordinates involved. For cartesian coordinates, this tensor is unity.)

Form the quantity

$$w_k = t_{k\ell} * u_\ell' - t_{k\ell}' * u_\ell \qquad (5.29)$$

where * denotes the convolution defined by

$$a*b = \int_0^t d\tau \, a(t-\tau) \, b(\tau) \quad . \qquad (5.30)$$

The upper limit t denotes the limit $\underset{\epsilon \to 0}{\text{Lim}}\ t+\epsilon$ whenever it is necessary to avoid ambiguity in the definition of the integral. In particular,

$$\int_{0}^{t} \delta(t-\tau)\ b(\tau)\ d\tau \equiv b(t) \tag{5.31}$$

where $\delta(t)$ is the Dirac delta function. A repeated subscript such as in Eq.(5.29) indicates a summation over the range 1 to 3 unless otherwise indicated.

Taking the divergence of Eq.(5.29) and using the equations of motion,

$$t_{k\ell,k} + \rho f_\ell = \rho \ddot{u}_\ell \tag{5.32}$$

$$t'_{k\ell,k} + \rho f'_\ell = \rho \ddot{u}'_\ell \tag{5.33}$$

(The notation $a_{,k}$ denotes the partial derivative $\frac{\partial a}{\partial x_k}$.) we find,

$$w_{k,k} = t_{k\ell} * e'_{k\ell} - t'_{k\ell} * e_{k\ell} + \rho \ddot{u}_\ell * u'_\ell - \rho \ddot{u}'_\ell * u_\ell$$

$$- \rho f_\ell * u'_\ell + \rho f'_\ell * u_\ell \tag{5.34}$$

where the strain components $e_{k\ell}$ are defined by

$$e_{k\ell} \equiv 1/2(u_{\ell,k} + u_{k,\ell}) \ . \tag{5.35}$$

But

$$t_{k\ell} * e'_{k\ell} = E_{k\ell mn} e_{mn} * e'_{k\ell} = e_{k\ell} * E_{k\ell mn} e'_{mn} = e_{k\ell} * t'_{k\ell} = t'_{k\ell} * e_{k\ell} \tag{5.36}$$

where we have used the general stress-strain relation $t_{k\ell} = E_{k\ell mn} e_{mn}$ and the symmetry property $E_{k\ell mn} = E_{mnk\ell}$ for the elastic constants. Also, from the definition of the convolution, Eq.(5.30), it is easily seen that

$$\ddot{\vec{u}} * \vec{u}' = (\vec{u} * \vec{u}')^{\cdot\cdot} - \vec{v}(o) \cdot \vec{u}' - \vec{u}(o) \cdot \dot{\vec{u}}' \qquad (5.37)$$

where $\vec{v}(o) = \dot{\vec{u}}(o)$. A similar expression holds with the primed and unprimed variables reversed. Thus

$$w_{k,k} \equiv \vec{\nabla} \cdot \vec{w} = -\rho \vec{f} * \vec{u}' + \rho \vec{f}' * \vec{u} - \rho \vec{v}(o) \cdot \vec{u}' + \rho \vec{v}'(o) \cdot \vec{u}$$

$$- \rho \vec{u}(o) \cdot \dot{\vec{u}}' + \rho \vec{u}'(o) \cdot \dot{\vec{u}} \qquad (5.38)$$

The divergence theorem states that for any closed surface S surrounding a volume V ,

$$\int_V \vec{\nabla} \cdot \vec{w} \, dv = \oint_S \vec{w} \cdot \hat{n} \, da \qquad (5.39)$$

where $\hat{n}$ denotes the unit outward normal vector to the surface. Thus

$$\int da \, \vec{t}_{(n)} * \vec{u}' + \int dv \, \rho [\vec{f} * \vec{u}' + \vec{v}(o) \cdot \vec{u}' + \vec{u}(o) \cdot \dot{\vec{u}}']$$

$$= \int da \, \vec{t}'_{(n)} * \vec{u} + \int dv \, \rho [\vec{f}' * \vec{u} + \vec{v}'(o) \cdot \vec{u} + \vec{u}'(o) \cdot \dot{\vec{u}}] \qquad (5.40)$$

where

$$t_{(n)_k} = t_{k\ell} n_\ell = t_{\ell k} n_\ell \quad . \qquad (5.41)$$

In a later discussion it will be important that this relation is true for any closed surface in the material and not just for the actual physical surface of the material.

Now for u' , we chose the solution of the wave equation with the singular source term

$$\rho f_i' = \delta(t) \, \delta(\vec{x}-\vec{\xi}) \, \delta_{ij} \quad , \tag{5.42}$$

where δ_{ij} is the Kronecker delta, and the initial conditions

$$\vec{u}'(o) = \vec{v}'(o) = 0 \; , \tag{5.43}$$

We denote this solution by $G_{ij}(\vec{x},\vec{\xi};t)$ and require

$$G_{ij} = 0 \text{ for } t<0 \; . \tag{5.44}$$

The term involving f' is easily evaluated

$$\int_V dv_x \, \rho(f' \ast \vec{u})_j = \int_V dv_x \delta(\vec{x}-\vec{\xi}) \int_0^t d\tau\delta(t-\tau) \, u_i(\vec{x},\tau) \, \delta_{ij}$$

$$= \int_V dv_x \, \delta(\vec{x}-\vec{\xi}) \, u_j(\vec{x},t)$$

$$= \begin{cases} u_j(\vec{\xi},t) & \xi \, \varepsilon \, V \\ \\ 0 & \xi \, \varepsilon \, V_c \end{cases} \tag{5.45}$$

where V_c denotes the complement of V , i.e.. the region outside the boundary of V . We will define $u_i(\vec{\xi},t)$ on the surface as the limit as the surface is approached from the inside. Thus using Eq. (5.40) (dropping the vector notation for $\vec{x}$ and $\vec{\xi}$)

$$u_j(\xi,t) = \oint da_x \left[t_{(n)i}(x,t) * G_{ij}(x,\xi;t) - u_i(x,t) * T_{(n)ij}(x,\xi;t) \right]$$

$$+ \int_V dv_x \, \rho \left[f_i(x,t) * G_{ij}(x,\xi,t) + v_i(x,o) \, G_{ij}(x,\xi,t) \right.$$

$$\left. + u_i(x,o) \cdot \dot{G}_{ij}(x,\xi;t) \right] \qquad (5.46)$$

where the stress matrix $T_{(n)ij} \equiv T_{ijk} \, n_k$ is obtained from G_{ij} by using the stress-strain relation,

$$T_{ijk} = \lambda G_{\ell j,\ell} \, \delta_{ik} + \mu (G_{ij,k} + G_{kj,i}) \qquad (5.47)$$

The partial derivatives are with respect to the x coordinates.

Since both $t_{(n)i}$ and u_i cannot be independently specified on a closed surface, we must impose an additional constraint on the Green's function to eliminate the dependence on one or the other of these quantities. Since we wish to specify the pressure on the surface, the natural choice is to require

$$T_{(n)ij} = 0 \text{ on } S \qquad (5.48)$$

where S denotes the surface of the half-space. If we further assume the absence of sources and homogeneous initial conditions, then

$$u_j(\xi,t) = \oint_S da_x \, t_{(n)i}(x,t) * G_{ij}(x,\xi;t) \, . \qquad (5.49)$$

This is the fundamental solution to the half-space problem with a prescribed stress distribution on the surface. The stresses in the material are found by applying the stress-strain relation to both sides of Eq.(5.49). Thus

$$t_{k\ell}(\xi,t) = \oint_S da_x \, t_{(n)i}(x,t) * \Sigma_{ik\ell}(x,\xi;t) \qquad (5.50)$$

79

where $\Sigma_{ijk}(x,\xi;t)$ is determined by Eq.(5.47) with the exception that the partial derivatives are now with respect to the ξ coordinates.

These expressions, while providing a formal solution to the problem are, of course, of no practical value until an explicit expression for the Green's tensor is found.

3. DERIVATION OF THE GREEN'S TENSOR

The Green's tensor we require is the solution to the wave equation

$$\rho \left[c_t^2 \, G_{ij,\ell\ell} + (c_\ell^2 - c_t^2) \, G_{\ell j,\ell i} - \ddot{G}_{ij} \right] = - \rho f_{ij} \tag{5.51}$$

with the source term

$$\rho f_{ij} = \delta(t) \, \delta(\vec{x}-\vec{\xi}) \, \delta_{ij} \tag{5.52}$$

which has homogeneous initial values and satisfies the boundary condition on the surface of the half-space given by

$$T_{(n)ij} = 0 \; . \tag{5.53}$$

The surface stress tensor $T_{(n)ij}$ is given in terms of the Green's tensor by

$$T_{(n)ij} = \left[\lambda G_{\ell j,\ell} \delta_{ik} + \mu \, (G_{ij,k} + G_{kj,i}) \right] n_k \tag{5.54}$$

where λ and μ are the Lame coefficients which are related to the longitudinal and transverse wave speeds by

$$c_t^2 = \frac{\mu}{\rho}$$

$$c_\ell^2 = \frac{\lambda + 2\mu}{\rho} \tag{5.55}$$

Since the governing equations are linear, we can always express the Green's tensor as a sum, each term of which satisfies the wave equation but not the complete set of boundary conditions. By making a judicious choice in this separation, the problem of determining G_{ij} reduces to several simpler problems whose solutions when added determine G_{ij}. A familiar example from electrostatics is the problem of determining the electric field due to a point charge near an infinite conducting plane. The solution is most easily found by writing it as the sum of the fields due to the charge alone, which will not satisfy the boundary conditions at the plane, and that due to a virtual image charge located behind the plane with properties chosen so that the sum of the two fields does satisfy the boundary conditions on the plane. The first of these fields will be singular at the location of the charge, whereas that of the second will be everywhere regular since the image charge does not lie inside the physical region.

We will, in fact, use this analogy to write the Green's tensor as a sum of three fields with the first being the singular field due to the source Eq.(5.52) with no boundaries. The second term will be the field due to the image of Eq.(5.52) and the third that which is required to satisfy the boundary conditions on the plane. These latter two terms are regular everywhere inside the material. In view of Eq.(5.53), the boundary condition for the third term is just the negative of the sum of the contributions from the first two terms.

Let us now choose a definite coordinate system. The material will be assigned to the half-space $x_3 < 0$ and the origin will be placed directly above the source point $\vec{\xi}$, Figure 24. The solution for an arbitrarily located source point can be found by a simple translation of coordinates.
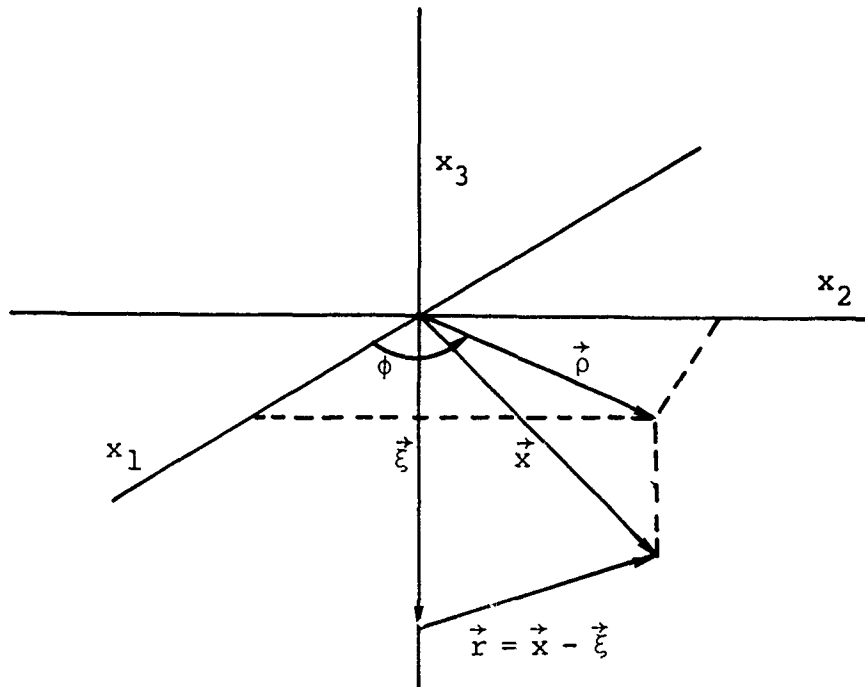
Figure 24.   Coordinate System Used in Green's Tensor
             Calculation.

The field due to the source given in Eq.(5.73) is well known,

$$G_{ij}^{(s)} = \frac{1}{4\pi\rho} \left\{ \left(\frac{3r_i r_j}{r^3} - \frac{\delta_{ij}}{r} \right) \int_{\frac{1}{c_\ell}}^{\frac{1}{c_t}} \lambda \delta(t-\lambda r) d\lambda \right.$$

$$+ \frac{r_i r_j}{r^3} \left[\frac{1}{c_\ell^2} \delta(t-\frac{1}{c_\ell}) - \frac{1}{c_t^2} \delta(t-\frac{r}{c_t}) \right]$$

$$+ \left. \frac{\delta_{ij}}{rc_t^2} \delta(t-\frac{r}{c_t}) \right\} \tag{5.56}$$

where $\vec{r} = \vec{x} - \vec{\xi}$. The integral is easily evaluated

$$\int_{\frac{1}{c_\ell}}^{\frac{1}{c_t}} \lambda \delta(t-\lambda r) d\lambda = \frac{t}{r^2} \left[\theta(t-\frac{r}{c_\ell}) - \theta(t-\frac{r}{c_t}) \right] \tag{5.57}$$

We see that $G_{ij}^{(s)}$ is singular at $r=0$ where it varies as $1/r$. The stress tensor corresponding to this field is found by substituting into Eq.(5.54).

$$T_{ikj}^{(s)} = \frac{1}{4\pi} \left\{ -6c_t^2 \left[5 \frac{r_i r_k r_j}{r^5} - \frac{\delta_{ij}r_k + \delta_{ik}r_j + \delta_{jk}r_i}{r^3} \right] \right.$$

$$\times \int_{\frac{1}{c_\ell}}^{\frac{1}{c_t}} \lambda \delta(t-\lambda r) d\lambda + 2 \left[6 \frac{r_i r_j r_k}{r^5} - \frac{\delta_{ij}r_k + \delta_{ik}r_j + \delta_{kj}r_i}{r^3} \right]$$

$$\times \left(\delta(t-\frac{r}{c_t}) - \frac{c_t^2}{c_\ell^2} \delta(t-\frac{r}{c_\ell}) \right) + 2 \frac{r_i r_j r_k}{r^4 c_t} \left[\dot{\delta}(t-\frac{r}{c_t}) \right.$$

$$\left. - \frac{c_t^3}{c_\ell^3} \dot{\delta}(t-\frac{r}{c_\ell}) \right] - \frac{r_j \delta_{ik}}{r^3} \left(1-2 \frac{c_t^2}{c_\ell^2} \right) \left[\delta(t-\frac{r}{c_\ell}) + \frac{r}{c_\ell} \dot{\delta}(t-\frac{r}{c_\ell}) \right]$$

$$\left. - \frac{(\delta_{ij}r_k + \delta_{kj}r_i)}{r^3} \left[\delta(t-\frac{r}{c_t}) + \frac{r}{c_t} \dot{\delta}(t-\frac{r}{c_t}) \right] \right\} \quad . \tag{5.58}$$

The surface stresses are

$$T_{(n)ij}^{(s)} = T_{ikj}^s n_k \tag{5.59}$$

where $\hat{n}$ is the unit outward normal to the surface which in this case is $\hat{n} = (0,0,1)$.

The second contribution to the Green's tensor will be chosen as the field due to the image of the source Eq.(5.52) found by reflecting in the $x_3=0$ plane. The reason for including this field explicitly rather than combining the second and third terms is that when the combined fields of the source and its image are substituted into the boundary condition Eq.(5.53), a number of terms cancel. The fields due to the image are given by Eqs.(5.56) and (5.58) when $\vec{\xi}$ is replaced by $-\vec{\xi}$ i.e., $\vec{\xi}_{source} = (0,0,-\xi)$ and $\vec{\xi}_{image} = (0,0,\xi)$ with $\xi>0$. Thus, since $\vec{r}=\vec{x}-\vec{\xi}$

$$\vec{r}_{source} = (x_1,x_2,x_3 + \xi) \tag{5.60}$$

$$\vec{r}_{image} = (x_1,x_2,x_3 - \xi) $$

On the boundary, $x_3=0$, we find

$$\vec{r}_{source_i} = \vec{r}_{image_i} \qquad i=1,2$$

$$\vec{r}_{source_3} = - \vec{r}_{image_3} \tag{5.61}$$

$$|\vec{r}_{source}| = |\vec{r}_{image}| \quad .$$

The combined contribution to the boundary condition is found by adding the individual contributions. From Eqs.(5.59) and (5.60), it is apparent that all terms will cancel which are proportional to an odd power of r_3 . By contracting Eq.(5.58) with $\hat{n}=(0,0,1)$, we easily find that

$$T^{(s)}_{(n)ij} + T^{(I)}_{(n)ij} = 0 \quad \text{for } i,j=1,2 \quad \text{or} \quad i=j=3 \quad . \tag{5.62}$$

When $i = 3$, $j \neq 3$ or $j = 3$, $i \neq 3$, the sum is not zero. For example, for $i = 1,2$,

$$T^{(s)}_{(n)i3} + T^{(I)}_{(n)i3} = \frac{1}{2\pi} \left\{ -6c_t^2 \left[5\frac{x_i \xi^2}{r^5} - \frac{x_i}{r^3} \right] \int_{\frac{1}{c_\ell}}^{\frac{1}{c_t}} \lambda \delta(t-\lambda r) d\lambda \right.$$

$$+ 2\left[6\frac{x_i \xi^2}{r^5} - \frac{x_i}{r^3} \right]\left(\delta(t-\frac{r}{c_t}) - \frac{c_t^2}{c_\ell^2}\delta(t-\frac{r}{c_\ell}) \right) + 2\frac{x_i \xi^2}{r^4 c_t}\left[\dot{\delta}(t-\frac{r}{c_t}) \right.$$

$$\left. - (\frac{c_t}{c_\ell})^3 \dot{\delta}(t-\frac{r}{c_\ell}) \right] - \frac{x_i}{r^3}\left[\delta(t-\frac{r}{c_t}) + \frac{r}{c_t}\dot{\delta}(t-\frac{r}{c_t}) \right] \right\} \quad . \qquad (5.63)$$

Each term is of the form x_i/r^n multiplied by either a delta function or its derivative. The problem of finding the Green's function thus reduces to finding solutions to the homogeneous wave equation which satisfy these two types of boundary conditions. When the individual solutions are found, it only remains to chose the linear combination which satisfies Eq. (5.53) to complete the derivation of the Green's tensor.

We seek solutions then to the following problems

$$\rho \left[c_t^2 G_{ij,\ell\ell} + (c_\ell^2 - c_t^2) G_{\ell j,\ell i} - \ddot{G}_{ij} \right] = 0 . \qquad (5.64)$$

$$T_{(n)ij} = 0 \quad i,j = 1,2 \text{ or } i = j = 3$$

$$T_{(n)i3} = A\frac{x_i}{r^n} F(t - \frac{r}{c}) \quad i = 1,2 \qquad (5.65)$$

$$T_{(n)3j} = A\frac{x_j}{r^n} F(t - \frac{r}{c}) \quad j = 1,2$$

where
$$F(t - \frac{r}{c}) = \begin{cases} \delta(t - \frac{r}{c}) \\ \dot{\delta}(t - \frac{r}{c}) \end{cases} \quad . \tag{5.66}$$

Notice that this problem can be treated by isolating each of the inhomogeneous boundary conditions. For example, one such problem would be set by requiring $T_{(n)ij} = 0$ for all i and j except for $T_{(n)i3} = A\frac{x_i}{r^n} F(t - \frac{r}{c})$.

While these problems do not appear to have been solved, the solutions to similar problems do exist.

First, we notice that since $T_{(n)ij}=0$ for $i,j=1,2$ and $i=j=3$ and there are no sources, we can set

$$G_{ij}=0 \quad i,j=1,2 \text{ and } i=j=3 \tag{5.67}$$

The nonzero components of G_{ij} are then G_{i3}, $i=1,2$ and G_{3i}, $j=1,2$. We will separate the problem into two parts corresponding to these two cases. The first will be treated explicitly; the second can be treated in an analogous manner. In order to simplify the notation, we define

$$u_i = G_{i3} \tag{5.68}$$

$$t_{ik} = T_{ik3} \tag{5.69}$$

$$t_{(n)i} = T_{(n)i3} = \left[\lambda \, \bar{\nabla}\cdot\bar{u} \, \delta_{ik} + \mu \left(\frac{\partial u_i}{\partial x_k} + \frac{\partial u_k}{\partial x_i} \right) \right] n_k \tag{5.70}$$

We define cylindrical coordinates (ρ, ϕ, z) such that (see Figure 24)

$$\vec{x} = (\rho\cos\phi,\ \rho\sin\phi, z) \tag{5.71}$$

$$\vec{\xi} = (0,0,-\xi) \tag{5.72}$$

It follows that

$$r^2 = x^2 + \xi^2 + 2z\xi = \rho^2 + z^2 + \xi^2 + 2z\xi \tag{5.73}$$

The unit vector normal to the surface is

$$\hat{n} = (0,0,1) \ . \tag{5.74}$$

The problem now becomes

$$c_t^2 \nabla^2 \vec{u} + (c_\ell^2 - c_t^2)\ \vec{\nabla}\ (\vec{\nabla}\cdot\vec{u}) - \ddot{\vec{u}} = 0 \tag{5.75}$$

$$t_{(n)i} = \lambda\vec{\nabla}\cdot\vec{u}\ \delta_{i3} + \mu\left(\frac{\partial u_i}{\partial x_3} + \frac{\partial u_3}{\partial x_i}\right) \tag{5.76}$$

with the boundary conditions

$$t_{(n)i}\Big|_{z=0} = \frac{A_1\ \rho\ F\left(t - \dfrac{r}{c}\right)}{\left(\rho^2 + \xi^2\right)^{\frac{n}{2}}}\ X\ \begin{cases} \cos\phi & i=1 \\[2ex] \sin\phi & i=2 \end{cases} \tag{5.77} \tag{5.78}$$

$$t_{(n)3}\Big|_{z=0} = 0 \tag{5.79}$$

Using Eq.(5.76), Eqs.(5.77) to (5.79) become in rectangular Cartesian coordinates

$$\left(\frac{\partial u_x}{\partial z} + \frac{\partial u_z}{\partial x} \right)\Bigg|_{z=0} = \frac{A_1}{\mu} \; \frac{\rho \cos\phi}{\left(\rho^2 + \xi^2 \right)^{\frac{n}{2}}} \; F\left(t - \frac{r}{c} \right) \tag{5.80}$$

$$\left(\frac{\partial u_y}{\partial z} + \frac{\partial u_y}{\partial y} \right)\Bigg|_{z=0} = \frac{A_1}{\mu} \; \frac{\rho \sin\phi}{\left(\rho^2 + \xi^2 \right)^{\frac{n}{2}}} \; F\left(t - \frac{r}{c} \right) \tag{5.81}$$

$$\lambda \left(\frac{\partial u_x}{\partial x} + \frac{\partial u_y}{\partial y} \right)\Bigg|_{z=0} + (\lambda+2\mu) \; \frac{\partial u_z}{\partial z}\Bigg|_{z=0} = 0 \tag{5.82}$$

We now express $\vec{u}$ in terms of a scalar and a vector potential

$$\vec{u} = \vec{\nabla}\eta + \vec{\nabla} \times \vec{\psi} \tag{5.83}$$

where

$$\nabla \cdot \vec{\psi} = 0 \; . \tag{5.84}$$

The wave equation then separates into equations for η and $\vec{\psi}$

$$\nabla^2 \eta - \frac{1}{c_\ell^2} \; \ddot{\eta} = 0 \tag{5.85}$$

$$\nabla^2 \vec{\psi} - \frac{1}{c_t^2} \; \ddot{\vec{\psi}} = 0 \tag{5.86}$$

The problem thus becomes that of solving Eq.(5.85) and (5.86) with the subsidiary condition Eq.(5.84) and the boundary conditions Eqs.(5.80) to (5.82).

By using the Laplace transform, we can eliminate the time dependence in these equations. Define

$$\bar{\eta}(s) = \int_0^\infty e^{-st} \eta(t) \, dt \qquad (5.87)$$

$$\bar{\psi}_i(s) = \int_0^\infty e^{-st} \psi_i(s) dt \qquad (5.88)$$

$$\bar{F}(r,s) = \int_0^\infty e^{-st} F(t - \frac{r}{c}) \, dt \qquad (5.89)$$

The latter transform can be given explicitly using the definition of $F(t - \frac{r}{c})$,

$$\bar{F}(r,s) = \begin{cases} e^{-\frac{rs}{c}} & \text{for } F(t - \frac{r}{c}) = \delta(t - \frac{r}{c}) \\ \left[se^{-\frac{rs}{c}} - c\delta(r) \right] & \text{for } F(t - \frac{r}{c}) = \dot{\delta}(t - \frac{r}{c}) \end{cases} \qquad (5.90)$$

Further,

$$\ddot{\bar{\eta}}(s) = s^2 \bar{\eta}(s) - \dot{\eta}(0) - s\eta(0) \qquad (5.91)$$

$$\ddot{\bar{\psi}}_i(s) = s^2 \bar{\psi}_i(s) - \dot{\psi}_i(0) - s\psi_i(0) . \qquad (5.92)$$

Using the initial conditions

$$\eta(0) = \dot{\eta}(0) = \psi_i(0) = \dot{\psi}_i(0) = 0 \qquad (5.93)$$

The wave equations, Eqs.(5.85) and (5.86), become (omitting the bar notation for transformed quantities)

$$(\nabla^2 - k_1^{\;2})\eta = 0 \tag{5.94}$$

$$(\nabla^2 - k_2^{\;2})\vec{\psi} = 0 \tag{5.95}$$

where

$$k_1 = \frac{s}{c_\ell} \tag{5.96}$$

$$\kappa_2 = \frac{s}{c_t} \tag{5.97}$$

These equations written in cylindrical coordinates become

$$(\nabla^2 - k_1^{\;2})\,\eta = 0 \tag{5.98}$$

$$\nabla^2 \psi_\rho - \frac{1}{\rho^2}\,\psi_\rho - \frac{2}{\rho^2}\,\frac{\partial \psi_\phi}{\partial \phi} - k_2^{\;2}\psi_\rho = 0 \tag{5.99}$$

$$\nabla^2 \psi_\phi - \frac{1}{\rho^2}\,\psi_\phi + \frac{2}{\rho^2}\,\frac{\partial \psi_\rho}{\partial \phi} - k_2^{\;2}\,\psi_\phi = 0 \tag{5.100}$$

$$(\nabla^2 - k_2^{\;2})\,\psi_z = 0 \tag{5.101}$$

where

$$\nabla^2 = \frac{1}{\rho}\,\frac{\partial}{\partial \rho}\left(\rho \frac{\partial}{\partial \rho}\right) + \frac{1}{\rho^2}\,\frac{\partial^2}{\partial \phi^2} + \frac{\partial^2}{\partial z^2} \tag{5.102}$$

The divergence condition Eq.(5.84) becomes

$$\frac{\partial \psi_\rho}{\partial \rho} + \frac{\psi_\rho}{\rho} + \frac{1}{\rho}\frac{\partial \psi_\phi}{\partial \phi} + \frac{\partial \psi_z}{\partial z} = 0 \tag{5.103}$$

The boundary conditions can also be expressed in cylindrical coordinates. The results are

$$\left(\frac{\partial u_\rho}{\partial z} + \frac{\partial u_z}{\partial \rho}\right)\Bigg|_{z=0} = \frac{A}{\mu} \rho \frac{\overline{F}(r_o, s)}{r_o^{\frac{n}{2}}} \tag{5.104}$$

$$\left(\frac{\partial u_\rho}{\partial z} + \frac{1}{\rho} \frac{\partial u_z}{\partial \phi}\right)\Bigg|_{z=0} = 0 \tag{5.105}$$

$$\lambda\left(\frac{\partial u_\rho}{\partial \rho} + \frac{u_\rho}{\rho} + \frac{1}{\rho} \frac{\partial u_\phi}{\partial \phi}\right)\Bigg|_{z=0} + (\lambda + 2\mu) \frac{\partial u_z}{\partial z}\Bigg|_{z=0} = 0 \tag{5.106}$$

where $\quad r_o^2 = \rho^2 + \xi^2 \quad$ and

$$\vec{u} = u_\rho \hat{\rho} + u_\phi \hat{\phi} + u_z \hat{z} \tag{5.107}$$

$$u_\rho = \frac{\partial \eta}{\partial \rho} + \frac{1}{\rho} \frac{\partial \psi_z}{\partial \phi} - \frac{\partial \psi_\phi}{\partial z} \tag{5.108}$$

$$u_\phi = \frac{1}{\rho} \frac{\partial \eta}{\partial \phi} + \frac{\partial \psi_\rho}{\partial z} - \frac{\partial \psi_z}{\partial \rho} \tag{5.109}$$

$$u_z = \frac{\partial \eta}{\partial z} + \frac{\partial \psi_\phi}{\partial \rho} + \frac{\psi_\phi}{\rho} - \frac{1}{\rho} \frac{\partial \psi_\rho}{\partial \phi} \tag{5.110}$$

We notice that the boundary conditions do not depend on ϕ when written in cylindrical coordinates. This being the case, it is natural to seek a solution which is also independent of ϕ. Such a solution does in fact exist.

The solution in terms of Hankel transforms which satisfies the wave equations, the divergence condition, and the boundary condition Eq.(5.105) is

$$\eta(s) = \int_0^\infty B_\eta(\beta) \, e^{\sqrt{\beta^2 + k_1^2}\, z} \, J_0(\rho\beta) \, d\beta \tag{5.111}$$

$$\psi_\phi(s) = \int_0^\infty B_\phi(\beta) \, e^{\sqrt{\beta^2 + k_2^2}\, z} \, J_1(\rho\beta) \, d\beta \tag{5.112}$$

$$\psi_\rho(s) = \psi_z(s) = 0 \tag{5.113}$$

The coefficients B_η and B_ϕ are found by substituting into Eq.(5.104) and (5.106). After some algebra, the result is found to be

$$B_\eta = \frac{\beta^2 \sqrt{\beta^2 + k_2^2}}{D(s,\beta)} \, I \tag{5.114}$$

$$B_\phi = \frac{-\beta \left(\beta^2 + k_2^2/2\right)}{D(s,\beta)} \, I \tag{5.115}$$

where

$$I = \int_0^\infty d\sigma \, \sigma J_1(\beta\sigma) \, \frac{A}{\mu} \, \frac{\sigma}{\left(\sigma^2 + \xi^2\right)^{n/2}} \, \overline{F}\left(\sqrt{\sigma^2 + \xi^2}, s\right) \tag{5.116}$$

$$D(s,\beta) = 2\left\{ (\beta^2 + k_2^2/2)^2 - \beta^2 \sqrt{(\beta^2 + k_1^2)(\beta^2 + k_2^2)} \right\} \tag{5.117}$$

$$= \frac{2s^4}{c_t^4} \, D(\zeta) \tag{5.118}$$

$$D(\zeta) = (1/2+\zeta)^2 - \zeta\sqrt{(1+\zeta)(\gamma^2+\zeta)} \qquad (5.119)$$

$$\zeta = \left(\frac{\beta c_t}{s}\right)^2 \qquad (5.120)$$

$$\gamma^2 = \left(\frac{c_t}{c_\ell}\right)^2 = \frac{1-2\nu}{2(1-\nu)} \quad . \qquad (5.121)$$

In this last relation, ν is Poisson's ratio. Since for all materials, $0<\nu<1/2$, it follows that $0<\gamma^2<1/2$. In particular, for $\nu=1/3$ which is a value typical of many materials, $\gamma^2 \simeq 1/4$ or $\gamma \simeq 1/2$.

From Eq.(5.108) to (5.110), we find (including again the bar notation),

$$\bar{u}_\rho(s) = -\int_0^\infty \left[B_\eta\,\beta e^{\sqrt{\beta^2+k_1^2}\,z} + B_\phi\sqrt{\beta^2+k_2^2}\,e^{\sqrt{\beta^2+k_2^2}\,z}\right] J_1(\beta\rho)d\beta \qquad (5.122)$$

$$\bar{u}_\phi(s) = 0 \qquad (5.123)$$

$$\bar{u}_z(s) = \int_0^\infty \left[B_\eta\sqrt{\beta^2+k_1^2}\,e^{\sqrt{\beta^2+k_1^2}\,z} + B_\phi\,\beta e^{\sqrt{\beta^2+k_2^2}\,z}\right] J_0(\beta\rho)d\beta \qquad (5.124)$$

The inverse Laplace transform gives the time dependent displacements

$$u_i(\rho,z,t) = \frac{1}{2\pi i}\int_{\alpha-i\infty}^{\alpha+i\infty} e^{st}\,\bar{u}_i(s)\,ds \qquad (5.125)$$

This completes the formal solution to the problem. The remaining problems are to evaluate the required integrals and to collect the various contributions to form the complete Green's tensor.

4. PROCEDURES FOR EVALUATING THE RESULTANT INTEGRAL EXPRESSIONS

We will examine the first integral of Eq.(5.122) for the case $F(r,t) = \delta(t-r/c)$. The others have the same general form and can be evaluated in a similar fashion. We define

$$H(t) = \frac{1}{2\pi i} \int_{\alpha-i\infty}^{\alpha+i\infty} e^{st} H(s) \, ds \tag{5.126}$$

$$H(s) = -\int_{0}^{\infty} B_\eta \, 3 \, e^{\sqrt{\beta^2+k_1^2}\, z} J_1(\beta\rho) \, d\beta \tag{5.127}$$

Our intention is to reverse the order of the s and the β and σ integrations. In order to justify this step, it is necessary to show that the integrals converge. We will assume for the present that $z<0$ and leave until later the limiting case $z=0$.

For s real and positive, it is obvious that the σ integration converges and when in addition $z<0$, it is equally obvious that the β integration also converges provided the denominator does not vanish for β positive and real. It has been shown, however, (Lamb, 1907) that $D(\zeta)$ has a simple zero for a value of $\zeta<-1$ and thus in view of the definition of ζ , $D(s,\beta)$ does not vanish for β in the range of integration and s real. Since both integrals converge for any s positive and real, the integrated result defines an analytic continuation for s not real; in particular along the line $\alpha-i\infty$ to $\alpha+i\infty$ where $\alpha=\text{Re}(s)$ lies to the right of any singularities in the s plane.

Because the integrals do converge, we can reverse the order of integration and study the properties of the s integration first. We define a function $G(t)$

$$G(t) = \frac{1}{2\pi i} \int_{\alpha-i\infty}^{\alpha+i\infty} ds \, e^{st} B(s,\beta) \, e^{-\sqrt{\beta^2+k_1^2}\,|z|} \, e^{-\frac{s}{c}\sqrt{\sigma^2+\xi^2}} \tag{5.128}$$

95

then

$$H(t) = -\frac{A}{\mu} \int_0^\infty d\beta \, \beta^3 \, J_1(\beta\rho) \int_0^\infty \frac{d\sigma \, \sigma^2}{(\sigma^2+\xi^2)^{n/2}} \, J_1(\beta\sigma) \, G(t) \tag{5.129}$$

where

$$B(s,\beta) = \frac{\sqrt{\beta^2+k_2^2}}{D(s,\beta)} \tag{5.130}$$

For notational convenience, we will change the variable of integration from s to the real variable y where $s=\alpha+iy$. As we will show, all the singularities lie along the imaginary s axis or equivalently, the real y axis and consequently we can set $\alpha=0$ with the understanding that the integration contour passes below all the singularities in the y plane. In terms of y, the function $G(t)$ becomes

$$G(t) = \frac{1}{2\pi} \int_{-\infty}^\infty dy \, e^{iy\left[t-\frac{1}{c}\sqrt{\sigma^2+\xi^2}\right]} e^{-\sqrt{\beta^2-\frac{y^2}{c_\ell^2}}\,|z|}$$

$$\frac{\sqrt{\beta^2-\frac{y^2}{c_t^2}}}{2\left[\left(\beta^2-\frac{y^2}{2c_t^2}\right)^2 - \beta^2\sqrt{\left(\beta^2-\frac{y^2}{c_\ell^2}\right)\left(\beta^2-\frac{y^2}{c_t^2}\right)}\right]} \tag{5.131}$$

The singularities in y result from the branch cuts of the two radials, the simple zero of $D(y,\beta)$ at $\zeta<-1$ and the asymptotic behavior of $D(\zeta)$ for large ζ. In the latter case, it happens that $D(y,\beta)$ is proportional to y^2 and thus the integrand has a second order pole at $y=0$. To show this, we expand about $y=0$ (which in view of Eq.(5.120) is large ζ)

$$D = 2\left[\beta^4 - \frac{\beta^2 y^2}{c_t^2} + \frac{y^4}{2c_t^4} - \beta^4\left(1 - \frac{y^2}{\beta^2 c_\ell^2}\right)^{1/2}\left(1 - \frac{y^2}{\beta^2 c_t^2}\right)^{1/2}\right] \qquad (5.132)$$

$$= 2\left[\beta^4 - \frac{\beta^2 y^2}{c_t^2} - \beta^4\left(1 - \frac{y^2}{2\beta^2 c_\ell^2} - \frac{y^2}{2\beta^2 c_t^2}\right) + 0(y^4)\right] \qquad (5.133)$$

$$= -\frac{\beta^2}{c_t^2}\left[1 - \gamma^2\right]y^2 + 0(y^4) \qquad (5.134)$$

As mentioned earlier, $D(\zeta)$ has a simple pole at a value of real $\zeta < -1$. Since $\zeta = \left(\dfrac{\beta c_t}{iy}\right)^2$, this will result in a pair of simple poles in the y plane at

$$-\frac{\beta^2 c_t^2}{y^2} = -1 - \delta \qquad \delta > 0 \text{ , real} \qquad (5.135)$$

or

$$y = \pm \frac{\beta c_t}{\sqrt{1+\delta}} \qquad (5.136)$$

The equation which determines δ is

$$(1/2 + \delta)^2 - (1 + \delta)\sqrt{\delta(1 + \delta - \gamma^2)} = 0 \qquad (5.137)$$

and thus δ is a function only of γ (where $\gamma = c_t/c_\ell$) which in turn depends only on Poisson's ratio.

The remaining singularities are the branch cuts at $y = \pm\beta c_t$ and $\pm\beta c_\ell$. We chose the phase of the two radicals by requiring these to be real when β and s are real. Then

$$\sqrt{\beta^2 - \frac{y^2}{c_\ell^2}} = \left\{ \left| \beta - \frac{y}{c_\ell} \right| \left| \beta + \frac{y}{c_\ell} \right| \right\}^{1/2} e^{i\frac{\left(\theta_1 + \theta_4 - \pi\right)}{2}} \tag{5.138}$$

$$\sqrt{\beta^2 - \frac{y^2}{c_t^2}} = \left\{ \left| \beta - \frac{y}{c_t} \right| \left| \beta + \frac{y}{c_t} \right| \right\}^{1/2} e^{i\frac{\left(\theta_2 + \theta_3 - \pi\right)}{2}} \tag{5.139}$$

where the θ_i are defined in Figure 25. Also indicated are the branch cuts, the poles and the integration contour.

Let us first consider the limit of large y in the lower half plane. By continuing in y between the cuts, (Figure 26), we find

$$\theta_1 = \theta_2 \to 2\pi - |\theta| \tag{5.140}$$

$$\lim_{|y| \to \infty} \quad \theta_3 = \theta_4 \to -|\theta| \tag{5.141}$$

where
$$\theta = -|\theta| \tag{5.142}$$

Thus

$$\lim_{|y| \to \infty} \sqrt{\beta^2 - \frac{y^2}{c_\ell^2}} = i|y| e^{-i|\theta|} = \frac{iy}{c_\ell} \tag{5.143}$$

$$\lim_{|y| \to \infty} \sqrt{\beta^2 - \frac{y^2}{c_t^2}} = \frac{iy}{c_t} \tag{5.144}$$

In this same limit

$$D(y,\beta) \to \frac{y^4}{2c_t^4} \left[1 + 0\left(\frac{1}{y^2}\right) \right] \tag{5.145}$$
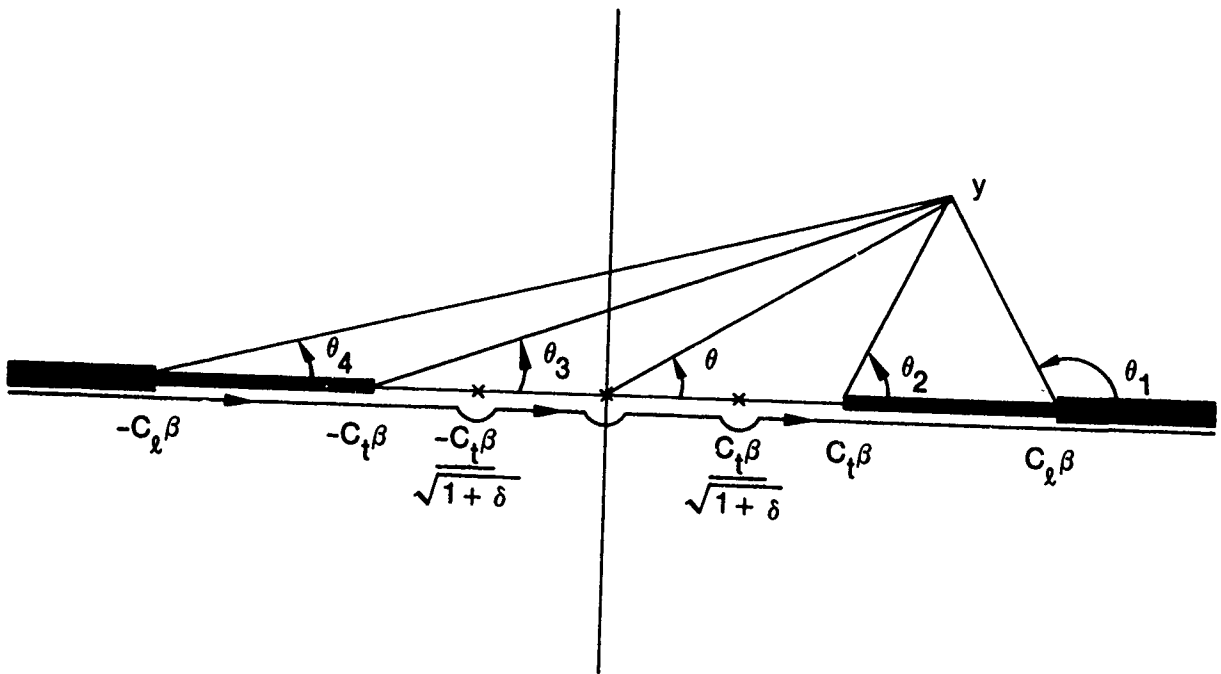
Figure 25.   Complex y plane showing singularities and integration contour.
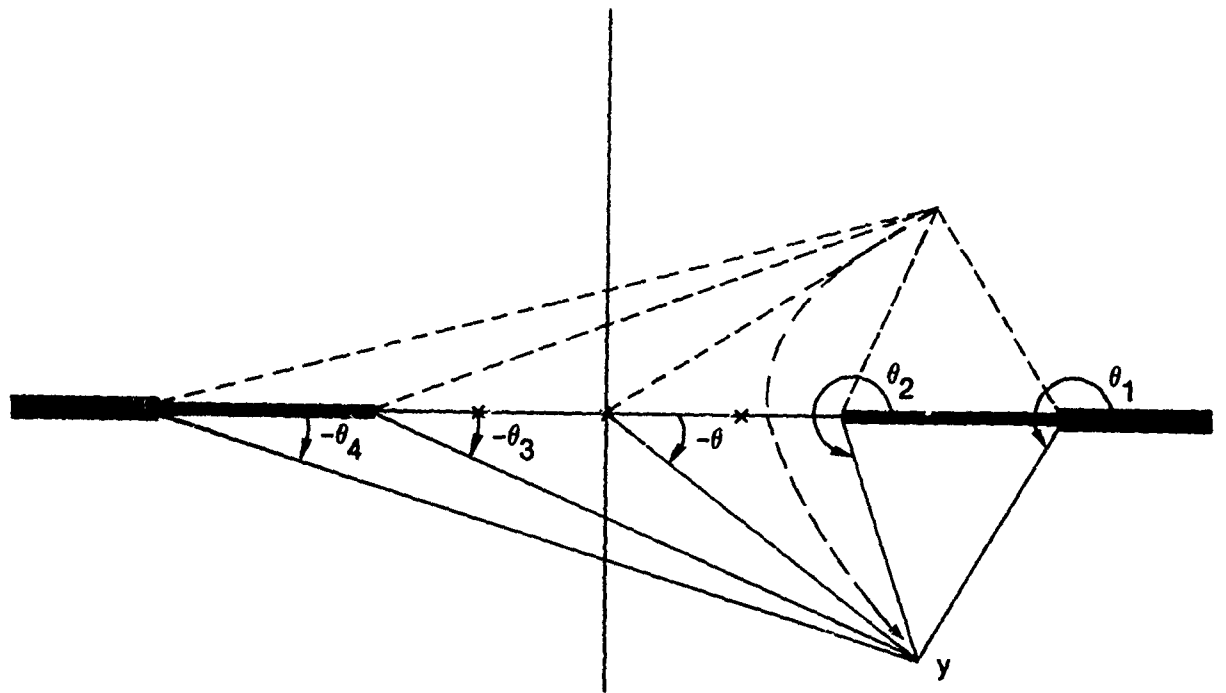
Figure 26. Continuation path into lower half
of the complex y plane.

so that the integrand becomes

$$\frac{2ic_t^3}{y^3} \, e^{iy\left[t - \frac{1}{c}\sqrt{\sigma^2 + \xi^2} - \frac{|z|}{c_\ell}\right]} \tag{5.146}$$

We see than that if $T < 0$ where

$$T = t - \frac{1}{c}\sqrt{\sigma^2 + \xi^2} - \frac{|z|}{c_\ell} \tag{5.147}$$

then the integrand will vanish everywhere on the semicircle as $|y| \to \infty$.
We can thus close the integration contour by including the semicircle
since its contribution is zero. Since there are no singularities in the
lower half plane, by Cauchy's theorem we find that $G(t)$ vanishes for
$T < 0$. Thus

$$G(t) \propto \theta\left(t - \frac{1}{c}\sqrt{\sigma^2 + \xi^2} - \frac{|z|}{c_\ell}\right) \tag{5.148}$$

where

$$\theta(t) = \begin{cases} 1 & t > 0 \\ 0 & t < 0 \end{cases} \tag{5.149}$$

In the upper half plane in the limit of large $|y|$, we find

$$\lim_{|y| \to \infty} \theta_1 = \theta_2 = \theta_3 = \theta_4 = \theta \tag{5.150}$$

and thus

$$\lim_{|y|\to\infty} \sqrt{\beta^2 - \frac{y^2}{c_\ell^2}} = \frac{-iy}{c_\ell} \tag{5.151}$$

$$\lim_{|y|\to\infty} \sqrt{\beta^2 - \frac{y^2}{c_t^2}} = \frac{-iy}{c_t} \tag{5.152}$$

The integrand becomes

$$\frac{-2ic_t^3}{y^3} \, e^{iy\left[t - \frac{1}{c}\sqrt{\sigma^2+\xi^2} + \frac{|z|}{c_\ell}\right]} \tag{5.153}$$

and since

$$t - \frac{1}{c}\sqrt{\sigma^2+\xi^2} + \frac{|z|}{c_\ell} = T + \frac{2|z|}{c_\ell} \tag{5.154}$$

the integrand vanishes on the upper semicircle for $|y|\to\infty$ whenever $T > 0$.

We can now deform the integration contour into the upper half-plane as indicated in Figure 27. From this it follows that

$$\int_{-\infty}^{\infty} dy = \int_{-\infty}^{-c_t\beta} + \oint + \int_{-c_t\beta}^{-\infty} + \oint_{-c_t\beta} + \int_{\infty}^{c_t\beta} + \oint_{c_t\beta} + \int_{c_t\beta}^{\infty} \tag{5.155}$$

$$+ \oint_{\frac{c_t\beta}{\sqrt{1+\delta}}} + \oint_{\frac{-c_t\beta}{\sqrt{1+\delta}}} + \oint_{o}$$

As we have just seen, the integral over the semicircle at $|y|\to\infty$ vanishes,

$$\oint_{\infty} = 0 \tag{5.156}$$
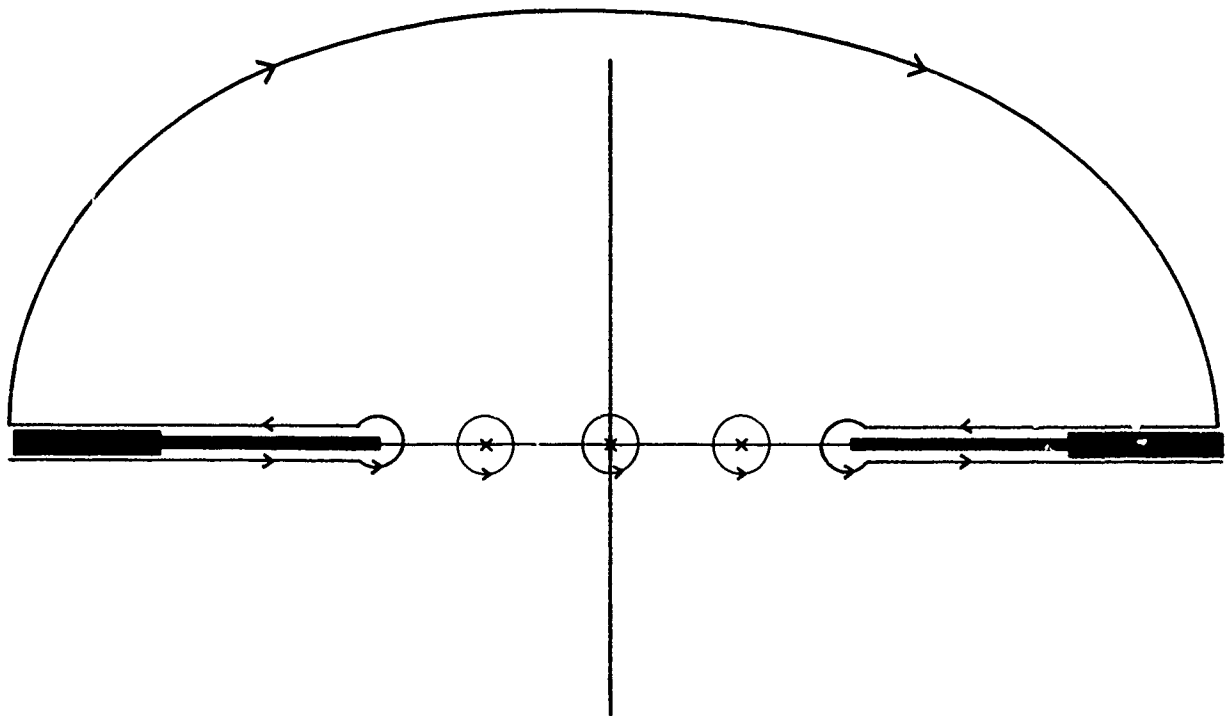
Figure 27. Integration contour deformed into the upper half of the complex y plane.

Also, since the integrand is proportional to $\sqrt{\beta^2 - \dfrac{y^2}{c_t^2}}$, the two

integrals around the branch points also vanish.

$$\oint_{c_2\beta} = \oint_{-c_2\beta} = 0 \tag{5.157}$$

The remaining contributions are nonzero. The contribution from the second order pole at $y=0$ is

$$\oint_o = 2\pi i \ \lim_{y \to 0} \ \frac{d}{dy} \left\{ y^2 I(y) \right\} \tag{5.158}$$

where $I(y)$ is the integrand of $G(t)$,

$$I(y) = \frac{1}{2\pi} e^{iy\left[t - 1/2 \ \sqrt{\sigma^2 + \xi^2} \right] - \sqrt{\beta^2 - \frac{y^2}{c_\ell^2}}\,|z|} \ x \ \frac{\sqrt{\beta^2 - \dfrac{y_2}{c_t^2}}}{D(y,\beta)} \tag{5.159}$$

It is easily determined that

$$\oint_o = \frac{c_t^2}{\beta(1-\gamma^2)} \left(t - \frac{1}{c} \sqrt{\sigma^2 + \xi^2} \right) e^{-\beta|z|} \tag{5.160}$$

Next, consider the simple poles at $y_\delta = \pm \dfrac{c_t \beta}{\sqrt{1+\delta}}$. Since $D(y,\beta)$ has simple zeros at these points, we can write

$$D(y,\beta) = D(y_\delta,\beta) + (y-y_\delta) \ D'(y_\delta,\beta) + \dots \tag{5.161}$$

where $D(y_\delta, \beta) = 0$. The residue theorem gives

$$\oint_{\frac{c_2\beta}{\sqrt{1+\delta}}} + \oint_{\frac{-c_2\beta}{\sqrt{1+\delta}}} = i\, e^{-\sqrt{\beta^2 - \frac{y_\delta^2}{c_\ell^2}}\,|z|}\, \sqrt{\beta^2 - \frac{y_\delta^2}{c_t^2}} \tag{5.162}$$

$$\times \left\{ \frac{e^{iy_\delta \left(t - \frac{1}{c}\sqrt{\sigma^2 + \xi^2}\right)}}{D'(y_\delta)} + \frac{e^{-iy_\delta \left(t - \frac{1}{c}\sqrt{\sigma^2 + \xi^2}\right)}}{D'(-y_\delta)} \right\}$$

$$= \frac{-2\beta \sqrt{\frac{\delta}{1+\delta}}\, e^{-\sqrt{1 - \frac{\gamma^2}{1+\delta}}\,\beta|z|}}{D'(y_\delta)}\, \sin\left[y_\delta \left(t - \frac{1}{c}\sqrt{\sigma^2 + \xi^2} \right) \right] \tag{5.163}$$

Here

$$D'(y_\delta) = \frac{2\beta^3}{c_t\sqrt{1+\delta}\,(1+2\delta)^2} \left\{ \frac{3 + 6\delta - 4\delta^3}{1+\delta} - 4\gamma^2(1-\delta^2) \right\} \tag{5.164}$$

To simplify notation, we will define

$$E(\gamma^2) = \frac{\sqrt{\delta}\,(1+2\delta)^2}{\left[\frac{3+6\delta-4\delta^3}{1+\delta} - 4\gamma^2(1-\delta^2) \right]} \tag{5.165}$$

then
$$\oint_{y_\delta} + \oint_{-y_\delta} = \frac{c_t}{\beta^2} E(\gamma^2)\ e^{-\sqrt{1-\frac{\gamma^2}{1+\delta}}\,\beta|z|}\ \sin\left[y_\delta\left(t - \frac{1}{c}\sqrt{\sigma^2+\xi^2}\right)\right] \tag{5.166}$$

The integrals along the right hand cut can be combined to give

$$\int_\infty^{c_t\beta} + \int_{c_t\beta}^\infty = \int_{c_t\beta}^\infty dy\left[I(y-io) - I(y+io)\right] \tag{5.167}$$

This must be separated into the regions $c_t\beta < y < c_\ell\beta$ and $y > c_\ell\beta$. In the region $c_t\beta < y < c_\ell\beta$, the radicals have the values

$$\sqrt{\beta^2 - \frac{y^2}{c_\ell^2}} = \text{real} \tag{5.168}$$

$$\sqrt{\beta^2 - \frac{y^2}{c_t^2}} = \sqrt{\frac{y^2}{c_t^2} - \beta^2}\ \times\ \begin{cases} -i & \text{above cut} \\ \ i & \text{below cut} \end{cases} \tag{5.169}$$

and thus

$$D(y,\beta) = 2\left[\left(\beta^2 - \frac{y^2}{2c_t^2}\right)^2 \pm i\beta^2\sqrt{\left(\beta^2 - \frac{y^2}{c_\ell^2}\right)\left(\frac{y^2}{c_t^2} - \beta^2\right)}\right] \tag{5.170}$$

with the $\pm$ sign corresponding to y above or below the cut. The resulting integral is obtained by substituting into Eq.(5.167). If we include also the contribution from the left hand cut, we obtain

$$\int_{c_t\beta}^{c_\ell\beta} + \int_{-c_t\beta}^{-c_\ell\beta} = -\frac{1}{\pi}\int_{c_t\beta}^{c_\ell\beta} dy \frac{\sqrt{\dfrac{y^2}{c_t^2} - \beta^2}\left(\beta^2 - \dfrac{y^2}{2c_t^2}\right)^2}{\left[\left(\beta^2 - \dfrac{y^2}{2c_t^2}\right)^4 + \beta^4\left(\beta^2 - \dfrac{y^2}{c_\ell^2}\right)\left(\dfrac{y^2}{c_t^2} - \beta^2\right)\right]}$$

$$-\sqrt{\beta^2 - \dfrac{y^2}{c_\ell^2}}\,|z|$$
$$x \quad e \qquad\qquad \sin\left[y\left(t - \frac{1}{c}\sqrt{\sigma^2 + \xi^2}\right)\right]$$

(5.171)

Next, for $y > c_\ell\beta$, we have in addition to Eq.(5.169)

$$\sqrt{\beta^2 - \frac{y^2}{c_\ell^2}} = \sqrt{\frac{y^2}{c_\ell^2} - \beta^2} \; x \; \begin{cases} -i & \text{above cut} \\ \\ i & \text{below cut} \end{cases}$$

(5.172)

and

$$D(y,\beta) = 2\left[\left(\beta^2 - \frac{y^2}{2c_t^2}\right)^2 + \beta^2\sqrt{\left(\frac{y^2}{c_\ell^2} - \beta^2\right)\left(\frac{y^2}{c_t^2} - \beta^2\right)}\right]$$

(5.173)

Note that $D(y,\beta)$ is cut only between $c_t\beta < y < c_\ell\beta$. The combined integrals give

$$\int_{c_\ell\beta}^{\infty} + \int_{-c_\ell\beta}^{-\infty} = -\frac{1}{\pi}\int_{c_\ell\beta}^{\infty} dy \frac{\sqrt{\dfrac{y^2}{c_\ell^2} - \beta^2}\,\cos\left[\sqrt{\dfrac{y^2}{c_\ell^2} - \beta^2}\,|z|\right]\sin\left[y\left(t - \dfrac{1}{c}\sqrt{\sigma^2 + \xi^2}\right)\right]}{\left(\beta^2 - \dfrac{y^2}{2c_t^2}\right)^2 + \beta^2\sqrt{\left(\dfrac{y^2}{c_\ell^2} - \beta^2\right)\left(\dfrac{y^2}{c_t^2} - \beta^2\right)}}$$

(5.174)

107

The function $G(t)$ is obtained by adding these contributions. Defining a new integration variable

$$w = y/c_t \beta \tag{5.175}$$

we obtain

$$
\begin{aligned}
G(t) = \theta(T) \frac{c_t}{\beta^2} &\left\{ \frac{\tau e^{-\beta|z|}}{1-\gamma^2} - E(\gamma^2) \, e^{-\sqrt{1-\frac{r^2}{1+\delta}}\,\beta|z|} \sin\!\left(\frac{\tau}{\sqrt{1+\delta}}\right) \right. \\[4pt]
&\left. - \frac{1}{\pi} \int_1^{1/\gamma} dw \; \frac{\sqrt{w^2-1}\left(1-\frac{w^2}{2}\right)^2}{\left(1-\frac{w^2}{2}\right)^4 + \left(1-w^2\gamma^2\right)\left(w^2-1\right)} \, e^{-\sqrt{1-\gamma^2 w^2}\,\beta|z|} \sin(\tau w) \right.
\end{aligned}
$$

$$(5.176)$$

$$
\left. - \frac{1}{\pi} \int_{1/\gamma}^{\infty} dw \; \frac{\sqrt{w^2-1}\,\cos\!\left[\sqrt{\gamma^2 w^2-1}\,\beta|z|\right]}{\left(1-\frac{w^2}{2}\right)^2 + \sqrt{(w^2\gamma^2-1)(w^2-1)}} \, \sin(\tau w) \right\}
$$

where

$$
\tau = c_t \beta \left(t - \frac{1}{c} \sqrt{\sigma^2+\xi^2} \right) > 0 \tag{5.177}
$$

The inequality follows from $T > 0$. The integrands of the above integrals are well defined in the range of integration. $H(t)$ is now found by substituting into Eq.(5.129). Because of the limits imposed by $\theta(T)$, the range of integration for the σ integral becomes

108

$$0 < \sigma < \left\{ c^2 \left(t - \frac{|z|}{c_\ell} \right)^2 - \xi^2 \right\}^{1/2} \qquad (5.178)$$

and consequently this integral always converges.

The β integration of the first three terms of Eq.(5.176) also converges because of the decaying exponentials. To show that the last term results in a convergent integral, we need an estimate of the asymptotic behvaior of the last term of Eq. (5.176). The denominator is a monotonically increasing function of w and can be written

$$\left(1 - \frac{w^2}{2} \right)^2 + \sqrt{(w^2\gamma^2 - 1)(w^2 - 1)} = \frac{w^4}{4} \left\{ \left(1 - \frac{2}{w^2} \right)^2 + \frac{1}{w^2} \sqrt{\left(\gamma^2 - \frac{1}{w^2} \right) \left(1 - \frac{1}{w^2} \right)} \right\}$$

$$= \frac{w^4}{4} F(w^2) \qquad (5.179)$$

where $F(w^2)$ is also a monotonic function of w^2 (this is not an obvious conclusion). To obtain a bound on the integral, we can replace $F(w^2)$ by its largest value, namely unity. Also in the numerator, we can replace the radical by its large w limit and the cosine by unit, thus

$$\int_{1/\gamma}^{\infty} dw \frac{\sqrt{w^2 - 1} \cos\left[\sqrt{w^2\gamma^2 - 1} \ \beta |z| \right] \sin \tau w}{\left[\left(1 - \frac{w^2}{2} \right)^2 + \sqrt{\left(w^2\gamma^2 - 1 \right) \left(w^2 - 1 \right)} \right]} \qquad (5.180)$$

$$\leq \int_{1/\gamma}^{\infty} dw \frac{w \sin \tau w}{\frac{w^4}{4}} = 4 \int_{1/\gamma}^{\infty} dw \frac{\sin \tau w}{w^3} \tag{5.180}$$

Integration by parts shows that this last integral is

$$4 \int_{1/\gamma}^{\infty} dw \frac{\sin \tau w}{w^3} = \frac{4\gamma^3}{\tau} \cos \tau/\gamma + \frac{3\gamma^4}{\tau^2} \sin \tau/\gamma + \dots \tag{5.181}$$

Thus the least convergent of the β integrations is bounded by

$$\int_{0}^{\infty} d\beta \, \beta \, J_1(\beta\rho) \quad J_1(\beta\sigma) \times \frac{\cos(\Gamma \, \beta)}{\beta} \tag{5.182}$$

which is a convergent integral [see W.N. Bailey (1936)].

We have now shown that the required integrals are convergent. They can be evaluated by a combination of analytic and numerical techniques. The limiting cases of $|z| = 0$ and $\xi = 0$ can be studied by consideration of the β and σ integrals in Eq.(5.176) as these limits are approached.

SECTION VI

FRACTURE ASSOCIATED WITH WATER DROP COLLISIONS

The critical fracture problems identified as the major contributors to the degradation of zinc sulfide infrared-transparent windows are fracture initiation due to the transient stresses generated by the water drop impact and crack propagation due to hydraulic penetration of the cracks which exist after the initial water drop collision. The initial fractures in polycrystalline zinc sulfide display a high level of insensitivity to subsequent stress wave interactions as observed microscopically for inter-secting ring fracture formations. At a limited number of sites, crack bi-furcation is noted where one fracture surface propagated in the direction of the critical stress associated with the first drop impact and the second fracture surface propagated in conformity with the stress states generated by the second drop in the absence of any initia.. fractures. While limited crack growth can be assigned to the stress wave interaction mechanism, it is conjectured that crack growth by hydraulic penetration is the dominant damage mechanism up to the time at which a significant population of erosion pits exists on the specimen's surface. At this point, material removal can be envisioned to be due to both lateral outflow jetting within erosion pits and hydraulic penetration.

The need for a more precise analysis of these loading conditions and the associated fracture problems was pointed out in Section III.3.b to remove the uncertainties in the response of the target to water drop im-pact collisions have been initiated and are described. Additional work is required before the results from these analyses will become available, but the general approach and the type of problem which can be realistically addressed is clearly indicated.

1. CRACK/STRESS WAVE INTERACTION

A Green's tensor formulation will be developed for the propagation of a surface crack into an elastic half-space due to the stress waves generated in the half-space by a water drop collision. Eventually the propagation of stress waves in a region containing many cracks will be considered.

Our starting point is Eq. (5.46). We evaluate the surface integral over the combined surfaces of the half-space and the crack. Again assuming no sources and homogeneous initial conditions, we find,

$$u_j(\xi,t) = \oint_{S'} da_x \, t_{(n)i} *G_{ij} + \oint_C da_x \left[t_{(n)i} *G_{ij} - u_i *T_{(n)ij} \right] \quad (6.1)$$

where G_{ij} is the same Green's function used previously. With the exception of the crack opening, the first integral is identical to Eq. (5.49). Clearly, since the crack opening is small, Eq. (5.49) yields

$$u_j^{(o)} \equiv \oint_S da_x \, t_{(n)i} *G_{ij} \simeq u_j \quad (6.2)$$

except for a small region close to the crack opening. Since $T_{(n)ij}$ does not necessarily vanish on the crack boundary, we obtain an inhomogeneous integral equation for $u_i(\xi,t)$ when ξ is evaluated on the crack. We could, of course, simply require $T_{(n)ij}$ to vanish on all surfaces thereby reducing the problem formally to Eq. (5.49) with a new Green's tensor. This is not done, however, because the resulting problem for the new Green's tensor would be impractical to solve. The idea in this approach is to make the Green's tensor problem as complete as possible without rendering it insoluble. The stress wave propagation problem in Section 5 is complicated enough without introducing the crack. The remaining part of the problem is then treated, for this case, by solving an integral equation. While integral equations are not in general easy to solve in closed form, they are often amendable to approximation methods.

The surface stress on the crack boundary $t_{(n)i}$ will be determined by the details of a particular situation. The simplest case occurs when the crack is air-filled since then the required boundary conditions are $\sigma_{(n)i} = 0$. (In Cartesian coordinates, the physical stress matrix σ_{ij} and the stress tensor t_{ij} are identical.) More generally, if the crack is filled with water, then $\sigma_{(n)i}$ will equal the hydrodynamic stress.

In writing Eq.(6.1), no mention was made of the fact that the crack is not stationary. We must therefore determine the exact nature of the integral expressions in this equation. Recall that during the derivation of the Green's theorem, it was noted that the divergence theorem is valid for any closed surface. It follows that we can always choose the surface at any instant of time to coincide with combined surfaces of the half-space, S' , and the instantaneous surface of the crack.

The time dependence of the crack morphology only enters into the first integral of Eq.(6.1) through its dependence on S' and thus this term will only be affected when evaluated close to the crack opening. Close to the crack means within a distance on the order of the width of the crack. The second term is more complicated, however, due to the time dependence of the integrand introduced by the convolution.

Consider the first of these integrals,

$$I_{ij} = \oint_C da_x \, t_{(n)i} * G_{ij}$$

$$= \oint_C da_x \int_0^t d\tau \, t_{(n)i}(x,t-\tau) \, G_{ij}(x,\xi;\tau) \qquad (6.3)$$

At time $\tau=0$, $t_{(n)}(x,t-\tau) = t_{(n)}(x,t)$ which is the stress on the crack surface at time t . For $\tau>0$ however, $t_{(n)i}$ is evaluated in the interior of the material since at earlier times $t-\tau$, the crack is smaller and consequently the points specified by $x(t)$, the

integration surface at time t , lie not on the crack surface of time $t-\tau$, but in the interior of the material. Thus $t_{(n)i}(x,t-\tau)$ is not given by the boundary values on the crack surface, but must be determined from the dynamic solution at each instant of time as the solution progresses. It is clear that the required information is available at any time t to proceed with the calculation, although the need to re-compute the integrand at each instant would be tedious. Fortunately, we can simplify this result considerably when the crack width is small. The integration surface $C(t)$ is independent of τ and we can interchange the order of integration (dropping the tensor indices),

$$
\begin{aligned}
I_1 &= \oint_C da \int_0^t d\tau \, t_{(n)}(x,t-\tau) \, G(\tau) \\
&= \int_0^t d\tau \oint_C da \, t_{(n)}(x,t-\tau) \, G(\tau) \\
&= \int_0^t d\tau \left[\oint da^+ \, t_{(n)}(x^+,t-\tau) \, G(x^+,\tau) \right. \\
&\qquad \left. + \oint da^- t_{(n)}(x^-,t-\tau) \, G(x^-,\tau) \right]
\end{aligned}
\tag{6.4}
$$

where $(+)$ and $(-)$ denote the sides of the crack as indicated in Figure 28. Since the crack width is assumed small, at each x

$$
\hat{n}_+ \simeq -\hat{n}_-
\tag{6.5}
$$

and

$$
G(x^+,\tau) \simeq G(x^-,\tau) \; .
\tag{6.6}
$$

The latter follows from the fact that the Green's tensor is the solution to the problem without the crack and is thus continuous everywhere in the half-space.
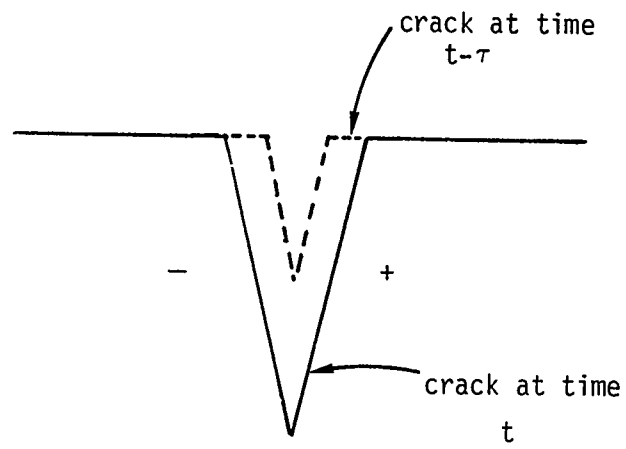
Figure 28. Schematic of the Variation of the Crack Boundary with Time.

Thus

$$I_{1j} \simeq \int_0^t d\tau \oint da^+ \, \hat{n}_k \left[t_{ik}(x^+, t-\tau) - t_{ik}(x^-, t-\tau) \right] G_{ij}(\tau) \quad (6.7)$$

Using the continuity of t_{ik} and G_{ij}, we now suppose that the surface of integration can be collapsed to the surface of the crack at time $t-\tau$ and a line extending from the location of the crack tip at time $t-\tau$ to the location of the crack tip at time t. The latter however vanishes by the continuity of t_{ik} and G_{ij}. These concepts are pictorially represented in Figure 29.

The integral $\oint da^+$ in Eq.(6.7) thus reduces to $\oint da^+(t-\tau)$ which denotes the integral over the crack surface C^+ at time $t-\tau$ and consequently $\Delta t_{ik} = t_{ik}(x^+) - t_{ik}(x^-)$ need only be evaluated on the crack surface. This is a considerable simplification since only the boundary values of t_{ik} are then involved in the calculation. A similar expression holds for the second integral in Eq.(6.1).

$$I_{2j} \simeq \int_0^t d\tau \oint da^+(t-\tau) \left[u_i(x^+, t-\tau) - u_i(x^-, t-\tau) \right] T_{ijk}(\tau) \, n_k \quad (6.8)$$

Along the crack surface, $u_i(x^+)$ and $u_i(x^-)$ generally have opposite signs so the integrand does not vanish. Thus if we know the Green's function, we obtain an integral equation for $u_i(\xi, t)$ which depends only on the values of $t_{(n)i}$ on the crack faces.

The approximation of small crack widths as used above can be examined by using the two-dimensional, plane strain solution for an edge crack in a semi-infinite plate subjected to mode I deformations. If r and θ are measured from the instantaneous crack tip, the displacements of the material point at the location (r, θ) are

$$u_x = 2(1+\nu) \frac{K_I}{E} \sqrt{\frac{r}{2\pi}} \cos\frac{\theta}{2} \left[1-2\nu+\sin^2\frac{\theta}{2} \right] \quad (6.9a)$$

$$u_y = 2(1+\nu) \frac{K_I}{E} \sqrt{\frac{r}{2\pi}} \sin\frac{\theta}{2} \left[2-2\nu-\cos^2\frac{\theta}{2} \right] \quad (6.9b)$$

116
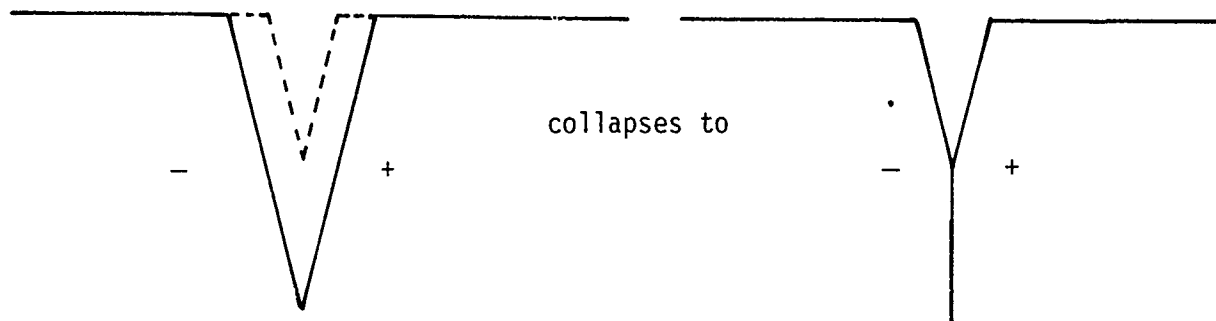
collapses to

Figure 29. Illustration of the Collapse of the Integration
Contour to Include just the Boundary of the Crack.

The location of the crack surface at time t, is determined by setting $r=\ell$ and $\theta=\pm\pi$ in Eq.(6.9). (Refer to Figure 30).

$$u'_x = 0$$
$$u'_y = \pm 4(1-\nu^2)\frac{K_I}{E}\sqrt{\frac{\ell}{2\pi}} \qquad (6.10)$$

With regard to the crack at time $t-\tau$, the displacements of the points located at the position of the integration surface at time t are found by substituting into Eq.(6.9) values of r' and θ' given by

$$r' = \sqrt{u'^2_y + (\eta-\ell)^2}$$
$$\theta' = \pm\tan^{-1}\left(\frac{u'_y}{\eta-\ell}\right) \qquad (6.11)$$

It will be useful at this point to introduce some numbers into these expressions. The stress intensity factor for this mode I stress condition is $K_I = 1.12\,\sigma\sqrt{\pi a}$ where a is the length of the crack (Paris and Sih, 1965). We chose as a representative value of stress the flexural strength of ZnS, σ_F=100.8 MPa. Young's modulus for this material is E=74.1 GPa and Poisson's ratio is 0.3. Thus Eq.(6.10) can be evaluated to yield

$$u'_y = \pm\, 3.9 \times 10^{-3}\sqrt{a'\ell} \qquad (6.12)$$

where a' is the length of the crack at time t. Then

$$\frac{u'_y}{\eta-\ell} = \pm\, 3.9 \times 10^{-3}\frac{\sqrt{a'\ell}}{\eta-\ell} \qquad (6.13)$$

and except for $\eta-\ell \leq 0(10^{-3})$,

$$\left|\frac{u'_y}{\eta-\ell}\right| \ll 1 \qquad (6.14)$$

118
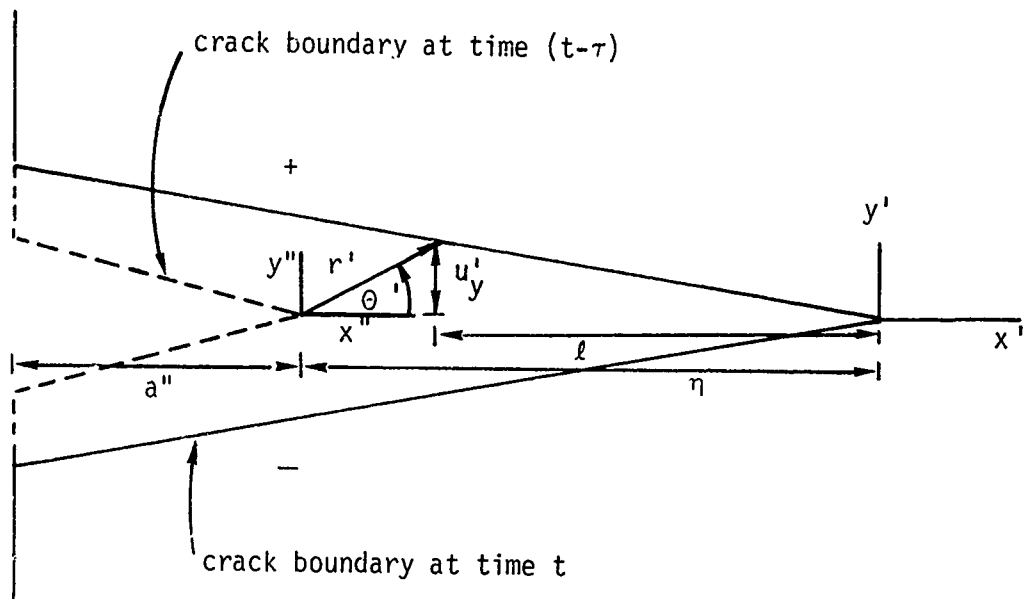
Figure 30. Coordinate System Used in Argument Justifying the Collapse of the Integration Contour to Include just the Crack Boundary.

119

The integrand in Eq.(6.8) is proportional to $\Delta u = u_i(x^+, t-\tau) - u_i(x^-, t-\tau)$. For $\theta' < \pi/2$, Eq.(6.9b) is evaluated as before with the assumption that θ is small, so using the previous material properties and formulae,

$$\Delta u \simeq \Delta u_y \simeq 5.6 \times 10^{-3} \sqrt{a''} \left(u_y'^2 + (\eta-\ell)^2 \right)^{1/4} \cdot \frac{1}{2} \left(\frac{u_y'}{\eta-\ell} \right) \left[2(1-\nu) - 1 \right]$$

$$\simeq 3.9 \times 10^{-6} \sqrt{\frac{a'a''\ell}{\eta-\ell}} \tag{6.15}$$

except for $\eta - \ell \leq 0(10^{-3})$. For $|\theta'| > \pi/2$,

$$\sin \frac{\theta'}{2} = \pm \left[1 - \frac{1}{4} \left(\frac{u_y'}{\eta-\ell} \right)^2 + \ldots \right] \simeq \pm 1 \tag{6.16}$$

and $\Delta u \simeq 5.6 \times 10^{-3} \sqrt{a''} \left(u_y'^2 + (\eta-\ell)^2 \right)^{1/4} \cdot 2(1-\nu) \simeq 7.8 \times 10^{-3} \sqrt{a''} \sqrt{\ell-\eta}$ (6.17)

Since T_{ijk} is continuous at the crack, the integration around the crack will be approximately given by

$$n_k T_{ijk} \int_0^{a'} d\ell \, \Delta u \tag{6.18}$$

Breaking the integral into the two regions, $\ell < \eta (= a' - a'')$ which corresponds to $\theta' < \pi/2$ and $\eta < \ell \leq a'$ $(\theta' > \pi/2)$, we find

$$I_< \equiv \int_0^\eta d\ell \, \Delta u = 6.2 \times 10^{-6} \, \eta \left[a'(a'-\eta) \right]^{1/2} \tag{6.19a}$$

$$I_> \equiv \int_\eta^{a'} d\ell \, \Delta u = 5.3 \times 10^{-3} (a'-\eta)^2 \tag{6.19b}$$

and thus except at $a' - \eta \lesssim 0(10^{-3})$ where $I_>$ vanishes because the crack vanishes,

$$\frac{I_<}{I_>} \sim 10^{-3} \ll 1 \tag{6.20}$$

120

The region very close to the crack tip where $|\eta-\ell| \lesssim O(10^{-3})$ must be re-examined but the general conclusion will not be changed. Consequently the surface of integration can safely be collapsed to enclose just the crack at time $t-\tau$ without introducing appreciable errors.

We now have a procedure then for calculating the stress and displacement distributions from the Green's function and the boundary stresses provided we know the morphology of the crack. The remaining steps are then to determine the Green's tensor and the relation between the dynamic field variables and the growth of the crack.

2. HYDRAULIC PENETRATION OF SURFACE CRACKS

Hydraulic penetration of existing surface cracks has been identified as a significant crack extension mechanism (Adler, 1979a) with characteristics distinct from those of the stress wave extension mechanism. One principal difference is in the direction of crack growth induced by these two mechanisms. It has been noticed for example that hydraulically activated cracks tend to undermine sections of the surface thus weakening large pieces of the surface which are subsequently removed. This behavior is strongly dependent on the characteristics of the material and thus the first step toward understanding and describing this process is to determine the relationship between the angle of crack extension and the other parameters of the problem such as the crack depth, inclination angle, and material properties. In general the analysis of this problem is quite complicated because of the hydrodynamics of the water flow in the crack and the interaction of the crack with impact induced stress waves. A much simpler, but relevant problem is analyzed here: namely, a two-dimensional static, pressurized surface crack of finite length, L , inclined to the surface at an arbitrary angle. The immediate goals of this study are to determine the

121

stress distribution surrounding the crack and, using one or more fracture model, to determine the initial angle of crack extension. Of particular interest is the effect of the proximity of the surface on the crack extension angle.

The stress distribution in two dimensions is most conveniently studied by introducing complex variables. As indicated in Figure 31, the material occupies the upper half plane. The location of a point in the material is specified by a complex number z given by

$$z = x + iy .$$ (6.21)

Complex conjugates will be denoted by a bar, e.g.,

$$\bar{z} = x - iy .$$ (6.22)

The equation of equilibrium becomes in complex notation

$$\frac{\partial^4 \chi(z,\bar{z})}{\partial^2 z \partial^2 \bar{z}} = 0$$ (6.23)

where $\chi(z,\bar{z})$ is the Airy stress function. The general solution of this equation is given in terms of two arbitrary functions $\phi(z)$ and $\psi(z)$ which are analytic in the region interior to the material boundary. In terms of these, the Airy stress function is

$$\chi(z,\bar{z}) = \text{Re}\left[\bar{z}\phi(z) + \int^z \psi(z)dz\right]$$ (6.24)
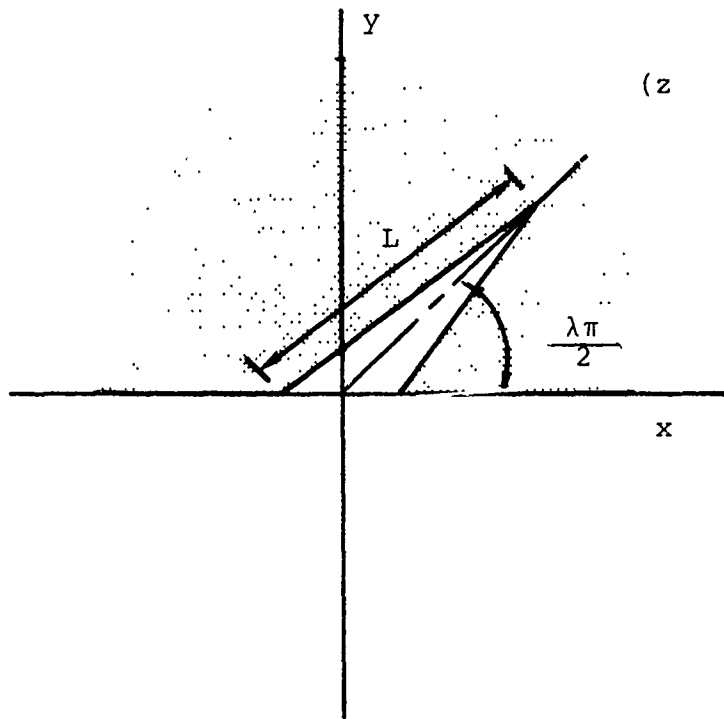
Figure 31.   Definition of Coordinates and Crack Angle
for Hydraulic Penetration Calculation.

The stresses are given by

$$\sigma_x + \sigma_y = 4 \, \mathrm{Re}\Phi(z) \qquad\qquad (6.25)$$

$$\sigma_y - \sigma_x + 2i\tau_{xy} = 2\left[\bar{z}\Phi'(z) + \Psi(z)\right] \qquad\qquad (6.26)$$

where

$$\Phi(z) \equiv \phi'(z) \qquad\qquad (6.27)$$

$$\Psi(z) \equiv \psi'(z) \qquad\qquad (6.28)$$

The boundary condition which determines these functions is

$$N(z) - iT(z) = \Phi(z) + \overline{\Phi(z)} - e^{2i\alpha}\left[\bar{z}\Phi'(z) + \Psi(z)\right] \qquad (6.29)$$

where $N(z)$ is the projection of the surface stress along $\hat{n}$, the outward unit normal vector, and $T(z)$ is the projection along the surface tangent pointing to the left of $\hat{n}$ when viewed from inside the material. The angle between $\hat{n}$ and the x- axis is denoted by α. Since we are considering hydrostatic forces,

$$N(z) = -P(z), \quad T(z) = 0 \qquad\qquad (6.30)$$

where $P(z)$ is the pressure which in general will depend on position.

We are thus confronted with the problem of finding two analytic functions which satisfy the boundary condition Eq.(6.29). Rather than approach this problem directly however, we will instead utilize a method introduced by Muskhelishvili (1953) who showed that by extending the definition of $\phi(z)$ into the lower half-plane, the function $\Psi(z)$ can be eliminated.

We define a function $\Phi(z)$ analytic in the lower half-plane by

$$\Phi(z) = -\bar{\Phi}(z) - z\bar{\Phi}'(z) - \bar{\Psi}(z) \qquad z \epsilon S^- \qquad (6.31)$$

Here the bar notation signifies

$$\bar{\Phi}(z) \equiv \overline{\Phi(\bar{z})} \qquad (6.32)$$

We now set $z \rightarrow \bar{z}$ and take the complex conjugate. Rearranging gives

$$\Psi(z) = -\Phi(z) - \bar{\Phi}(z) - z\Phi'(z) \qquad z \epsilon S^+ \qquad (6.33)$$

where now z is defined in the upper half-plane. Thus by extending the definition of $\Phi(z)$ into the lower half-plane, the function $\Psi(z)$ is determined in the upper half-plane. Introducing this result into Eq.(6.29) we obtain

$$N(z) - iT(z) = \Phi(z) + \overline{\Phi(z)} - e^{2i\alpha}\left[(\bar{z} - z)\Phi'(z) - \Phi(z) - \bar{\Phi}(z)\right] \qquad (6.34)$$

Consider now a region of the real axis for which N and T vanish. Since $\alpha = -\frac{\pi}{2}$ along this material surface, we have

$$0 = \Phi(z) + \overline{\Phi(z)} + (\bar{z} - z)\Phi'(z) - \Phi(z) - \bar{\Phi}(z) \qquad (6.35)$$

or

$$0 = \Phi(z) - \Phi(\bar{z}) + (z - \bar{z})\overline{\Phi'(z)} \qquad (6.36)$$

Since $z - \bar{z} = 0$ on the real axis, provided $\Phi'(z)$ is not too singular we obtain

$$\Phi(z) = \Phi(\bar{z}) \quad \text{at } z = \bar{z} \qquad (6.37)$$

This means that $\Phi(z)$ as extended by Eq. (6.31) is continuous across the real axis and it follows that $\Phi(z)$ is analytic everywhere in the plane, except perhaps on portions of the boundary where N and/or T are non-zero.

The asymptotic behavior of $\Phi(z)$ has been investigated by Muskhelishvili (1953) who showed that

$$\Phi(z) = \frac{-(X+iY)}{2\pi(1+\kappa)} \frac{1}{z} + \Gamma + \Phi_1(z) \tag{6.38}$$

$$\kappa = 3 - 4\nu$$

where Γ is related to the limit of the stresses as $z \to \infty$, $X+iY$ is the resultant of the surface stresses over the finite boundaries, and ν is Poisson's ratio. If the stresses vanish as $z \to \infty$, $\Gamma=0$ and if the surface stresses are self-equilibrating, then $X+iY=0$. The function $\Phi_1(z)$ is analytic everywhere except at the origin and vanishes as z^{-2} as $z \to \infty$. In order to simplify the calculations as much as possible, we will suppose that the pressure is self-equilibrating and further that the pressure vanishes everywhere on the real axis. Clearly by superposition, other more general solutions can be found by the addition of solutions for the cases in which this pressure is not zero.

Along the crack (see Figure 31), we have

$$e^{2i\alpha} = e^{2i\left(\frac{\lambda\pi}{2} + \frac{\pi}{2}\right)} = -e^{i\lambda\pi} \tag{6.39}$$

with the plus or minus sign depending on which side of the crack we are considering. Thus the boundary condition becomes

$$\Phi(z) \left(1-e^{i\pi\lambda}\right) + \overline{\Phi(z)} - e^{i\pi\lambda} \bar{\Phi}(z) + e^{i\pi\lambda}(\bar{z}-z)\Phi'(z) + P(z) = 0 \tag{6.40}$$

The boundary condition is not in a convenient form because the crack shape does not allow a simple power series expansion for $\Phi(z)$. To remedy this problem, we introduce a conformal mapping which maps the crack into a unit semicircle (Figure 31). The mapping which accomplishes this is (Bowie, 1973),

$$z = w(\zeta) = A \frac{1}{\zeta} (\zeta-1)^\lambda (\zeta+1)^{2-\lambda} \tag{6.41}$$

where

$$A = \frac{L}{2\lambda^{\frac{\lambda}{2}} (2-\lambda)^{1-\frac{\lambda}{2}}} \tag{6.42}$$

The angle θ_0 defined by

$$\theta_0 = \tan^{-1} \left(\frac{(2\lambda-\lambda^2)^{1/2}}{1-\lambda} \right) \tag{6.43}$$

determines the location of the crack tip on the unit circle in the ζ plane. It is easily shown that the positive and negative real axes in the z plane map into the corresponding real axes for $|\zeta|>1$ in the ζ plane. The crack maps into the unit semicircle in the ζ plane. Introducing the notation

$$\Phi(w(\zeta)) \equiv \Phi(\zeta) \tag{6.44}$$

$$\Phi'(z) = \frac{\Phi'(\zeta)}{w'(\zeta)} \tag{6.45}$$

the boundary condition becomes (on the unit circle $\zeta \equiv \sigma = e^{i\theta}$)

$$\Phi(\sigma) (1-e^{i\pi\lambda}) + \overline{\Phi(\sigma)} - e^{i\pi\lambda} \tilde{\Phi}(\sigma)$$

$$+ (1-e^{i\pi\lambda}) \frac{\sigma(\sigma^2-1)}{\sigma^2+2(\lambda-1)\sigma+1} \Phi'(\sigma) + P(\sigma) = 0 \quad 0 \le \theta \le \pi \tag{6.46}$$

127

(z

(ζ

$$\frac{\lambda \pi}{2}$$

θ

−1   1
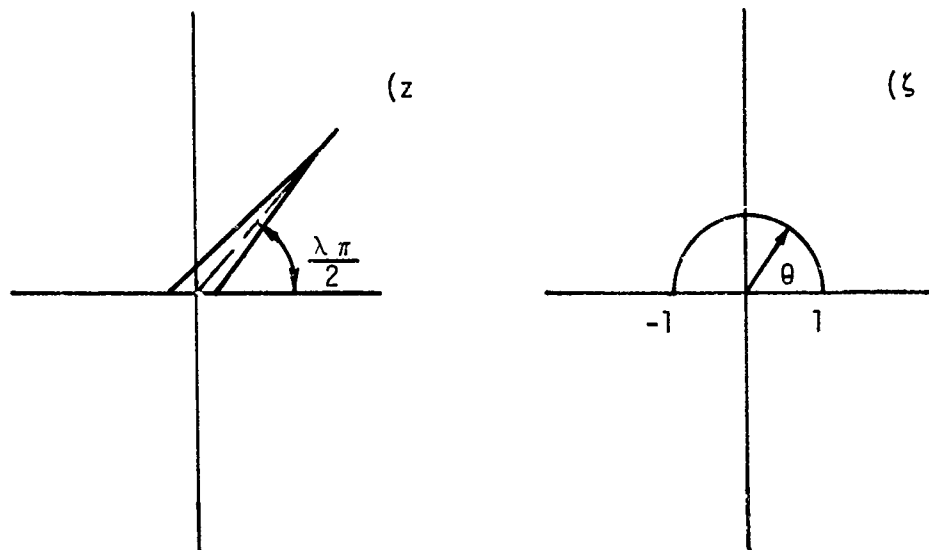
Figure 32.   Mapping of Crack onto Unit Circle.

The coefficient of $\Phi'(\sigma)$ has poles at

$$\sigma_{\pm} = 1-\lambda\underline{+}i\sqrt{2\lambda-\lambda^2} \tag{6.47}$$

By counting singularities, one finds that writing $\Phi(\zeta)$ in the form

$$\Phi(\zeta) = \frac{G(\zeta)\,\zeta^4}{(\zeta-\sigma_+)\,(\zeta-\sigma_-)^3} \tag{6.48}$$

defines a function $G(\zeta)$ which is analytic external to the unit circle and has no severe singularities on the unit circle. It follows that $G(\zeta)$ can be represented by a power series of the form

$$G(\zeta) = \sum_{k=2}^{\infty} A_k\,\zeta^{-k}\,. \tag{6.49}$$

The inversion of this expression gives

$$J_n \equiv \frac{1}{2\pi}\int_0^{2\pi} d\theta\, G(e^{i\theta})\, e^{in\theta} = \begin{cases} 0 & n \le 1 \\ A_n & n \ge 2 \end{cases} \tag{6.50}$$

This integral can be separated into two regions

$$J_n = \frac{1}{2\pi}\int_0^{\pi} d\theta\, G(e^{i\theta})\, e^{in\theta} + \frac{1}{2\pi}\int_{\pi}^{2\pi} d\theta\, G(e^{i\theta})\, e^{in\theta} \tag{6.51}$$

In the first of these, we introduce Eq. (6.49) to find

$$\frac{1}{2\pi}\int_0^{\pi} d\theta\, G(e^{i\theta})\, e^{in\theta} = \frac{A_n}{2} + \frac{1}{2\pi i}\sum_{\substack{k=2 \\ k\ne n}}^{\infty} A_k\left(\frac{(-1)^{n-k}-1}{n-k}\right) \tag{6.52}$$

129

In the second of these integrals, G , which is evaluated in the lower half-plane, is given by the boundary condition Eq.(6.46). If we define $\alpha = 2\pi - \theta$, we obtain

$$\frac{1}{\pi} \int_{\pi}^{2\pi} d\theta \ G(e^{i\theta}) \ e^{in\theta} = \frac{1}{\pi} \int_{0}^{\pi} d\alpha \ G(e^{-i\alpha}) \ e^{-in\alpha}$$

$$= \frac{1}{\pi} \int_{0}^{\pi} d\theta \ G(\overline{e^{i\theta}}) \ e^{-in\theta} \tag{6.53}$$

From the boundary condition, it follows after some algebra (recall $G(\bar{\sigma}) = \overline{G(\sigma)}$, $\bar{\sigma} = \frac{1}{\sigma}$,etc.)

$$G(\bar{\sigma}) = G(\sigma) \ F_1(\sigma) + \overline{G(\sigma)} \ F_2(\sigma) + \frac{\overline{G'(\sigma)}}{\sigma} \ F_3(\sigma) + P(\sigma) \ F_4(\sigma)$$

$$0 \le \theta \le \pi \tag{6.54}$$

where

$$F_1(\sigma) = \sigma^4 \sigma_-^2 \left(\frac{\sigma - \sigma_+}{\sigma - \sigma_-} \right)^2 e^{i\pi\lambda} \tag{6.55}$$

$$F_2(\sigma) = (e^{i\pi\lambda} - 1) \ \frac{\sigma_-^4}{(\sigma - \sigma_-)^2} \ \left[(\sigma - \sigma_+)^2 + \frac{\sigma(1 - \sigma^2)}{(\sigma - \sigma_-)^2} \ (4\sigma - 3\sigma_+ - \sigma_-) \right] \tag{6.56}$$

$$F_3(\sigma) = \frac{(e^{i\pi\lambda} - 1) \ (1 - \sigma^2)\sigma_-^4(\sigma - \sigma_+)}{(\sigma - \sigma_-)^3} \tag{6.57}$$

$$F_4(\sigma) = e^{i\pi\lambda}\sigma_-^2(\sigma - \sigma_+)^3 \ (\sigma - \sigma_-) \tag{6.58}$$

Substituting Eq.(6.49) into (6.54) and the result into (6.53) yields

$$\frac{1}{\pi} \int_0^\pi d\theta \; G(\bar{\sigma}) \; e^{-in\theta} = \sum_{k=2}^{\infty} \left\{ A_k I_1(k+n) + \bar{A}_k \left[I_2(k-n) - k I_3(k-n) \right] \right\} + I_4(n) \quad (6.59)$$

where

$$I_1(k+n) = \frac{1}{\pi} \int_0^\pi d\theta \; e^{-i(k+n)\theta} F_1(e^{i\theta}) \qquad (6.60)$$

$$I_2(k-n) = \frac{1}{\pi} \int_0^\pi d\theta \; e^{i(k-n)\theta} \; F_2(e^{i\theta}) \qquad (6.61)$$

$$I_3(k-n) = \frac{1}{\pi} \int_0^\pi d\theta \; e^{i(k-n)\theta} \; F_3(e^{i\theta}) \qquad (6.62)$$

$$I_4(n) = \frac{1}{\pi} \int_0^\pi d\theta \; P(e^{i\theta}) \; F_4(e^{i\theta}) \; e^{-in\theta} \qquad (6.63)$$

Combining Eqs.(6.50), (6.51), (6.52) and (6.59) yields an infinite set of nonhomogeneous linear simultaneous equations for the infinite number of complex coefficients A_n . Uniqueness of the solution is assured by the uniqueness of analytic functions for a given set of boundary conditions.

Since the complex coefficients A_n represent an infinite set governed by an infinite set of nonhomogeneous linear simultaneous equations, there is a degree of arbitrariness in the selection of a truncation procedure for determining the coefficients. The first attempt involved solving n complex equations, equally divided into the groups $n \geq 2$ and $n < 2$, for n complex coefficients A_k , k=2,3,...n+1 . It was found however that the coefficients so determined increased rapidly with increasing n and thus did not lead to a convergent expression for the function $G(\zeta)$ in Eq.(6.49). In order to inhibit this tendency,

131

additional equations were included so that n' equations $(n'>n)$ were solved for n coefficients in a least squares sense. For $\lambda \approx 1$, this procedure results in a rapidly converging sequence of coefficients when $n' \gtrsim 2n$, the accuracy of which was checked by comparing with the coefficients determined by Bowie (1973) for the case of a crack normal to the surface $\lambda = 1$. For λ much less than unity, on the other hand, some practical problems remain with this procedure because the number of coefficients required for convergence appears to grow as λ decreases and, as a consequence, the amount of computer time required becomes excessive. We have not yet exhaustively studied the possible variations within this class of algorithms and thus further work may yield a more efficient procedure which will reduce the amount of computer time required to obtain a solution. An alternate method for determining the stress near a crack tip has been discussed by Hussian, et al. (1974), for a related problem. This method, which is based on the solution of an integral equation in the limit as the crack tip is approached, will be discussed briefly below after some other aspects of this same paper which are relevant to the present problem are discussed.

Before doing so, however, we will derive the expressions which relate the stress intensity factors and the function $G(\zeta)$. For fracture Modes I and II, the stress near the crack tip is known to have the form

Mode I

$$\sigma_{x'} = \frac{K_I}{\sqrt{2\pi r}} \cos \frac{\theta}{2} \left(1 - \sin \frac{\theta}{2} \sin \frac{3\theta}{2} \right)$$

$$\sigma_{y'} = \frac{K_I}{\sqrt{2\pi r}} \cos \frac{\theta}{2} \left(1 + \sin \frac{\theta}{2} \sin \frac{3\theta}{2} \right) \qquad (6.64)$$

$$\tau_{x'y'} = \frac{K_I}{\sqrt{2\pi r}} \cos \frac{\theta}{2} \sin \frac{\theta}{2} \cos \frac{3\theta}{2}$$

Mode II

$$\sigma_x' = -\frac{K_{II}}{\sqrt{2\pi r}} \sin\frac{\theta}{2}\left(2 + \cos\frac{\theta}{2}\cos\frac{3\theta}{2}\right)$$

$$\sigma_{y'} = \frac{K_{II}}{\sqrt{2\pi r}} \sin\frac{\theta}{2}\cos\frac{\theta}{2}\cos\frac{3\theta}{2} \qquad (6.65)$$

$$\tau_{x'y'} = \frac{K_{II}}{\sqrt{2\pi r}} \cos\frac{\theta}{2}\left(1 - \sin\frac{\theta}{2}\sin\frac{3\theta}{2}\right)$$

where the parameters r, θ are defined in Figure 33. If we set $\theta=0$ and use Eqs. (6.25) and (6.26), we find

$$K_I = \lim_{r\to 0}\left[2\sqrt{2\pi r}\ \text{Re}\ \Phi(z)\right] \qquad (6.66)$$

$$K_{II} = \lim_{r\to 0}\left[-i\sqrt{2\pi r}\left(\bar{z}\ \Phi'(z) + \Phi(z)\right)e^{2i\alpha}\right] \qquad (6.67)$$

After some algebra, these reduce to

$$K_I + iK_{II} = \frac{\sqrt{\pi L}\ \sqrt{\lambda(2-\lambda)}}{4\sin^4\theta_o}\left(\text{Re}\left[i\ G(\sigma_+)\ \sigma_+^3\right] + i\ \text{Im}\left[i\ G(\sigma_+)\ \sigma_+^3\right]\right) \qquad (6.68)$$

which allows us to calculate the stress near the crack tip from $G(\sigma_+)$ or equivalently, the A_n's.

The next problem is to relate the stress near the crack tip to the growth of the crack. Many models have been proposed to describe the relation between stress and crack growth but most are too limited in scope to treat combined mode cracking. Two models which deal specifically with combined mode cracking are those of Sih (1973) and Hussain, et al. (1974). In Sih's model, the crack is assumed to extend in the direction of the maximum potential energy density where the potential energy density P is given by

$$P = -\frac{S}{r}\ . \qquad (6.69)$$

133
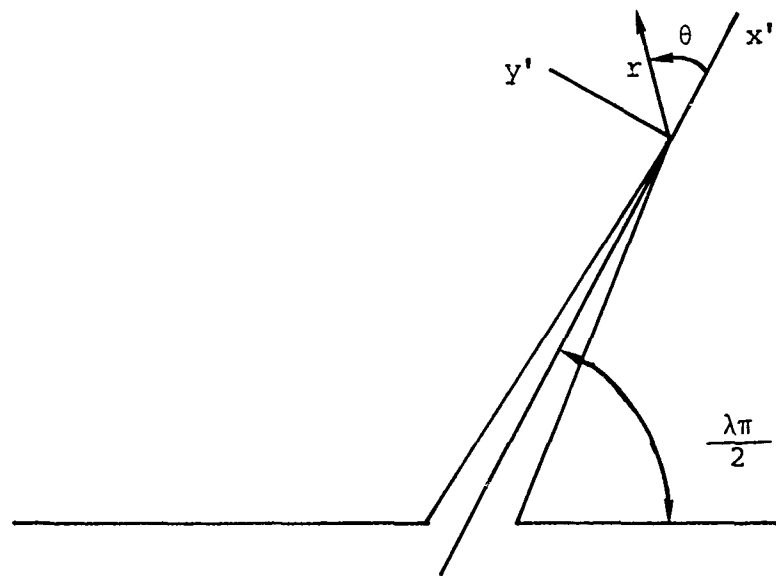
Figure 33. Definition of Parameters r,θ
and (x',y') Coordinate System.

$\dfrac{S}{r}$ is the elastic free energy in the limit as the crack tip approaches $(r \to 0)$

$$S = \lim_{r \to 0} \left\{ r\left(\frac{1}{2E}(\sigma_x^2 + \sigma_y^2 + \sigma_y^2) - \frac{\nu}{E}(\sigma_x\sigma_y + \sigma_x\sigma_z + \sigma_y\sigma_z)\right.\right.$$
$$\left.\left. + \frac{1}{2\mu}(\tau_{xy}^2 + \tau_{xz}^2 + \tau_{yz}^2)\right)\right\} \tag{6.70}$$

Since S is a quadratic function of the stress intensity factors at the crack tip, the direction of crack growth predicted by this model can easily be calculated once these factors are known. In fact, since

$$S = \frac{1}{16\mu}\left\{ (3-4\nu-\cos\theta)\ (1+\cos\theta)\ K_I^2\right.$$
$$+ \frac{1}{4\mu}\sin\theta\left(\cos\theta - (1-2\nu)\right)K_I K_{II} \tag{6.71}$$
$$\left. + \left(4(1-\nu)\ (1-\cos\theta) + (1+\cos\theta)\ (3\cos\theta-1)\right)K_{II}^2\right.$$

the condition that P be a maximum yields

$$\frac{\partial S}{\partial \theta} = 0 \ ; \ \frac{\partial^2 S}{\partial \theta^2} > 0 \tag{6.72}$$

or

$$\alpha_1 \sin 2\theta + \alpha_2 \cos 2\theta - \alpha_3 \sin\theta - \alpha_4 \cos\theta = 0 \tag{6.73}$$
$$2\alpha_1 \cos 2\theta - 2\alpha_2 \sin 2\theta - \alpha_3 \cos\theta + \alpha_4 \sin\theta > 0 \tag{6.74}$$

where

$$\alpha_1 = K_I^2 - 3K_{II}^2$$
$$\alpha_2 = 4K_I K_{II}$$
$$\alpha_3 = 2(1-2\nu)\ (K_I^2 - K_{II}^2) \tag{6.75}$$
$$\alpha_4 = 4(1-2\nu)\ K_I K_{II}$$

Thus given K_I and K_{II}, a crack extension angle can be determined. Crack extension is supposed to occur when S reaches a critical value characteristic of each material.

More recently, Hussain, et al. (1974), proposed a model for mixed mode crack extension. In some respects, it is similar to Sih's model although the crack extension criterion is stated in terms of the energy release rate given by the invariant J integrals rather than in terms of the elastic free energy. The important difference however is that Hussain, et al., treat the stress in the neighborhood of the crack tip as that for a deflected crack in the limit as the propagation branch of the crack shrinks to zero length. They found that the stress determined by this limiting procedure is dependent on the angle between the propagation and main branches of the crack. Consequently the energy release rate also depends on this angle and they argue that the crack will extend in the direction of maximum energy release. This extension criterion is more difficult to apply in general because a more complicated boundary value problem must be solved to determine the appropriate stress intensity factors.

The procedure used by Hussain, et al., is to convert the boundary value problem for the stress function into an integral equation. This step is useful because an exact solution can be found in the double limit as the propagation branch shrinks to zero length and the crack tip is approached. This yields sufficient information to calculate the stress intensity factors. It is felt that this technique might also prove useful for determining the stress intensity factors for the present problem. If this is indeed the case, then the convergence problems discussed earlier with regard to the series solution would be circumvented. Further work will be required to verify this supposition. We emphasize that the use of integral equation techniques is distinct from the concept of calculating the stress in the limit of zero propagation branch length. The deflected crack problem could also be solved using the series expansion techniques discussed earlier if the integral equation method proved to be too cumbersome. The remaining question is to determine which, if either, of these models is correct and this can only be done by comparison with experiment.

SECTION VII

TRANSMISSION LOSSES DUE TO CRACKS

It is intuitively obvious that optical degradation will occur when the surface of an infrared-transmitting window becomes pitted on the scale of the diameter of a typical rain drop since then the transmitted infrared radiation with a wavelength λ on the order of 1 to 10 μm will be scattered in various directions vis a vis Snell's law. This is particularly true for materials such as zinc sulfide and zinc selenide which have rather large indices of refraction. At $\lambda=3.3$ μm, $n_{ZnS}=2.3$; and for $\lambda=8$-13 μm, $n_{ZnSe}=2.4$. A more important observation with regard to the subsurface fractures described in Section 4, however, is that significant degradation occurs before there is a measurable mass loss from the surface. This indicates the importance of light scattering by the internal fracture surfaces which develop due to single and multiple water drop collisions.

It is easy to understand the origin of the transmission degradation by considering the optical properties of an idealized crack as indicated in Figure 34. The crack faces are taken to be parallel in order to avoid unnecessary complication in the elementary analysis which follows. Whenever electromagnetic radiation is incident on an interface between two regions with differing indices of refraction, generally both transmitted and reflected waves result, Figure 35a. If the index of refraction of the second medium, n_2, is less than that of the first, n_1, then a critical angle of incidence α_c exists such that the reflection is total for angles of incidence $\alpha > \alpha_c$, Figure 35b.

This angle is given by

$$\sin\alpha_c = \frac{n_2}{n_1} \tag{7.1}$$

For the interface between zinc sulfide and air and water, respectively, this angle has the values

137
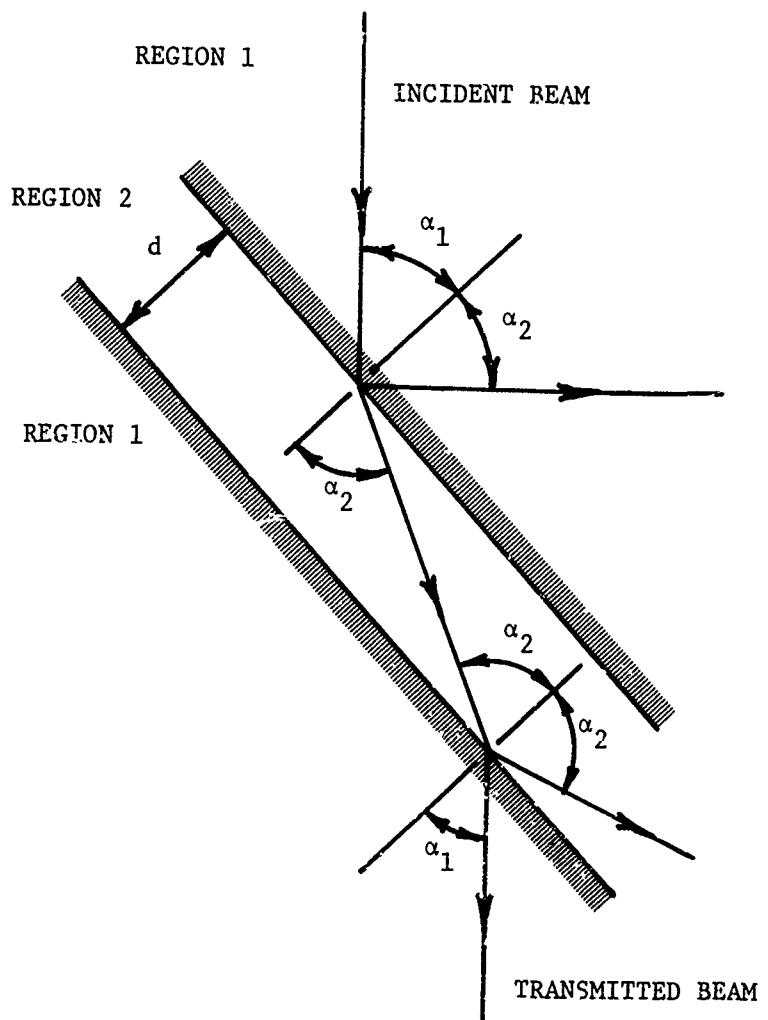
Figure 34. Geometrical Relations for the Transmission of
Radiation Across an Idealized Crack.

a) $n_1 > n_2$

$\alpha < \alpha_c$

b) $n_1 > n_2$

$\alpha > \alpha_c$
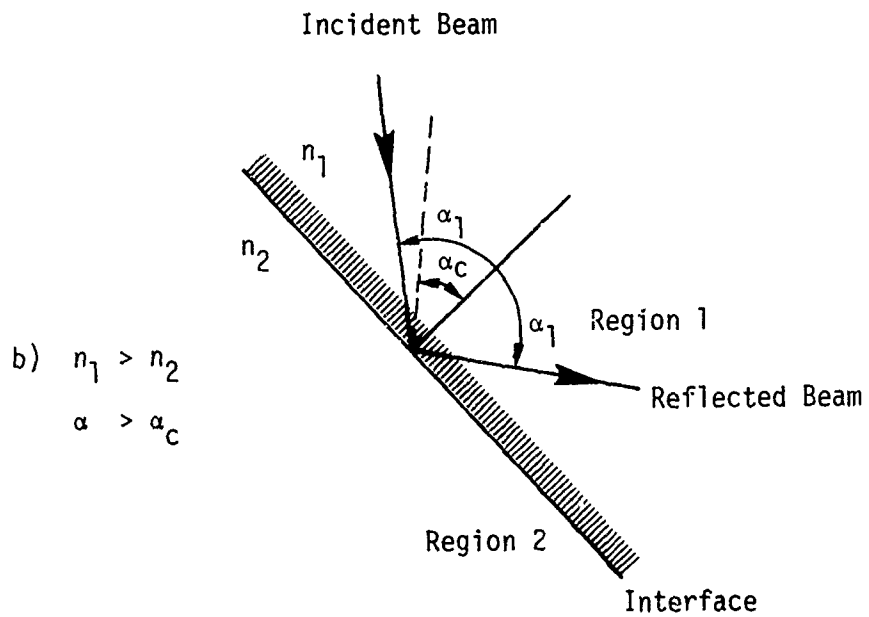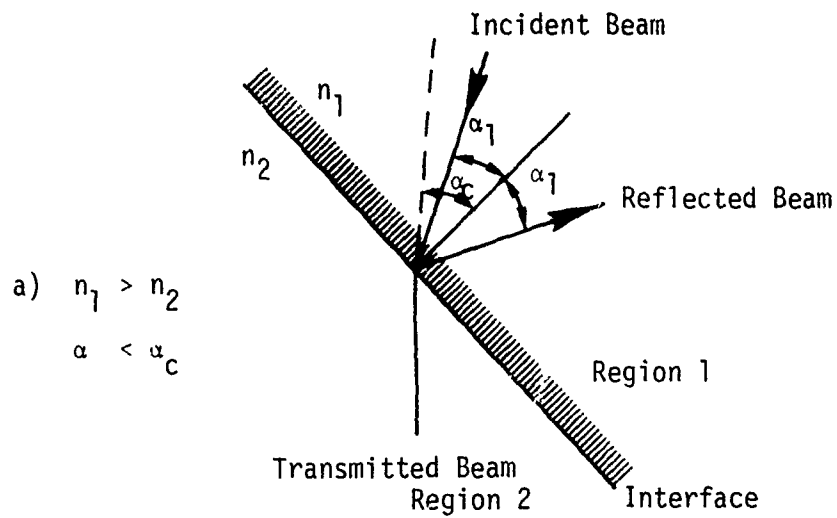
Figure 35. Transmission of Electromagnetic Radiation at the Interface between Two Media.

$$\alpha_c = \begin{cases} 25.8° & \text{ZnS - air} \\ \\ 34.4° & \text{ZnS - water} \end{cases} \tag{7.2}$$

For the case of a crack which has two interfaces, the situation is more complicated because transmission can occur for angles greater than α_c by a process analogous to quantum mechanical tunneling, provided the crack width d is not too large. For the electromagnetic field does not vanish instantaneously at the interface in Figure 35b under conditions of total internal reflection, but instead attenuates exponentially according to

$$e^{-k_2 Z \left[\left(\frac{\sin\alpha}{\sin\alpha_c} \right)^2 - 1 \right]^{1/2}} \qquad \alpha > \alpha_c \tag{7.3}$$

where Z is the distance normal to the interface in region 2 and $k_2 = \frac{2\pi}{\lambda_2}$ is the wave number in region 2. It is easily shown that even though the field is nonzero in region 2, no energy is propagated in the Z-direction by this field. If, however, a second interface is placed close to the first in the region where the field is nonzero, then energy can flow across the gap and some transmission will occur. The transmission coefficient, T, defined to be the ratio of the transmitted energy to the incident energy, for the crack is determined by solving the boundary value problem for the geometry shown in Figure 34. For unpolarized light, the transmission coefficient is

$$T = 1/2 \left(|\zeta_\perp|^2 + |\zeta_{||}|^2 \right) \tag{7.4}$$

140

where for $\alpha < \alpha_c$,

$$|\zeta_\perp|^2 = \frac{1}{\cos^2\gamma + 1/4\left(\dfrac{\cos\alpha_1}{\cos\alpha_2\sin\alpha_c} + \dfrac{\cos\alpha_2\sin\alpha_c}{\cos\alpha_1}\right)^2 \sin^2\gamma} \tag{7.5a}$$

$$|\zeta_{||}|^2 = \frac{1}{\cos^2\gamma + 1/4\left(\dfrac{\cos\alpha_1\sin\alpha_c}{\cos\alpha_2} + \dfrac{\cos\alpha_2}{\cos\alpha_1\sin\alpha_c}\right)^2 \sin^2\gamma} \tag{7.5b}$$

$$\gamma = k_2 d \cos\alpha_2 \tag{7.5c}$$

and for $\alpha > \alpha_c$

$$|\zeta_\perp|^2 = \frac{1}{\cosh^2\Gamma + 1/4\left(\dfrac{\cos\alpha_1}{q\sin\alpha_c} - \dfrac{q\sin\alpha_c}{\cos\alpha_1}\right)^2 \sinh^2\Gamma} \tag{7.6a}$$

$$|\zeta_{||}|^2 = \frac{1}{\cosh^2\Gamma + 1/4\left(\dfrac{\cos\alpha_1\sin\alpha_c}{q} - \dfrac{q}{\cos\alpha_1\sin\alpha_c}\right)^2 \sinh^2\Gamma} \tag{7.6b}$$

$$q = \left[\left(\frac{\sin\alpha}{\sin\alpha_c}\right)^2 - 1\right]^{1/2} \tag{7.6c}$$

$$\Gamma = k_2 d \, q \tag{7.6d}$$

141

The subscripts $\perp$ and $||$ refer to polarization of the electric field perpendicular and parallel to the plane of incidence. These expressions include the effects of multiple reflections in the crack. Notice that since $|\zeta_\perp| \neq |\zeta_{||}|$, the transmitted light will in general be partially polarized.

Some representative evaluations of Eq.(7.4) are provided in Figures 36 to 39 . Figure 36 shows the dependence of T on α for fixed values of the ratio d/λ . λ refers to the wavelength in air. For values of $d/\lambda \gtrsim 1$, essentially no transmission occurs for $\alpha > \alpha_c$ as expected. The rapid fluctuations in T for $\alpha < \alpha_c$ are due to the constructive and destructive interference of the primary and reflected waves emerging from the crack. For small values of d/λ , on the other hand, significant transmission can occur for $\alpha > \alpha_c$. Figures 37 and 38 show the dependence of T on d/λ for fixed angle. Figure 38 shows the results from Figure 37 on an expanded scale. It is seen that for $\alpha < \alpha_c$, T oscillates indefinitely as a function of d/λ in response to the interference effects mentioned above never dropping below about .55; but for $\alpha > \alpha_c$, T decays rapidly to zero as d/λ is increased. Notice also that T approaches unity for all angles if d/λ is sufficiently small which would be the case if the crack were to close after its formation.

The results in Figures 36 to 38 were calculated assuming the crack to be filled with air. For comparison, the analogous results for water filled cracks are shown in Figure 39 . For ease of comparison, the dependence of T on d/λ for air when $\alpha_1 = 50°$ is also plotted in Figure 39. It is apparent that the transmission coefficient is enhanced by the water which is expected since increasing α_c decreases the attenuation coefficient Γ , Eq.(7.6d). This shows incidently that improved transmission will be obtained for a given crack width by decreasing the index of refraction of the material.
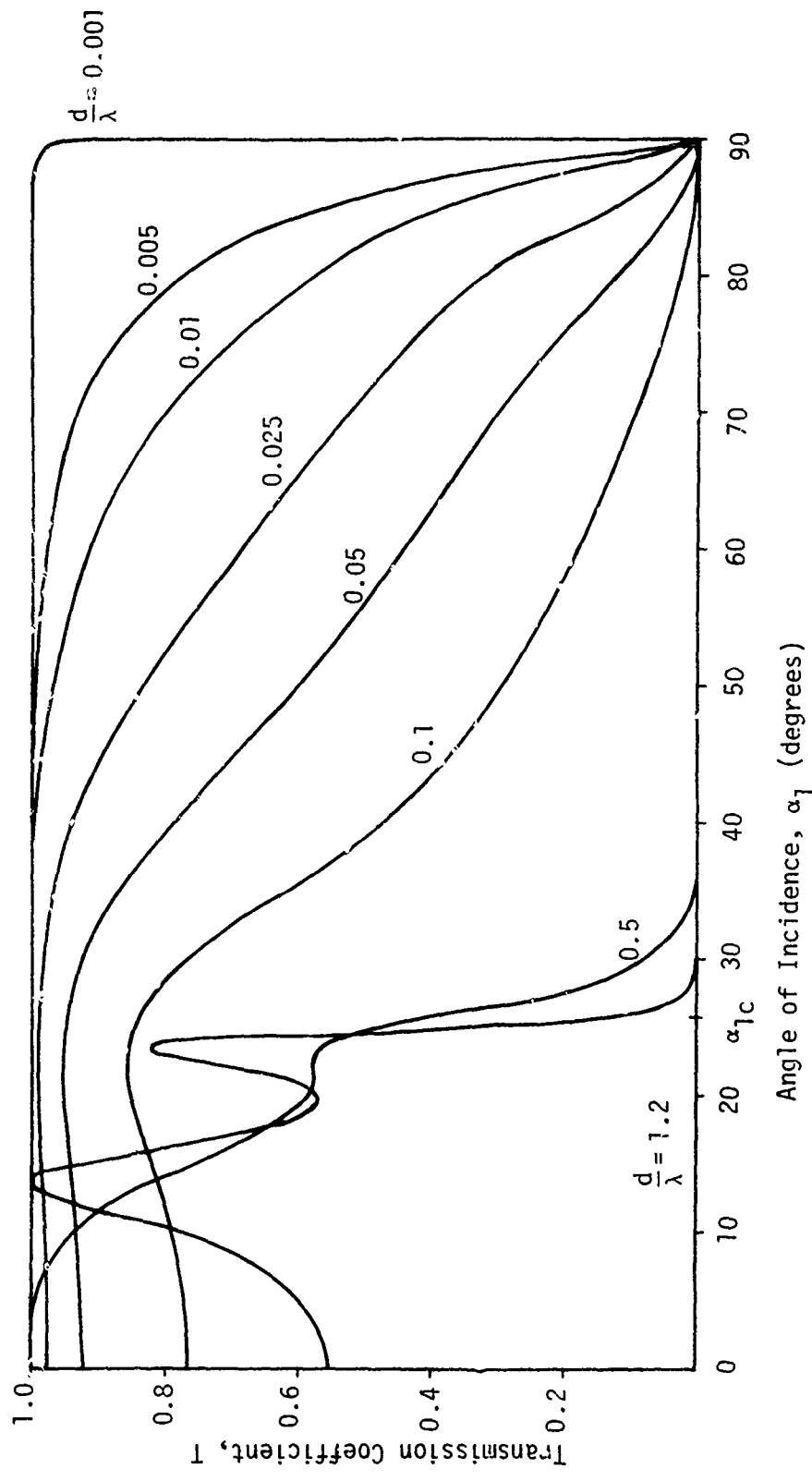
Figure 36.   Transmission Across an Air-filled Inclined Gap in Zinc Sulfide as a Function of Angle of Incidence
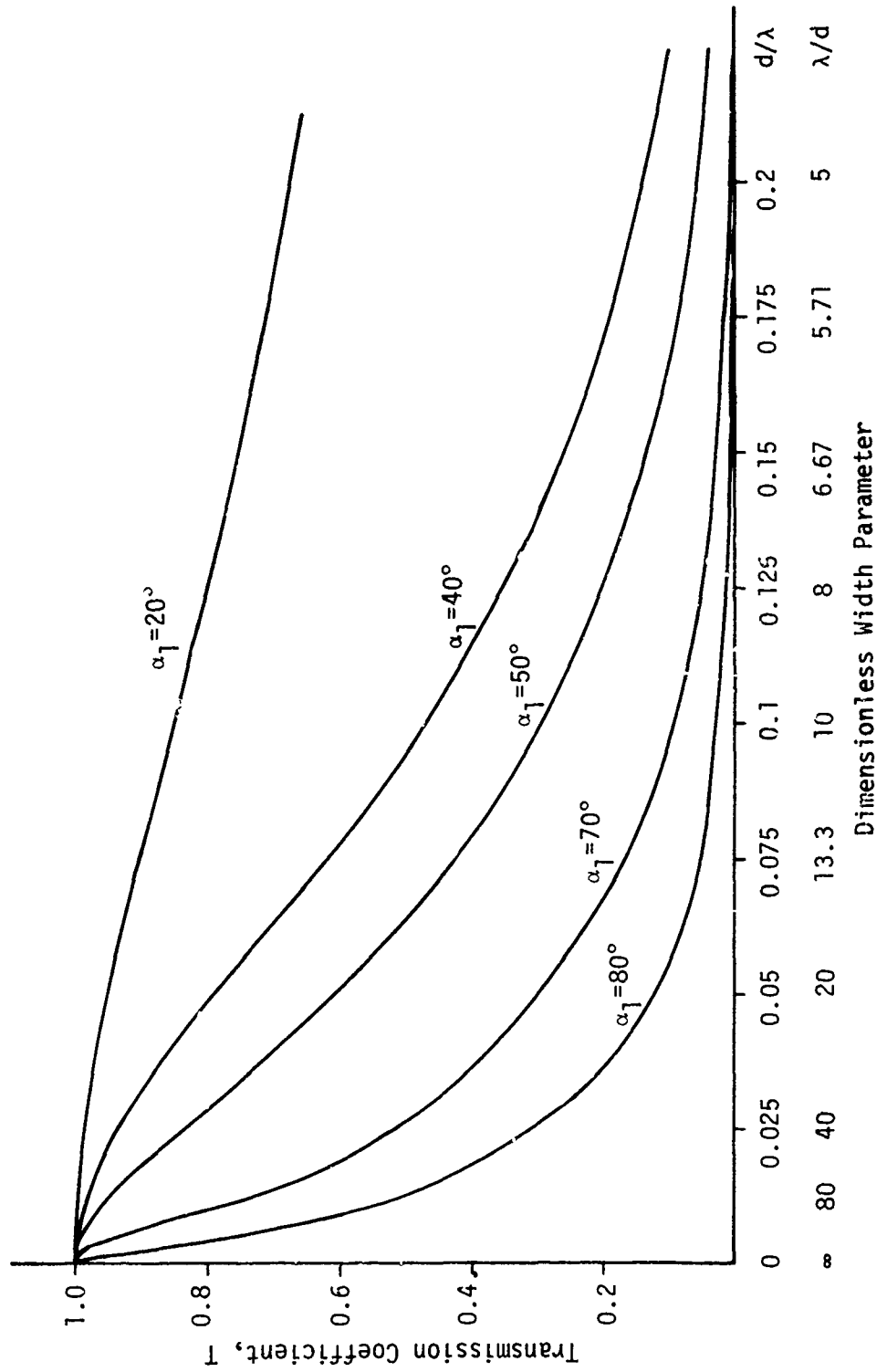
Figure 37. Transmission Across an Air-filled Inclined Gap in Zinc Sulfide as a Function of Gap Width

144
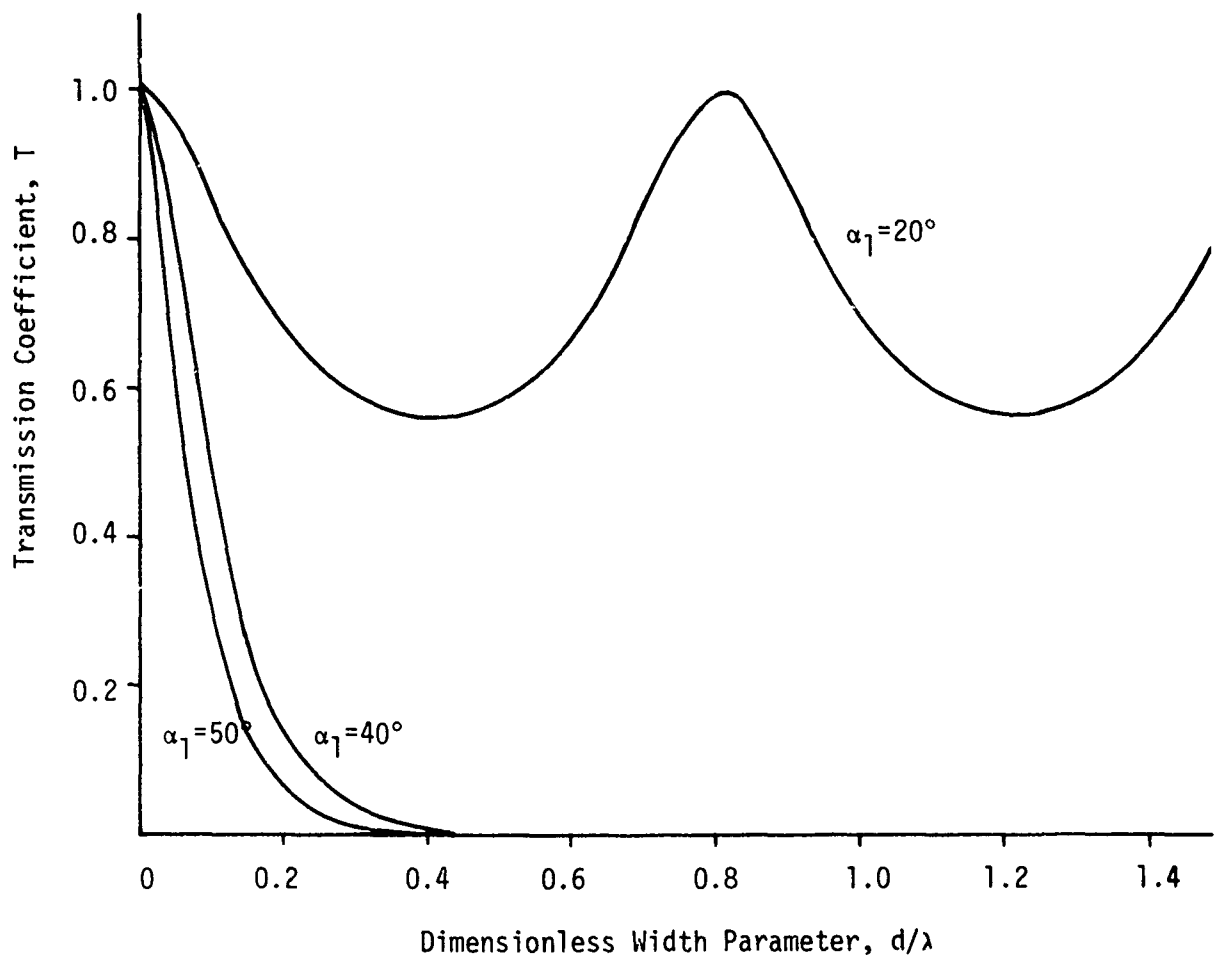
Figure 38. Transmission Across an Air-filled Inclined Gap
in Zinc Sulfide as a Function of Gap Width
(expanded scale)
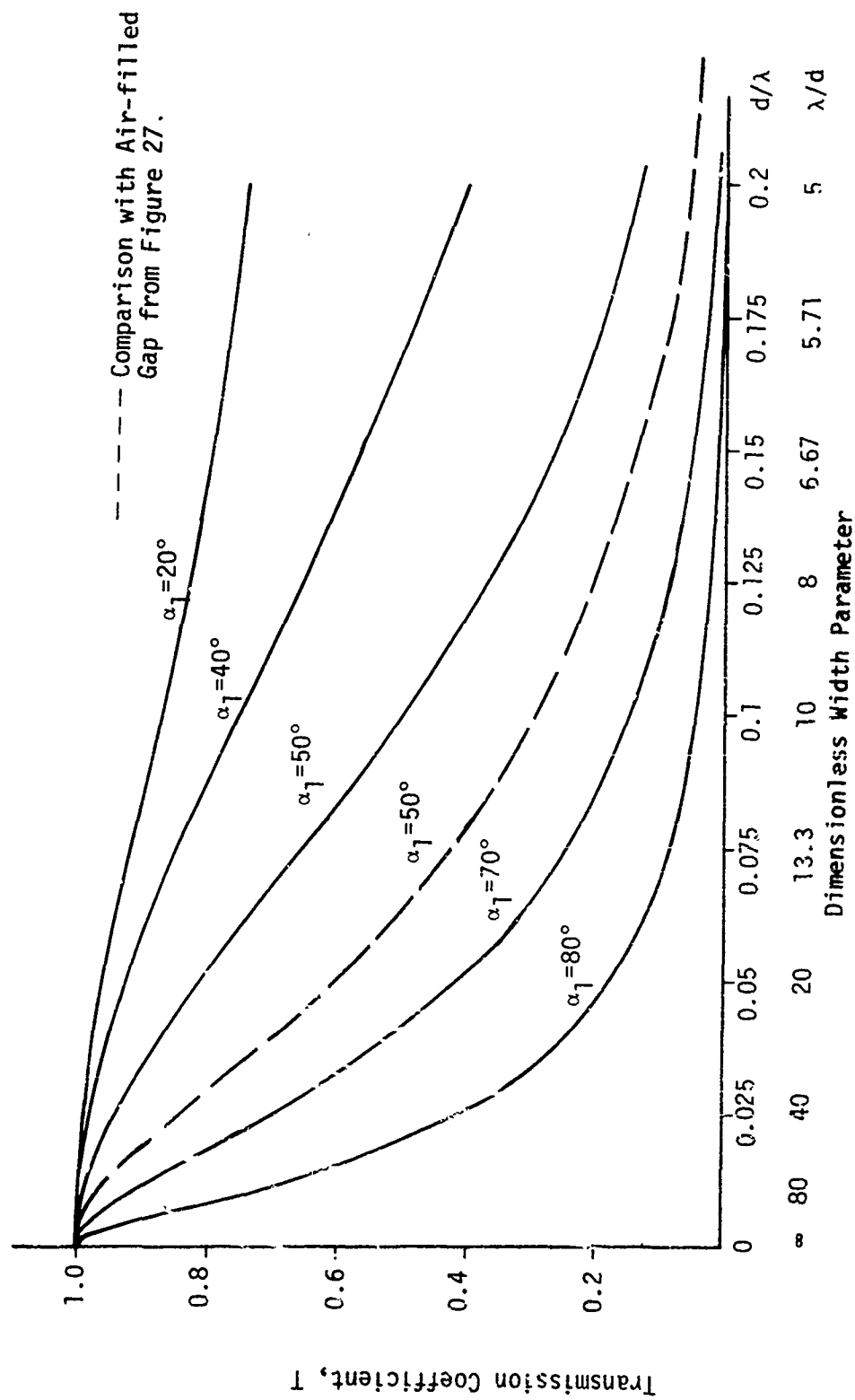
Figure 39. Transmission Across a Water-filled Inclined Gap in Zinc Sulfide as a Function of Gap Width.

146

To relate these results to the net transmission of a window, it is necessary to consider the length of the crack. This will eliminate the apparent anomaly of zero transmission at $\alpha_1 = 90°$, since then the projected area of the crack is also zero and the crack does not cause a loss of transmission.

The calculations presented here do not yet include the effects of attenuation in the material and reflections at the window surfaces. Since these later effects are multiplicative, the influence on radiation transmission of the cracks developed during water drop impacts can be adequately addressed without treating these other effects in detail.

If the incident radiation is normal to the window surface, a simple expression is obtained for the time dependent loss of transmission due to crack formation. Denoting the incident and transmitted energy per unit area per unit time by ε_i and ε_T , respectively, a transmission coefficient T_o is defined for an uncracked window by

$$\varepsilon_T = T_o \varepsilon_i \tag{7.7}$$

T_o includes the effects of reflection at the window surfaces and energy absorption by the window material. When cracks are present, the total energy transmitted will be the sum of that transmitted by the uncracked and cracked regions. Thus,

$$\varepsilon_T A_o = \varepsilon_i T_o \left(A_o - \sum_n A_n \right) + \sum_n \varepsilon_{Tn} A_n \tag{7.8}$$

where A_o is the total surface area of the window, A_n is the area projected onto the window surface of the nth crack at time t , and ε_{Tn} is the energy transmitted through this area. ε_{Tn} will include the attenuation effects of T_o in addition to that of the crack and it follows that

$$\varepsilon_{Tn} \cong \varepsilon_i T_o T_n \tag{7.9}$$

where T_n is the transmission coefficient for the nth crack. Introducing the definition in Eq.(7.9) into Eq.(7.8),

$$\varepsilon_T A_o = \varepsilon_i T_o \left[A_o - \sum_n A_n \left(1 - T_n \right) \right] \tag{7.10}$$

We have assumed that cracks do not overlap. If they do, the total crack attenuation is found by substituting for T_n the appropriate products of transmission coefficients for the particular cracks involved. The time-dependent transmission coefficient due to crack generation is determined from Eq.(7.10),

$$T(t) = \frac{\varepsilon_T A_o}{\varepsilon_i A_o} = T_o \left[1 - \frac{1}{A_o} \sum_n A_n (1 - T_n) \right] \tag{7.11}$$

In order to proceed further, we need an estimate of the average crack inclination angle. Experimental studies show that the majority of the crack surfaces are inclined to the surface at angles greater than 45° except for those in fracture zone 2. A representative angle of $\alpha_1 = 55°$, an angle which is much greater than α_c for either air- or water-filled cracks will be selected for the purpose of considering an explicit example. Referring to Figure 38, we see that such cracks will be almost totally opaque for $d/\lambda \gtrsim 0.3$. Suppose for simplicity that all the cracks are formed at the same angle with the same projected area and are created at a constant rate of N cracks per unit time, then the transmission coefficient for the window, Eq.(7.11), reduces to

$$T(t) = T_o \left[1 - \frac{t}{t_o} (1 - T_c) \right] \tag{7.12}$$

where $t_o = \left[N \left(\frac{A_c}{A_o} \right) \right]^{-1}$ is the time required to completely obscure the surface.

A_c is the projected area of a single crack,

T_c is the transmission coefficient for a single crack.

The implications of this result are that no incubation period is required before degradation begins and that the transmission loss will increase linearly with exposure time. The expression in Eq.(7.12) is valid only for times small relative to t_o .

Figure 40 shows the degradation of transmission for $\alpha_1 = 55°$ for several values of d/λ . It is apparent from this figure that the value of d/λ has a significant effect on the rate of degradation. The line labeled $(T_c = 0)$ is the limiting line for the case of completely opaque cracks which is reached for $d/\lambda \gtrsim .3$ (see Figure 38) . Thus, for example, for a crack width of $d = .2$ µm , the crack would be essentially opaque for wavelengths of $\lambda \simeq 1$µm and nearly transparent for $\lambda \simeq 20$µm. Behavior of this sort has been observed by Hackworth and co-workers (Hackworth and Kocher, 1977; Hackworth, et al., 1979). According to their work, the infrared transmittance of zinc sulfide decreased almost linearly with incremental exposure to the standard rainfield in the AFML/Bell rotating arm erosion facility for wavelengths in the range 0.5 to 2.1 µm. However they indicate that there is a definite incubation period associated with the development of surface pitting for the degradation of transmittance in the range of 2.5 to 25 µm. Once erosion pits are nucleated the rate of transmittance loss was approximately proportional to the growth rate of the total cross-sectional area of the pits. Hackworth and co-workers speculate that the same relations apply to zinc selenide and gallium arsenide, however the rate of material removal was too great for exposures to the standard rainfield to experimentally confirm this conjecture.

Obviously this model is oversimplified since many effects such as nonparallel crack surfaces and overlapping cracks were not considered. It is expected however that a more complete model which includes these and other effects and the statistical nature of the particle field would yield a similar result for the transmission coefficient.
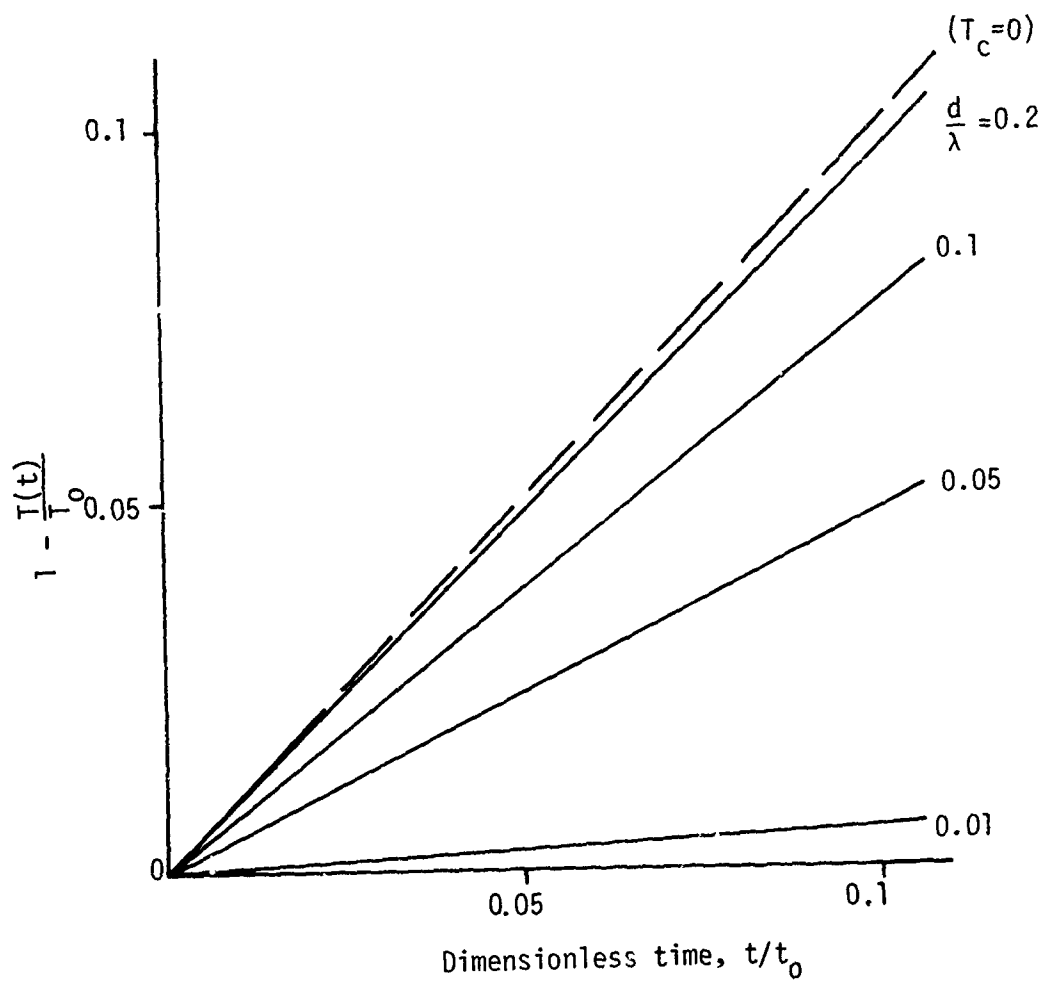
Figure 40. Time-dependence of the Transmission Losses in Zinc Sulfide due to Idealized Crack Growth in Air When the Angle of Incidence is 55°.

SECTION VIII

DISCUSSION

The objective of this effort was to determine the relationships between water drop impact damage and the material properties of infrared-transparent materials in order to evaluate and guide the development of erosion resistant window materials. A combined experimental and analytical approach was undertaken to determine and describe primarily the water drop impact response of CVD zinc sulfide, however the results of this program are of more general utility.

The impact damage mechanisms were investigated for water drop impacts at velocities from 222 to 684 ms^{-1} (730 to 2240 fps) with the major emphasis on the velocity range from 342 to 512 ms^{-1}. Both experimental and computational procedures were utilized to relate the dominant damage modes to the material's surface condition, microstructure, and bulk properties. The most productive analysis for evaluating the bulk response of the material to the water drop impact loading involves continuum representations of the target material.

The complete description of the impact process entails the solution of a coupled problem including the deformations of both the incident particle and the target material. At the relatively low velocities of interest and for highly deformable particles the problem can be uncoupled as a first approximation. The effect of the incident particle can then be treated as a known temporally and spatially dependent pressure distribution on the undeformed surface of the target material. This pressure distribution has been determined using finite difference procedures and experimentally for water drop impact simulations as reviewed by Adler (1979a). The analytical representation of the surface pressure distribution developed by Rosenblatt, et al. (1977) with minor modifications will be adequate for the initial implementation of the computational program which will be an outgrowth of the completed analysis described in Section V. The reasons for undertaking this analysis are outlined in Section V.1. While the scope of this analysis is

151

beyond the original intent of this program, the approach adopted affords a broader range of generalization than would otherwise be possible and is the basis for describing crack growth due to surface flaw interactions with the dynamic stress field (Section VI.1).

The solution to the general problem of an elastic half-space subjected to an arbitrary pressure distribution on its surface will provide the transient stress states within the half-space. The only material properties included in this analysis are the density, Young's modulus, and Poisson's ratio for the target material which enter the solution through the characteristic wave velocities for the material. The approach taken is to determine the Green's tensor for the elastic half-space. The transient stress states are then found in terms of a surface integral of the convolution of the pressure distribution and the Green's tensor. The formal problem of determining the Green's tensor has been solved and has been reduced to evaluating several definite integrals as described in Section V.4. In some cases singularities occur in these integrals which have been treated analytically to preserve the accuracy of the results. The singularities are understood and isolated so the resulting integrals can be evaluated numerically with a high degree of accuracy. The solution is essentially complete; it now has to be programed for digital computer evaluation.

The alternative method for determining the stress waves is the completely numerical finite element approach. We have avoided using these methods because of the large expense and the fact that these methods do not give a very detailed picture of the stress waves unless a very small grid size is used. One is then beset with problems resulting from the disparity in the size of the regions important for stress wave propagation and the size of the crack tip.

Within a continuum context the fracture problems to be addressed involve introduction of the fracture toughness and the distribution of critical flaw sizes for the target material. For purely elastic material response conditions the fracture toughness, K_{IC}, is considered to be a

material constant, and as such is used to define the critical stress intensity factor for a wide variety of crack configurations and loading conditions. The fracture problems identified as being most significant in relation to the water drop impact damage produced in CVD zinc sulfide are the stress wave/surface flaw interactions and hydraulic penetration of preexisting surface cracks. It was originally thought that the stress wave/microstructure interactions would be much more significant than the experimental results indicate. The general observation from the experimental data is that the fractures produced during water drop collisions on CVD ZnS are essentially insensitive to the material's general microstructure and inclusion content over a representative range of grain size variations.

Stress wave/surface flaw interactions will be the first step in utilizing the available fracture data in a model. This model will also be considered in terms of the experimental data obtained for water drop impacts on CVD zinc sulfide. Some simple examples of how this data can provide useful estimates of the fracture response of CVD ZnS will be described.

The critical stress intensity factor (fracture toughness) for CVD ZnS has been determined by Evans (data referred in Evans and Wilshaw, 1976), Wimmer and Graves (1977), and Shockey, et al. (1977). Evans found $K_{IC} = 1$ MPa m$^{1/2}$ for a material with an average grain size of 10 μm with essentially equiaxed grains (Evans, 1979).[*] According to Wimmer and Graves, $K_{1C} = 0.67$ MPa m$^{1/2}$. This value was determined for the baseline material for this investigation, material A, using a four-point bend test. Wimmer and Graves' grain size measurements showed that the material had columnar grains with a cross sectional diameter of 8 to 10 μm and a length up to 60 μm in the growth direction. They also determined that the bend strength was 100.8 MPa. Shockey, et al., found $K_{IC} = 0.75$ MPa m$^{1/2}$ based on four tests using a modified expanded ring test technique. The material used by Shockey, et al., was composed of columnar grains with average cross sectional diameters of 7 μm and lengths of approximately 56 μm.

---

[*] The grain size was reported to be 30 μm in Evans and Wilshaw (1976), however in a recent communication with Dr. Evans (Evans, 1979) the grain size was restated as being 10 μm and equiaxed grains. Representatives from Raytheon Corp. do not recall producing equiaxed grain material and have only been able to achieve a minimum average aspect ratio of about 3 with the CVD process.

There are two crack geometries which are relevant to the water drop impact conditions: an edge crack in a plate and a semicircular crack in a half-space as illustrated in Figure 41. The stress intensity factors for each of these cases when the cracks are subjected to an uniaxial stress, σ, are

$$K_I = 1.12 \sigma \sqrt{a\pi} \qquad (8.1)$$

[Paris and Sih, 1965] and

$$K_I = C \frac{2\sigma}{\pi} \sqrt{a\pi} \qquad (8.2)$$

[Smith, et al., 1967] where $C = 1.03$ when $\theta = 0°$ and $C = 1.21$ when $\theta = 90°$ (refer to Figure 41).

We note in passing that Shockey and co-workers (1977) incorrectly evaluated Eq.(8.2) using their value of K_{IC}. They equated σ to the flexural strength of 110 MPa and computed the magnitude of the critical flaw size which they define as $a_c^* = 2 a_c$ where a_c is the value corresponding to Eq.(8.2). Shockey, et al., find that $a_c^* = 0.73$ mm. However they made an arithmetic error; the value of a_c^* should be 0.073 mm. Furthermore if the critical flaw size is properly interpreted, then a_c (the depth of the flaw as shown in Figure 41b) is 36 μm. This result indicates the critical flaw size is approximately five times the cross sectional diameter of the average grain in contrast to the value determined by Shockey and co-workers which is 100 times this dimension.

The relations in Eq.(8.1) and (8.2) can also be used in conjunction with the transient stress states due to particulate collisions. Since our evaluation of the transient stresses is not yet operational for digital computations, some of the published results will be used as approximations to the stresses imposed on the crack.
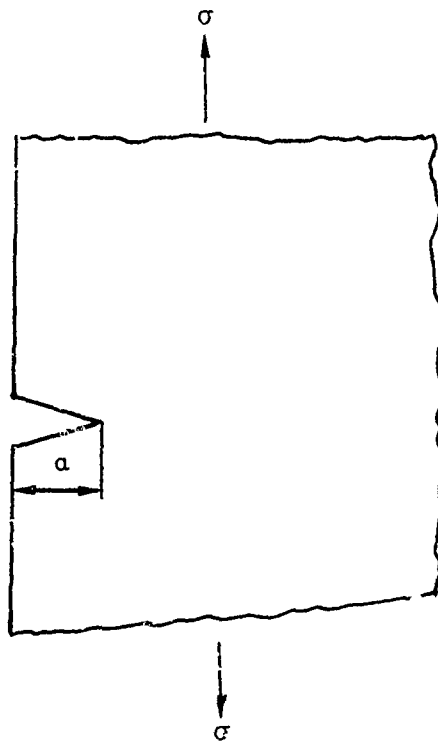
a. An Edge Crack in a Semi-Infinite
Sheet Subjected to Uniaxial Tension
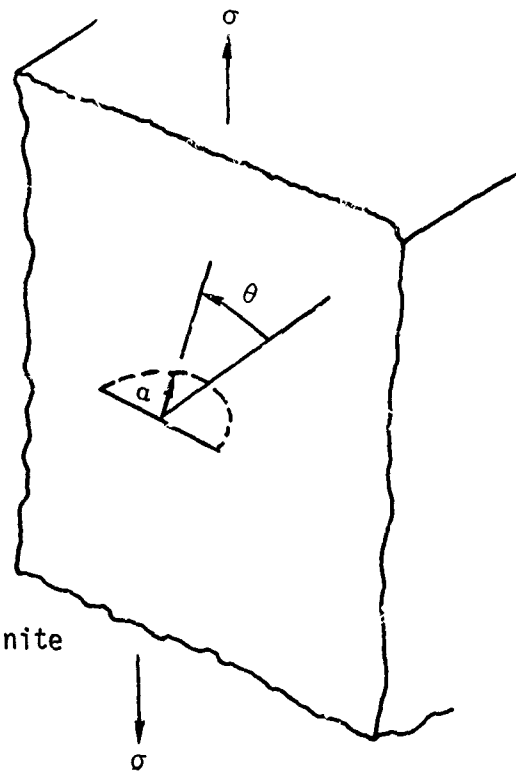
b. Semicircular Edge Crack in a Semi-Infinite
Solid Subjected to Uniaxial Tension

Figure 41.   Crack Geometries for Stress Intensity Evaluations.

Adler and Hooker (1976) showed that Blowers' model and analysis of a water drop impact could be used to estimate the stresses in an elastic half-space (Blowers, 1969). For brittle materials the critical stress conditions occur at and near the surface of the half-space outside of the expanding water drop contact zone. Hackworth and Kocher (1977) used the computer program for Blowers' analytical solution to evaluate many impact conditions including the spatial and temporal development of the radial stress component for low velocity water drop impacts on zinc sulfide. Hackworth and Kocher recorded the values of the peak radial tensile stresses, however they ignored any criterion for the onset of pressure release. Their subsequent work (Hackworth and Kocher, 1978) attempted to incorporate the pressure profile developed by Rosenblatt, et al. (1977) into Blowers' formulation of the water drop impact problem. The deficiencies in their modification of Blowers' original derivation are discussed in Section V.1. The radial stress levels they report are for relatively long times after the initial contact with the target. More representative conditions for the near-field stress levels were provided in Section III.3b.

Assuming as a first approximation that the radial tensile stress is responsible for crack propagation, the magnitude of this stress will be used in conjunction with Eq.(8.1) and (8.2) to estimate the potential for significant stress wave/surface flaw interactions. Representative stress levels will be considered in relation to the critical flaw size, a_c, which may be responsible for the observed cracks in water drop impacted zinc sulfide. Since the critical stress intensity factor is known and estimates of the applied tensile stress can be made, a_c can be evaluated using Eqs.(8.1) and (8.2). The parameters associated with the two-dimensional case, Eq.(8.1), will be denoted by primes and those associated with the semicircular flaw by double primes, Eq.(8.2). When $C = 1.03$ the fracture stress for the semicircular flaw is considerably larger than that required for an edge crack when $a_c' = a_c''$: the depth of the crack is the same for both cases.

$$\sigma_F' = 0.505 \frac{K_{IC}}{\sqrt{a_c'}} \tag{8.3}$$

$$\sigma_F'' = 0.856 \frac{K_{IC}}{\sqrt{a_c''}} \qquad (8.4)$$

According to Hackworth and Kocher (1977), the radial tensile stresses for a 2 mm drop impacting at 222 ms^{-1} acting long enough to propagate cracks reach a level of 170 MPa with a peak value of 196 MPa at a depth of 12.7 µm below the surface. Setting $a_c = 12.7$ µm in Eq.(8.3) and (8.4), we find $\sigma_F' = 95$ MPa and $\sigma_F'' = 162$ MPa. The fracture stresses when $a_c = 5$ µm are $\sigma_F' = 151$ MPa and $\sigma_F'' = 256$ MPa. The transient radial tensile stresses for this case attain an effective level of 255 MPa with a peak value of 285 MPa. The magnitude of the tensile stresses generated depends on the impact velocity and drop size, however these calculations indicate that the potential for crack growth does prevail for the applied stress conditions and flaw sizes which appear to be consistent with our experimental observations. The comparable test condition would be shot no. 815 which is a 1.60 mm water drop impact at 237 ms^{-1}. The observed maximum fracture depth is 40 µm and several cracks on the order of 5 µm were seen.

The plots of the radial stress component in Section III.3.b indicate that appreciably larger stresses are generated for higher impact velocities. At 700 ms^{-1} radial stresses on the order of 1 GPa occur in the target at a depth of 5 µm. These stress levels have the potential for propagating cracks from critical flaws on the order of 0.1 µm. The magnitude of the radial stress will also increase as the surface of the target is approached. Thus the surface finish has a strong influence on the propagation of cracks into the substrate. Concentrating on cracks which do not appear to originate from surface scratches, it would seem reasonable to speculate that a large proportion of the cracks originate from nucleating flaws less than the grain size. The correlation of the radial distance at which fractures are first observed and the development of significant radial tensile stresses as described in Section III.3.b appears to be consistent with the experimental data over the impact velocity range from 200 to 700 ms^{-1} as summarized in Table 8.

Rosenblatt and co-workers (1976, 1977) have also considered the problems outlined here for a zinc selenide target material with a mean grain size of 50 μm. The smallest grid sizes used in this work for the finite difference representation of the target material was 25 μm for a 1 mm water drop which would be equivalent to 50 μm for a 2 mm water drop. The typical grid used in this work for a 2 mm water drop was 100 μm. Subsequent calculations (Rosenblatt and Ito, 1978) use a 12.5 μm grid size for a 2 mm water drop. The peak radial tensile stresses were evaluated as a function of depth into the target. This computation would only supply the values of the stresses averaged over a distance of 12.5 μm from the surface and applied to the midpoint of this cell. The available analytic solution indicates there is a significant gradient in the radial stress with distance into the target over the 12.5 μm cell dimension, so a considerably finer grid would be required to provide comprehensive stress data for zinc sulfide. The analytic solution can compute the values of the stress components in increments of hundredths or thousandths of a micrometer if desired with computational times running on the order of seconds for each depth over the complete range of radial distances that these stresses are significant. The approach used by Rosenblatt and Ito for the surface crack interaction is different than that being pursued here.

One of the central issues pertaining to hydraulic penetration is to understand the mechanism by which hydraulic penetration of cracks leads to crack growth and erosion pit nucleation. Obviously, this problem is complicated in general because of the combined effects of the hydrodynamics of the water in the crack and the interaction with the locally induced stress waves generated during the penetration process. As a first step toward describing this process, a much simpler problem has been considered: namely, a two-dimensional pressurized surface crack inclined to the surface. The result of this calculation is the stress distribution surrounding the crack with particular emphasis on the effect produced by the proximity of the surface. From this stress distribution, the initial direction and possibly the velocity of crack propagation as a function of initial crack angle and depth will be determined using currently available fracture models.

It is our contention that the fracture problems identified and presently being analyzed in terms of a continuum mechanics approach are the critical problems which must be addressed in order to formulate a productive analytical framework for describing the particle impact response of CVD zinc sulfide. These analyses have been carried out in a balanced association with observations of the actual effects of the water drop collision process. Experimental procedures have been utilized to gain understanding of the relationships between the material's surface condition and microstructure and the nature and extent of the resulting crack patterns.

The experimental observations of the fractures produced by water drop impingement indicate a relative insensitivity to the grain size and general grain structure in CVD ZnS. On the other hand, Hackworth and Kocher (1978) report seeing a significant reduction in damage coincident with reduction of grain size in ZnSe. This result, seemingly in conflict with the present finding, is easily reconciled by the following observations. The grain size used in Hackworth and Kocher's (1978) work, although not reported numerically, appears in their micrograph to be a large grain size possibly on the order of 100 μm intercept distance in the plane shown and unresolvable at the stated magnification of 135 (presumably <10 μm) for the micrograph of the fine grained material. This grain size variation represents not only a much larger range than this study, but the larger grain size is on the order of the impact fracture pattern dimensions. Combining this observation with the observations made on ZnS would indicate that reductions in grain size beyond an order of magnitude below the fracture size will not yield a significant erosion resistance.

Examination of the micrographs of water drop impacts presented by Hackworth and Kocher (1978) to illustrate that the fine grain ZnSe has better erosion resistance than the large grain ZnSe reveals that although the fractures are smaller in the small grain material there are also many more of them. This indicates that most probably a similar amount of fracture surface area was created for each impact; i.e., a similar amount of energy dissipated in fracturing the specimen but the form of the fractures

changed. Hackworth and Kocher (1978) also report that although the resistance of ZnSe improved with reduced grain size it did not equal that of ZnS. This indicates that erosion resistance is governed by a more intrinsic material variable than grain size or hardness.

The effect of grain size and microhardness on the erosion resistance of zinc sulfide has been described by Adler and Hooker (1978). It is pointed out that substantial strengthening would be anticipated when the grain boundaries effectively resist fracture propagation, when fracture propagation is confined to crystallographic cleavage planes, and when the grain size is much smaller than the drop size. With the exception of confirmation of fracture propagation along crystallographic cleavage planes these conditions are satisfied by the CVD ZnS formulations which have been investigated. Furthermore Adler and Hooker indicated that the standard mechanical fracture tests evaluate the response to the largest flaw present, however the erosion process depends upon the concurrent propagation of a surface flaw population. The largest flaw may not be representative of the average behavior of the population. It is also shown here that the magnitude of the imposed radial stresses for 2 mm water drops impacting at velocities in excess of 300 ms^{-1} is many times the calculated fracture stress levels for reasonable flaw dimensions as identified from the CVD ZnS specimens evaluated. In view of the overwhelming amount of energy available and the imposed stress levels, it is unlikely that further modification of the bulk material will significantly improve the erosion resistance of CVD ZnS.

Considerably greater latitude for increased resistance to rain erosion can be gained from improved polishing procedures and subsequent maintenance of the initial surface finish. The specimens used in this program were polished to better than average FLIR window specifications, but the capability of the water drop to interact with the polishing defects remaining even for this level of surface preparation is clearly evident in the water drop experiments. Submicrometer flaw depths will have to be achieved and maintained. The application of the antireflectant coating over this surface quality will certainly have a positive influence on improving the erosion resistance.

SECTION IX

CONCLUSIONS

The general fracture behavior of CVD ZnS due to water drop impingement has been investigated. Three zinc sulfide formulations have been considered representing a range of grain sizes, grain shapes, and inclusion content. The microscopic observations of the damage produced by 2 mm diameter water drops impacting from 222 to 684 ms^{-1} indicate that there is no discernable difference in the fracture trajectories or penetration depths for the microstructural variations examined. It is found that no significant improvement in the erosion resistance will accrue from further modification of the bulk properties of the CVD processed ZnS. The dominant fracture mode is transgranular, and the grain size is small enough in relation to the loaded region of a 1 mm or larger water drop that no benefit will be gained from further grain refinement.

The most important factor in relation to the fracture response of the currently produced CVD ZnS was the quality of the surface finish. Calculations were provided which indicated the imposed tensile stress levels for 2 mm water drops impacting at 200 ms^{-1} were comparable to the fracture stress for reasonable surface scratch dimensions to several times the estimated fracture stress as the impact velocity approached 700 ms^{-1}. On the basis of these straightforward estimates of the critical stress levels, a significant increase in the erosion resistance appears to be possible if the surface polishing defects do not exceed a depth of 1 μm and preferably 0.1 μm.

The need for evaluating the transient stress states at and near the surface of the specimen was an outgrowth of the experimental program where it appears that the fracture nucleating surface flaws are on the order of 5 μm or less. The available analytical and numerical stress wave analyses were to be used for modeling the observed fracture response of CVD ZnS, however these analyses were found to be inadequate for various reasons which have been enumerated. This survey of available approaches motivated the

development of the mathematical analysis of the transient stresses due to a water drop collision presented in Section V. Further work is required to obtain numerical results, however a generalization of Blowers' analytical approach is now available which should be applicable to a spatially and temporally varying loading function applied to the surface of the target.

Two fracture conditions have been identified as being the most relevant to the general degradation of infrared transmitting windows. The first is the interaction of the transient stresses generated by the impact with surface flaws, and the second is hydraulic penetration of the water from an impacting water drop into a pre-existing surface crack. Stress analyses for both of these critical problems have been initiated as described in Section VI.

The transmission degradation which may arise due to cracks in the material once they are formed also has been treated analytically. The significance of the crack face separation distance and the crack orientation is estimated in the preliminary calculations presented in Section VII.

REFERENCES

W.F. Adler (1977). "Liquid Drop Collisions on Deformable Media," J. Materials Sci., 12, 1253-1271.

W.F. Adler (1979a). "The Mechanics of Liquid Impact," Treatise on Materials Science and Technology, Volume 16: Materials Erosion (C.M. Preece, ed.), New York: Academic Press, forthcoming.

W.F. Adler (1979b). "Single Water Drop Impacts on Polymethylmethacrylate," Proc. Fifth Int. Conference on Erosion by Liquid and Solid Impact, Cambridge, England.

W.F. Adler and S.V. Hooker (1976). Characterization of Transparent Materials for Erosion Resistance, Air Force Materials Laboratory Report AFML-TR-76-16.

W.F. Adler and S.V. Hooker (1978). "Water Drop Impact Damage in Zinc Sulfide," Wear, 48, 103-119.

W.F. Adler and T.W. James (1979). Particle Impact Damages in Ceramics, Technical Report for Office of Naval Research Contract N00014-76-C-0744 (March 1979).

W.N. Bailey (1936). "Some Infinite Integrals Involving Bessel Functions," Proc. London. Math. Soc., 40 (1936), 37-48.

R.M. Blowers (1969). "On the Response of an Elastic Solid to Droplet Impact," J. Inst. Maths. Applics., 5, 167-193.

F.P. Bowden and J.E. Field (1964). "The Brittle Fracture of Solids by Liquid Impact, by Solid Impact, and by Shock," Proc. R. Soc. Lond., A282, 331-352.

O.L. Bowie (1973). "Solution of Plane Crack Problems by Mapping Techniques," Mechanics of Fracture 1 (G.C. Sih, ed.), Leyden: Noordhoff International Publishing.

A.G. Evans (1979). Personal communication.

A.G. Evans and R.T. Wilshaw (1976). "Quasi-Static Solid Particle Damage in Brittle Solids--I. Observations, Analysis and Implications." Acta Met, 939-956.

G.A. Graves, D.E. McCullum and J.M. Wimmer (1977). Exploratory Development and Investigation of the Thermal, Electrical, Mechanical, and Physical Properties of Infrared Laser Window and I-R Transmitting Materials, Air Force Materials Laboratory AFML-TR-77-23.

163

J.V. Hackworth and L.H. Kocher (1977). Exploratory Development of Rain Erosion Resistant Infrared Window Materials, Air Force Materials Laboratory Report AFML-TR-77-84.

J.V. Hackworth and L.H. Kocher (1978). Behavior of Infrared Window Materials Exposed to Rain Drop Environments at Velocities to 2000 ft/sec (610 m/s), Air Force Materials Laboratory Report AFML-TR-78-184.

J.V. Hackworth, L.H. Kocher, and I.C. Snell (1979). "The Response of Infrared Transmitting Materials to High Velocity Impact by Water Drops," Erosion: Prevention and Useful Applications, ASTM STP 664 (W.F. Adler, ed.), Philadelphia: American Society for Testing and Materials, pp. 255-278.

F.J. Heymann (1968). "On the Shock Wave Velocity and Impact Pressure in High-Speed Liquid-Solid Impact," Trans. ASME, J. Basic Eng., 90, 400-402.

Y. Huang (1971). "Numerical Studies of Unsteady, Two-Dimensional Liquid Impact Phenomena," Ph.D. Thesis, Univ. of Michigan.

M.A. Hussain, S.L. Pu, and J. Underwood (1974). "Strain Energy Release Rate for a Crack Under Combined Mode I and II," Fracture Analysis ASTM STP 560, American Society for Testing and Materials, 1974, pp. 2-28.

J.-B.G. Hwang (1975). "The Impact Between a Liquid Drop and an Elastic Half-Space," Ph.D. Thesis, University of Michigan.

N.I. Muskhelishvili (1953). Some Basic Problems of the Mathematical Theory of Elasticity, Groningen, Holland: P. Noordhoff Ltd.

Paris and G.C. Sih (1965). "Stress Analysis of Cracks," Fracture Toughness Testing and Its Applications, ASTM STP 381, Philadelphia: American Society for Testing and Materials, pp. 30-83.

T.L. Peterson (1975). "Rain Erosion Effects in Infrared Window Materials," presented at a meeting of the American Ceramic Society, Washington, D.C.

T.L. Peterson (1979). "Multiple Water Drop Impact Damage in Layered Infrared Transparent Materials," Erosion: Prevention and Useful Applications, ASTM STP 664 (W.F. Adler, ed.), Philadelphia: American Society for Testing and Materials, pp. 279-297.

M. Rosenblatt, G.E. Eggum, L.A. DeAngelo, and K.N. Kreyenhagen (1976). Numerical Investigation of Water Drop Erosion Mechanisms in Infrared-Transparent Materials, Air Force Materials Laboratory Report AFML-TR-76-193.